UNIVERSITY OF CALGARY

Evaluating the Potential of Reflection-Based Waveform Inversion

by

Khalid A. Almuteri

A THESIS

SUBMITTED TO THE FACULTY OF GRADUATE STUDIES

IN PARTIAL FULFILLMENT OF THE REQUIREMENTS FOR THE

DEGREE OF MASTER OF SCIENCE

GRADUATE PROGRAM IN GEOLOGY AND GEOPHYSICS

CALGARY, ALBERTA

JUNE, 2017

Abstract

Full waveform inversion (FWI) is a powerful tool to build high-resolution velocity models, from recorded seismic data. However, a major issue with FWI is that it fails to reconstruct the low-wavenumber components of the velocity model in the absence of low-frequency information in the data. Generally, for a limited-offset acquisition geometry, deep targets are only sampled by reflected waves with narrow scattering angles, which makes such failure inevitable. In this thesis, I point out the limitation of conventional FWI when applied to reflection data and review, implement and analyze an alternative approach to overcome this limitation called reflection-based waveform inversion (RWI). The new waveform inversion formalism relies on decomposing the subsurface model into a background part that I seek to resolve, and a reflectivity part that is assumed to be known. Separating the decoupled velocity model into long- and short-wavelength components permits us to extract the contribution of the reflected data to the background part of the velocity model. In this thesis, I show that RWI retrieves the long-wavelength information from seismic reflections where FWI fails, and that it is the concept of modeling by seismic demigration that enables this retrieval. Also, I show that modeling by seismic demigration imposes limitations to RWI, as it removes any amplitude versus offset (AVO) information and mandates reflections-only recorded data, which prevents the usage of diving waves, refractions and direct arrivals. I show that applying source-receiver illumination compensation to the gradient enhances the contributions of deeper reflections and speeds up the convergence of the inversion. Also, I show that the choice of having the source function in the wave equation as a forcing term or as a boundary value problem (BVP) has a major impact on the inversion results and that the inversion is highly sensitive to the way the source function is treated in the wave equation. All the tools used in this thesis to generate synthetic data, wavefields, and to carry the waveform inversion were developed from scratch using Python. The finite-difference en-

gine was validated by analyzing the AVO response for simple models, by examining reverse time migration results, and by testing the codes on FWI. The RWI code was validated with previously established results.

Acknowledgements

I would like to thank my supervisor Dr. Kris Innanen for giving me the opportunity to work with him on this project, and for his great help. Without his continuous support, encouragement, and guidance this thesis would not have been possible.

Also, I would like to thank my committee members, Dr. Daniel Trad and Dr. Larry Lines for their time, their help and useful comments. I also would like to thank Dr. Daniel Trad and Dr. Sam Gray for many helpful discussions and suggestions. I also want to thank my instructors Dr. Kris Innanen, Dr. Edward Krebes, Dr. John Bancroft, and Wenyong Pan for their wonderful courses that helped me a lot in this project.

Also, I would like to thank Dr. Yu Geng, Scott Keating, Khaled Al Dulaijan, and Dr. Faranak Mahmoudian for many useful discussions and suggestions. Also, I would like to extend my appreciation and thanks to Laura Baird and Kevin Hall for their help to make things easier for me and made my journey enjoyable. Also, I would like to thank all of CREWES staff, students, and sponsors. Also, I would like to thank Saudi Aramco for giving me the opportunity to pursue a graduate degree.

Finally, I would like to thank Khaled Al Dulaijan, Mohammed Kanfar, Scott Keating, Adriana Gordon, Bobby Gunning, Andrew Mills, Eric Rops, and all others for making my time here an enjoyable experience.

Dedication

I would like to dedicate this work to my parents and siblings. Without their continuous help and support, I wouldn't be here.

Table of Contents

List of Tables

List of Figures and Illustrations

Chapter 1

Introduction

1.1 Seismic migration

In exploration seismology, raw seismic data is processed to produce an interpretable structural image of the subsurface. In seismic processing, common-midpoint (CMP) gathers are created by grouping traces with the same source-receiver midpoint coordinate, and traces are sorted by source-receiver separation distance. Reflection traveltimes in CMP gathers are a function of offset. A correction, called normal moveout (NMO), is applied to CMP gathers to remove the traveltime moveout effect. For further details about seismic data processing, the reader is referred to Yilmaz (2001). Applying NMO to CMP gathers converts recorded seismic data into a zero-offset profile, a stacked section. The zero-offset profile is equivalent to having a seismic survey where each trace is created from a source and receiver placed at the same position in space. This creates a seismic image, but interpreting it requires an assumption to be made that recorded events are coming from reflectors directly beneath the source-receiver position. In reality, this assumption is not correct; however, not knowing the exact position in the subsurface of seismic events does not provide any other choice. As a consequence, seismic migration is needed to place recorded events at their correct subsurface positions, creating an accurate geometrical image of the subsurface. Seismic migration plays a crucial part in waveform inversion (Margrave et al., 2010). Stolt and Weglein (1985) provides an introduction to and resources that cover the relationship between seismic migration and inversion.

Seismic migration can be classified into ray based migration, such as Kirchhoff migration, and wave-equation or wavefield extrapolation migration (WEM). The WEM methods can be categorized into two classes: one-way wave-equation migration, and two-way wave-equation migration (Hemon, 1978; McMechan, 1983; Whitmore, 1983; Baysal et al., 1983), commonly known as reverse-time migration (RTM). The WEM abbreviation usually refers to the one-way wave-equation migration.

The concept of Kirchhoff migration is to broadcast seismic data over semi-circles or to sum seismic data along diffraction curves (Hagedoorn, 1954; Schneider, 1978). In pre-stack Kirchhoff migration, the broadcast is along semi-ellipses (Yilmaz, 2001). The theoretical basis of Kirchhoff migration was presented by Hagedoorn (1954). This method has been the favorable migration method in the industry for its efficiency, and for its capability to perform a target-oriented migration, and this is especially attractive for large 3-D data (Gray and May, 1994).

The early work by Claerbout (1970) led to the wave-equation based migration methods, as he formulated a finite-difference migration algorithm (Schneider, 1978). The advantage of wave-equation methods, over Kirchhoff, is their robustness, as they can cope with complex geological models. In WEM, wavefield extrapolation is carried out in depth (Berkhout, 1981). The concept of this method is to obtain a new instance of the recorded data, at which the recording plane is shifted downward in depth (Berkhout, 1981). Then, to form an image of the subsurface, the newly recorded data at time $t = 0$, at the level of the shifted recording plane, is projected to its corresponding depth plane in the image domain (Berkhout, 1981). In RTM, the process of migrating data is as follows:

1. A source wavefield, which is assumed to match the wavefield producing the observed data, is generated. It is computed by injecting a source function into a velocity model and forward propagating in time.

2. Back-propagating observed data to create a receiver wavefield.

3. An imaging condition, according to Claerbout's imaging principle (Claerbout, 1971), is applied on the modeled wavefields to obtain an image of the subsurface (Hemon, 1978; McMechan, 1983; Whitmore, 1983; Baysal et al., 1983).

1.2 Seismic inversion

Seismic migration aims at creating structural images, placing reflectors at their correct positions in the subsurface; however, there is no attempt to extract physical properties about the subsurface from the recorded data (Bleistein et al., 2001). Seismic inversion, on the other hand, is attempting to predict the physical parameters of the subsurface from seismic data (Mora, 1987). Inversion is a nonlinear problem, whose solution is attained through solving a linearized version iteratively (Wang, 2016). Inversion problems tend to be ill-posed, as in many cases a solution might not exist or might not be unique. Moreover, the inversion process can be very sensitive to small changes in the input data. Seismic inversion comprises an estimation problem, in which measured data is used to estimate model parameters, and an appraisal problem, to evaluate the inversion results' accuracy (Snieder, 1998). One of the most widely used and most rapidly developing inversion techniques is full waveform inversion (FWI).

FWI is an optimization problem that aims at extracting the Earth's physical parameters, from recorded seismic data, through an iterative inversion process (Lailly, 1983; Tarantola, 1984; Virieux and Operto, 2009). The rise of FWI as a velocity model building tool is due to the high-resolution models that it provides (Pan and Innanen, 2015a). The means by which FWI builds material properties is by iteratively minimizing the difference between predicted data and observed data through an objective function, usually a least-squares function. FWI in principle utilizes the full recorded data (e.g., direct waves, pre-critical reflections, post-critical reflections, multiples) in the inversion process (Virieux and Operto, 2009). The inversion can be carried out in the time domain (Tarantola, 1984; Mora, 1987; Crase et al., 1990) or in the frequency domain (Pratt and Worthington, 1990; Pratt, 1999; Pratt and Shipp, 1999).

FWI, although an attractive inversion tool, suffers from some limitations that need to be resolved. These issues can be divided into four main categories; nonlinearity limitation, data acquisition limitation, wave physics assumptions, and noise in recorded data. First, the nonlinearity of the seismic inverse problem produces an objective function with many local minima (Bunks et al., 1995). The local minima prevents the iterative inversion method from converging to the global minimum unless the starting model produces data within half a cycle from the observed data (Figure 1.4). Becoming trapped in such a local minimum is for this reason called ”cycle-skipping”. Second, low-frequency and long-offset data, necessary to avoid cycle-skipping and to reconstruct large-scale Earth model features, are usually unavailable in acquired data. According to Claerbout (1985), velocity is the low spatial-frequency part (Figure 1.2) of what is regarded as the ”real velocity” (Figure 1.1) and the high-frequency component (Figure 1.3) of the ”real velocity” is reflectivity and not velocity. The reflectivity part of the velocity model is linearly dependent on the data (Jannane et al., 1989). The low spatial-frequency part of the velocity, the smoothly varying background velocity, controls the arrival times of seismic events (Jannane et al., 1989; Zhou et al., 2012). As a consequence, to obtain an accurate velocity model, low-frequency information is vital (Figure 1.5). To mitigate the nonlinearity of the problem, a multiscale FWI approach is often taken (Bunks et al., 1995; Sirgue and Pratt, 2004; Virieux and Operto, 2009). Multiscale FWI is proposed in the time domain (Bunks et al., 1995) and in the frequency domain (Sirgue and Pratt, 2004). This approach improves the inversion results by decomposing the velocity model by scale (Bunks et al., 1995). Solving the problem iteratively at long scales get the solution closer to the neighborhood of the global minimum, as at low frequencies there are fewer local minima (Bunks et al., 1995). Higher frequencies are inverted at higher iterations to find the global minimum (Bunks et al., 1995).

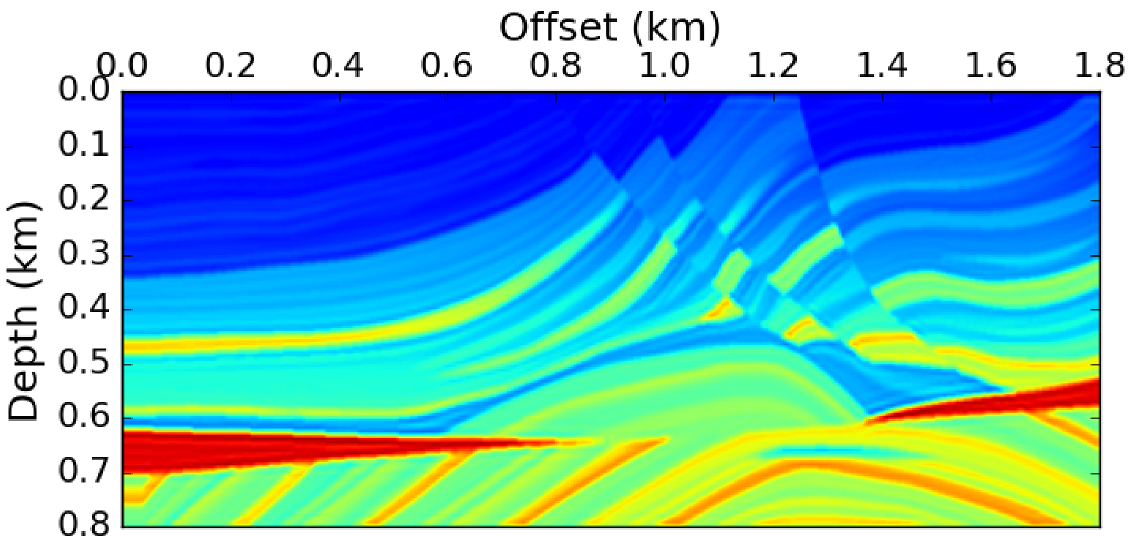

Figure 1.1: "Real velocity".

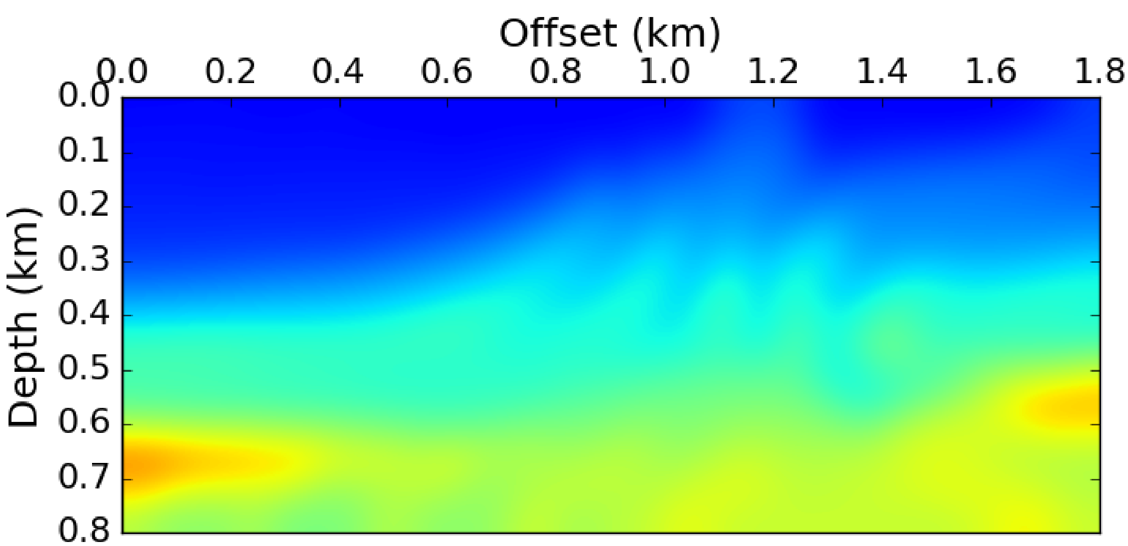

Figure 1.2: Low spatial-frequency component of the "real velocity". According to Claerbout (1985), this component of the subsurface is the velocity.

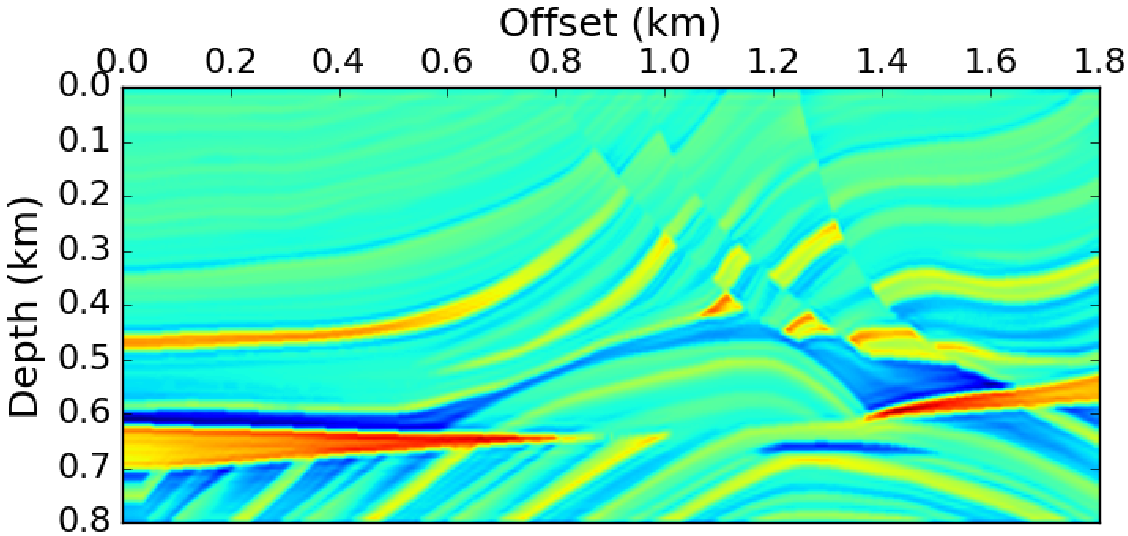

Figure 1.3: High spatial-frequency component of the "real velocity". According to Claerbout (1985), this component of the subsurface is the reflectivity.

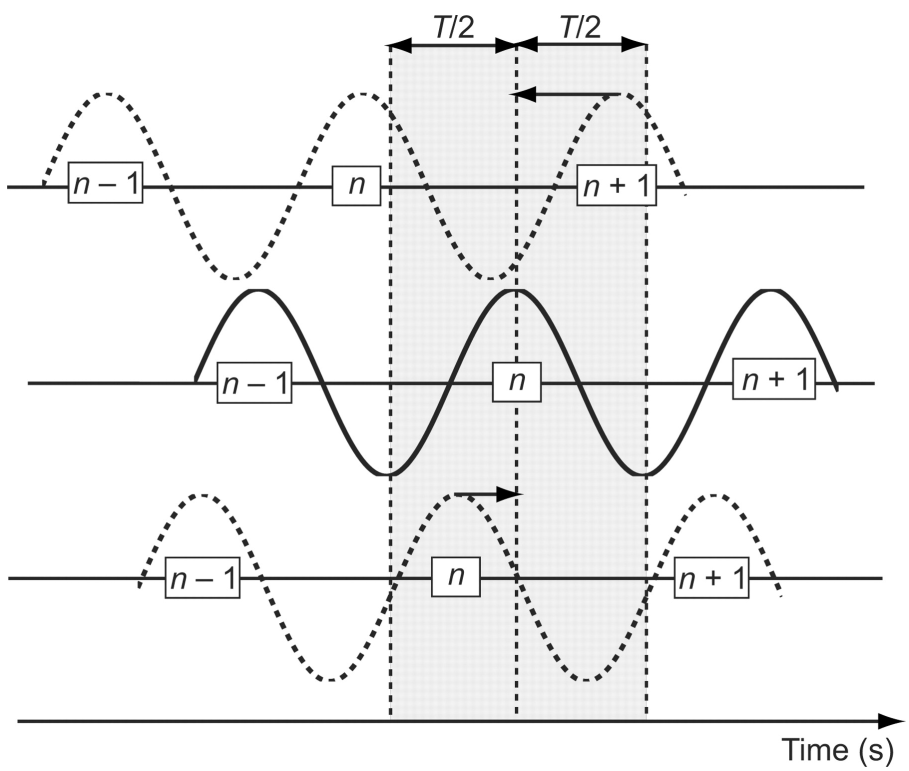

Figure 1.4: Cycle-skipping problem in FWI. [Figure 7 of (Virieux and Operto, 2009)].

Third, the wave physics accounted for in the inversion process might not necessarily be representative of the actual wave propagation behavior. For instance, inverting seismic data, which is best described with the elastic wave equation, with an acoustic wave equation (Mora, 1987; Mulder and Plessix, 2008). A multiparameter elastic inversion, in an elastic world, is necessary to avoid local minima (Mulder and Plessix, 2008). However, multiparameter inversion has its challenges, as it suffers from cross-talk effects and it is computationally expensive (Prieux et al., 2013; Operto et al., 2013; Pan et al., 2016; Pan and Innanen, 2015b). For this reason, in this thesis I consider an acoustic, single-parameter inverse problem, recognizing that doing so will introduce limits on the accuracy of any results. Finally, FWI treats all recorded data as a signal, including noise unrelated to earth properties and wave propagation through the earth. Such noise will contaminate the inversion results, as FWI will attempt to match this noise.

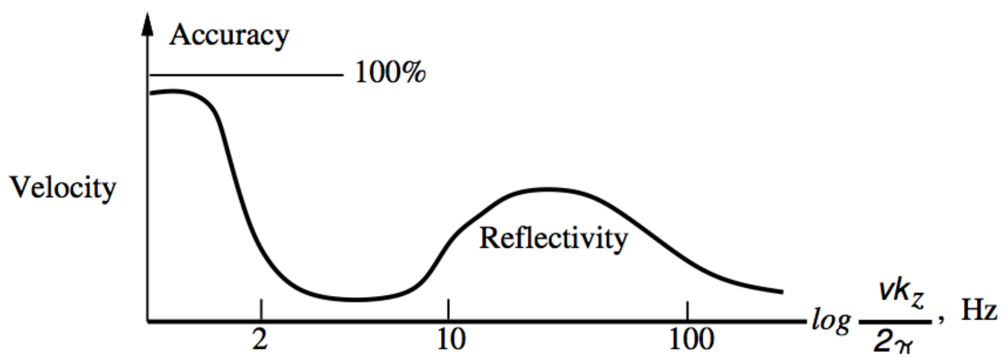

Figure 1.5: The relationship between seismic data and velocity information. [Figure 1.4-3 of (Claerbout, 1985)].

1.3 Thesis objectives and overview

The objective of this thesis is to examine the integrity of reflection-based waveform inversion (RWI) in recovering the background part of the velocity model and to validate the method by comparing the results to that of FWI. Also, I provide an explanation of how RWI differs from FWI in constructing the gradient. Some of the limitations of RWI are illustrated, and in some cases addressed with algorithm change.

In Chapter 2, I review the wave equation, the absorbing boundary conditions, the finite-difference scheme, the stability and accuracy of the numerical modeling, the concept of reverse-time migration, and the concept of modeling by seismic demigration.

In Chapter 3, I explain the theory behind RWI and provide the necessary derivations to the gradient. I also explain the motivation behind using RWI over FWI. Afterwards, I explain how the gradient construction in RWI is different from FWI.

In Chapter 4, I apply RWI to a simple model, using a scaled and non-scaled gradient, and compare the results with that of FWI. Also, I examine the influence of scaling the gradient on the inversion results.

In Chapter 5, I apply RWI to a small section of the Marmousi model, using a scaled gradient, and compare the results with that of FWI.

In Chapter 6, I discuss some of the practical issues in RWI and its relationship to modeling by seismic demigration. Also, I examine one possible solution to overcome one of the limitations.

Chapter 2

Wave equation and implementation of finite-difference solutions in Python

2.1 Introduction

Codes for numerical solution of the wave equation provide an environment where physical phenomena, associated with wave propagation, can be analyzed and studied; as exact analytical solutions are usually unavailable. In geophysics, wave equation modeling is the fundamental element of processes such as reverse-time migration, and seismic modeling and inversion. The finite-difference approximation is the simplest and most widely used method to solve the wave equation numerically. In this chapter, I review the wave equation and the tools needed for numerical implementation, reverse-time migration, and modeling by seismic demigration. A Python code for simulation was developed to illustrate this process. All examples in this chapter and all simulations in later chapters are carried out using this code package.

2.2 Wave equation

Forward modeling is an essential part of seismic waveform inversion. It enables us to generate modeled data and wavefields needed for this inversion process. The modeling process is governed by the wave equation, which provides the physics that ties the physical parameters of a model (e.g., velocity and density) to the simulated data. In other words, the wave equation transforms our information of the subsurface from the model domain to information about the subsurface in the data domain. In waveform inversion, this relationship is utilized to invert for the model domain information from the data domain information.

The 2-D multiparameter acoustic wave equation is given by

$$\frac{\partial^2 u}{\partial t^2} = \frac{\kappa^2}{\rho^2}\left[\rho \bigtriangledown \cdot \left(\frac{1}{\rho} \bigtriangledown u\right)\right] + f(t), \tag{2.1}$$

where $\rho = \rho(x,z)$ is the density, $\kappa = \kappa(x,z)$ is the bulk modulus, $u = u(x,z,t)$ is the pressure field, and $f(t)$ is the source function; it expands to

$$\frac{\partial^2 u}{\partial t^2} = v^2\left[\frac{-1}{\rho}\left(\frac{\partial \rho}{\partial x}\frac{\partial u}{\partial x} + \frac{\partial \rho}{\partial z}\frac{\partial u}{\partial z}\right) + \left(\frac{\partial^2 u}{\partial x^2} + \frac{\partial^2 u}{\partial z^2}\right)\right] + f(t), \tag{2.2}$$

where $v = v(x,z) = \sqrt{\frac{\kappa(x,z)}{\rho(x,z)}}$ is the compressional wave velocity. Hereafter, I assume a constant density model; hence, equation (2.2) reduces to

$$\frac{\partial^2 u}{\partial t^2} = v^2\left(\frac{\partial^2 u}{\partial x^2} + \frac{\partial^2 u}{\partial z^2}\right) + f(t). \tag{2.3}$$

2.3 Absorbing boundary conditions

Equation (2.3) defines the wave propagation in an unbounded domain. However, in numerical modeling we are limited to a finite domain; if no boundary conditions were applied, the model limits will act as an artificial boundary and will generate artificially reflected waves.

The absorbing boundary conditions (ABC) that I implemented in this project are the Clayton-Engquist boundary conditions (Clayton and Engquist, 1977). They are based on the paraxial approximation of the scalar wave equation that separates the wavefield into up-, down-, right-, and left-going waves (Claerbout, 1985).

To obtain the paraxial approximation, the first step is to Fourier transform the homogeneous wave equation

$$\frac{1}{v^2}\frac{\partial^2 u}{\partial t^2} = \bigtriangledown^2 u, \tag{2.4}$$

which yields the dispersion relation

$$k_x^2 + k_z^2 = \frac{\omega^2}{v^2}. \tag{2.5}$$

The dispersion relation enables us to separate the wavefield by solving for the appropriate wavenumber. For instance, the down-going wavefield is obtained by solving for the positive values of the wavenumber k_z

$$k_z = \sqrt{\frac{\omega^2}{v^2} - k_x^2} = \frac{\omega}{v}\sqrt{1 - \frac{v^2}{\omega^2}k_x^2} \tag{2.6}$$

$$\Rightarrow \frac{v}{\omega}k_z = \sqrt{1 - \frac{v^2}{\omega^2}k_x^2}. \tag{2.7}$$

The paraxial approximation is achieved by expanding the square root $\sqrt{1 - \frac{v^2}{\omega^2}k_x^2}$ and transforming the expansion to the space-time domain. Higher order approximations using the Taylor expansion gives an unstable paraxial approximation (Engquist and Majda, 1977), so the Padé expansion is more stable and used instead:

$$a_j = 1 - \frac{(vk_x/\omega)^2}{1 + a_{j-1}}, \tag{2.8}$$

where the jth approximation is given by $k_z = \frac{\omega}{v}\sqrt{1 - \left(\frac{v}{\omega}k_x\right)^2} \approx \frac{\omega}{v}a_j$, and $a_1 = 1$.

As a result, the first two orders of the paraxial approximation in Fourier domain are

$$First - order : k_z = \frac{\omega}{v} \tag{2.9a}$$

$$Second - order : k_z = \frac{\omega}{v}\left(1 - \frac{1}{2}\left(\frac{vk_x}{\omega}\right)^2\right), \tag{2.9b}$$

and the corresponding paraxial approximations in time-space domain are

$$First - order : \frac{\partial u}{\partial z} + \frac{1}{v}\frac{\partial u}{\partial t} = 0 \tag{2.10a}$$

$$Second - order : \frac{\partial^2 u}{\partial z \partial t} + \frac{1}{v}\frac{\partial^2 u}{\partial t^2} - \frac{v}{2}\frac{\partial^2 u}{\partial x^2} = 0. \tag{2.10b}$$

The first-order approximation, equation (2.10a), is known as the 5° wave equation, and the second-order approximation, equation (2.10b), is known as the 15° wave equation (Claerbout, 1985).

The 15° wave equation is discretized and solved to apply the ABC for the sides of the model. In this case, equation (2.10b) is used to create an absorbing boundary along the bottom side of the model. For the corners, the ABC is implemented by rotating the first-order approximations by 45° (Clayton and Engquist, 1977).

2.4 Differential operators

The wave equation can be solved numerically in the time domain or the frequency domain (Marfurt, 1984; Virieux and Operto, 2009). Finite-difference is the most widely used method to discretize and solve the wave equation (Virieux, 1986; Virieux and Operto, 2009). A second-order central finite difference approximation scheme is commonly used in the modeling. The second-order approximation of the first partial derivative is

$$\frac{\partial u}{\partial x} \approx \frac{u(x+h,z,t) - u(x-h,z,t)}{2h}, \tag{2.11}$$

where h is the grid points spacing (dt is used for the time step). Equation (2.11) in the indices notation is

$$\frac{\partial u}{\partial x} = u_x|_{x=i} \approx \frac{u^n_{i+1,j} - u^n_{i-1,j}}{2h}, \tag{2.12}$$

where the subscript i is for offset (x), the subscript j is for depth (z), and the superscript n is for time (t). The second-order approximation of the second partial derivative is

$$\frac{\partial^2 u}{\partial x^2} \approx \frac{u(x+h,z,t) - 2u(x,z,t) + u(x-h,z,t)}{h^2}. \tag{2.13}$$

Equation (2.13) in the indices notation is

$$\frac{\partial^2 u}{\partial x^2} = u_{xx}|_{x=i} \approx \frac{u^n_{i+1,j} - 2u^n_{i,j} + u^n_{i-1,j}}{h^2}. \tag{2.14}$$

The discretized form of equation (2.4), with the source term, is given by

$$\frac{u^{n+1}_{i,j} - 2u^n_{i,j} + u^{n-1}_{i,j}}{dt^2} \approx v^2_{i,j}\frac{u^n_{i+1,j} + u^n_{i,j+1} - 4u^n_{i,j} + u^n_{i-1,j} + u^n_{i,j-1}}{h^2} + f_{n+1}, \tag{2.15}$$

where we solve for $u^{n+1}_{i,j}$.

2.5 Stability and grid dispersion

Wave equation discretization causes two issues to the numerical solution; grid dispersion, and instability in the forward modeling. Grid dispersion causes different frequencies to travel at different velocities, whereas instability of the finite-difference process results in accumulation of errors and failure of the numerical solution. As a result, two necessary criteria need to be met to limit the consequences of the discretization.

The first criterion relates the grid dispersion to the spatial sampling h. If h is not small enough, a dispersion will occur. For a second-order finite difference, at least, ten grid points are required for the upper half-power wavelength of the source (Alford et al., 1974). The equation that governs the relationship is

$$h \leq \frac{v_{min}(x,z)}{10 f_\circ}, \tag{2.16}$$

where $f_\circ$ is the upper half-power frequency (Figure 2.1). The second criterion relates the stability to the temporal sampling dt (Lines et al., 1999). The criterion for a second-order scheme is

$$\frac{v_{max}(x,z)dt}{h} \leq \frac{1}{\sqrt{2}}. \tag{2.17}$$

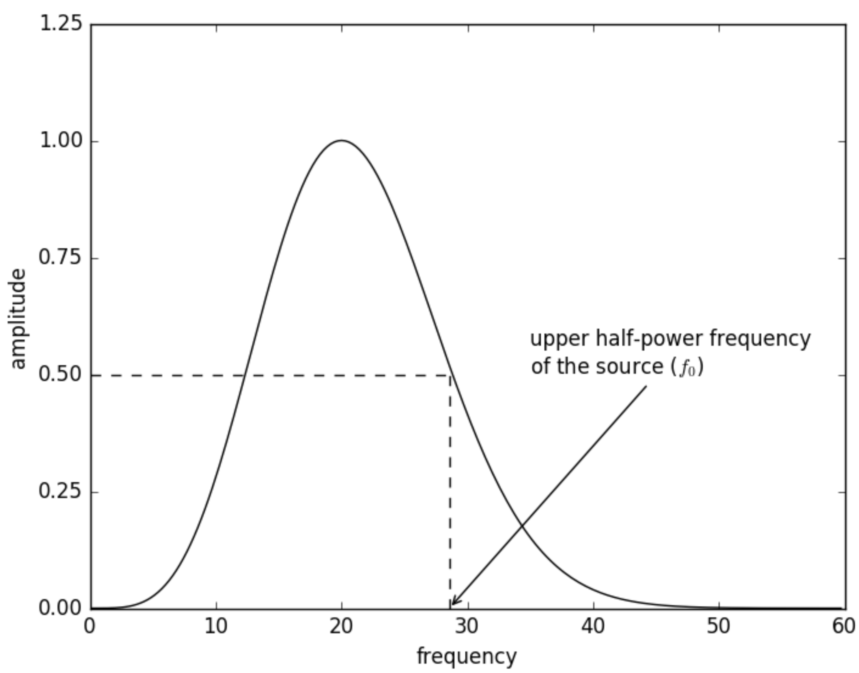

Figure 2.1: Power spectrum of source wavelet [Figure 3a of (Alford et al., 1974)].

2.6 Wave propagation examples

In this section, I show samples of shot gathers and wavefield propagation snapshots created using the implemented Python code. For this, I use Marmousi model (Figure 2.2). Wavefield propagation snapshots, for a source at $x = 2.35$ km, at $t = 0.26$ s, 0.52 s, and 0.78 s are shown in Figures (2.3), (2.4) and (2.5), respectively. In Figures (2.6) and (2.7) shot gathers for sources at $x = 2.35$ km and at $x = 3.85$ km are plotted, respectively.

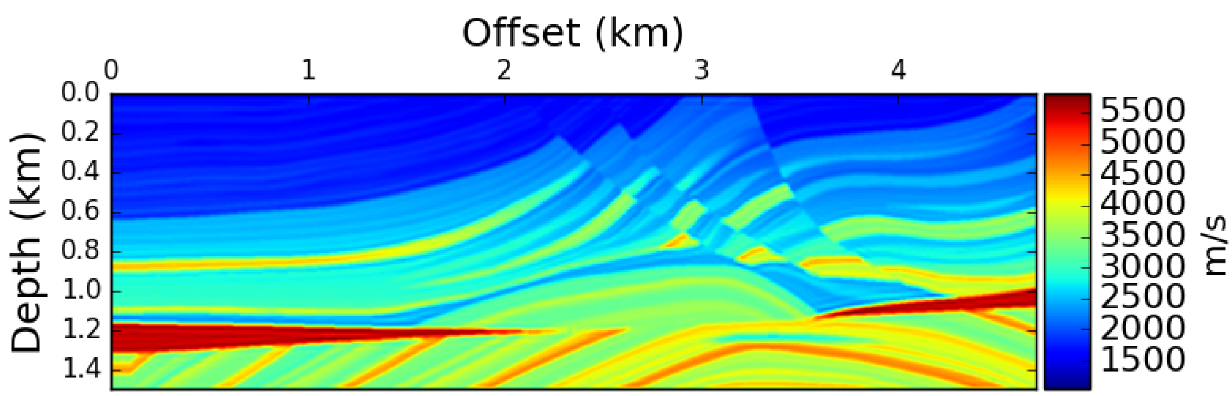

Figure 2.2: Marmousi model.

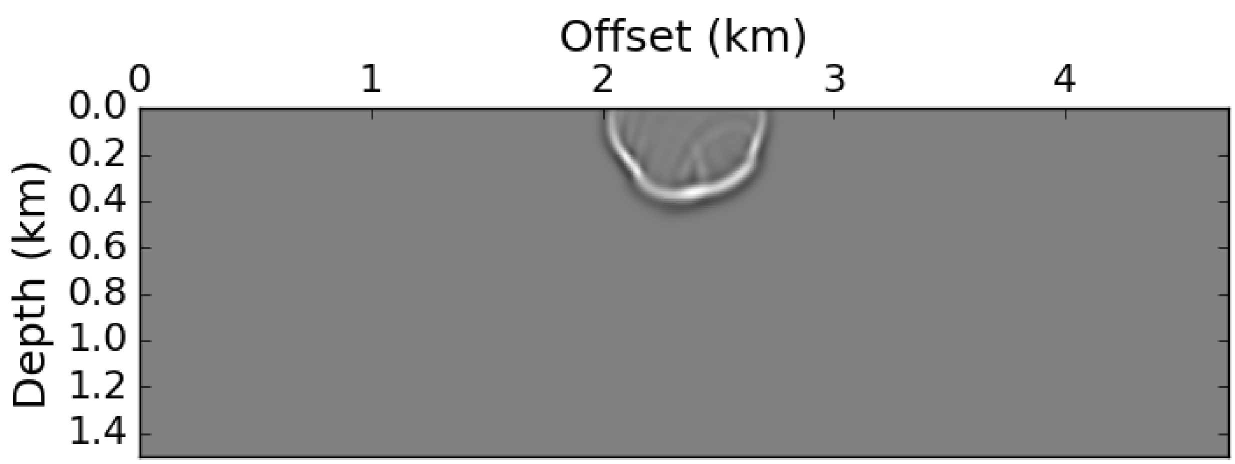

Figure 2.3: Wavefield snapshot for a source at $x = 2.35$ km at $t = 0.26$ s.

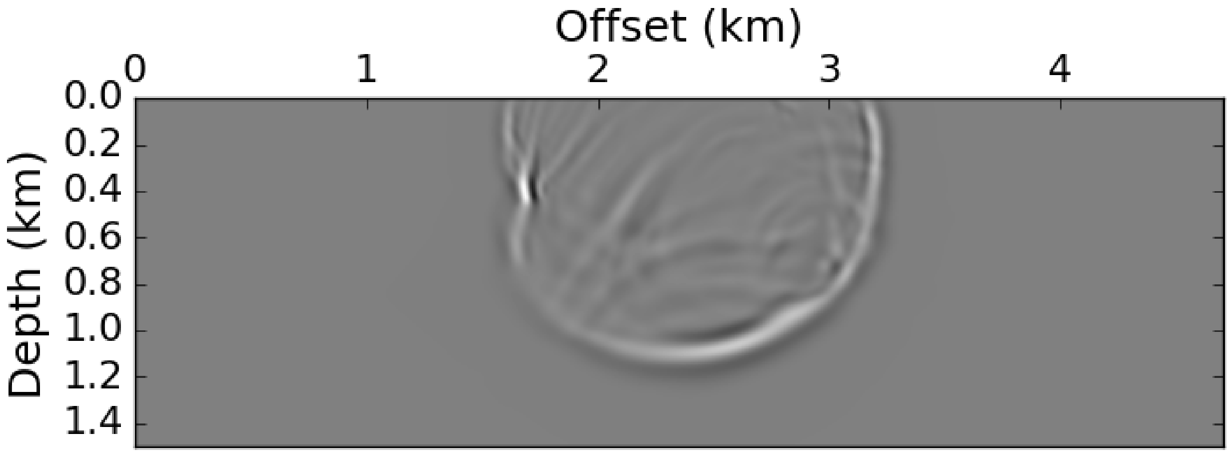

Figure 2.4: Wavefield snapshot for a source at $x = 2.35$ km at $t = 0.52$ s.

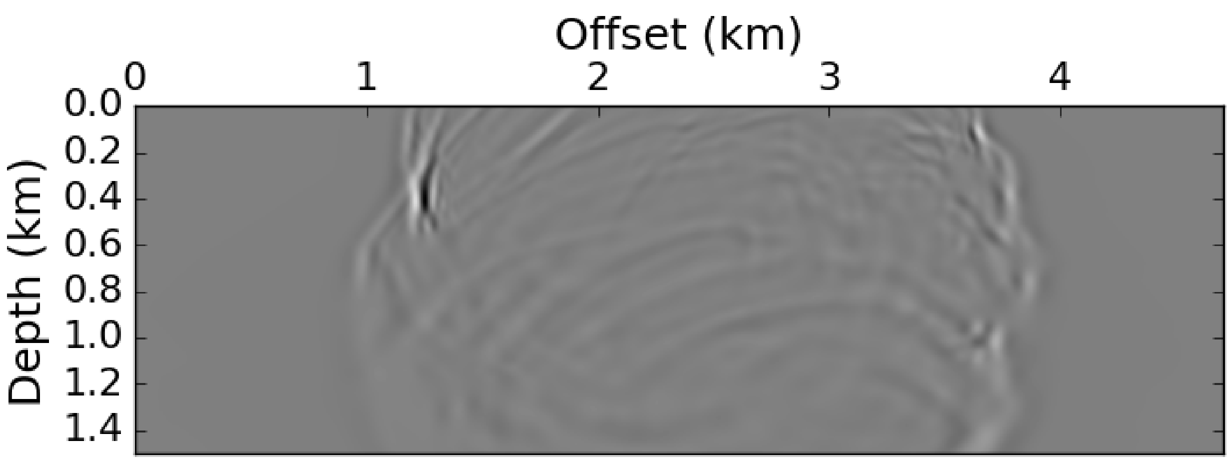

Figure 2.5: Wavefield snapshot for a source at $x = 2.35$ km at $t = 0.78$ s.

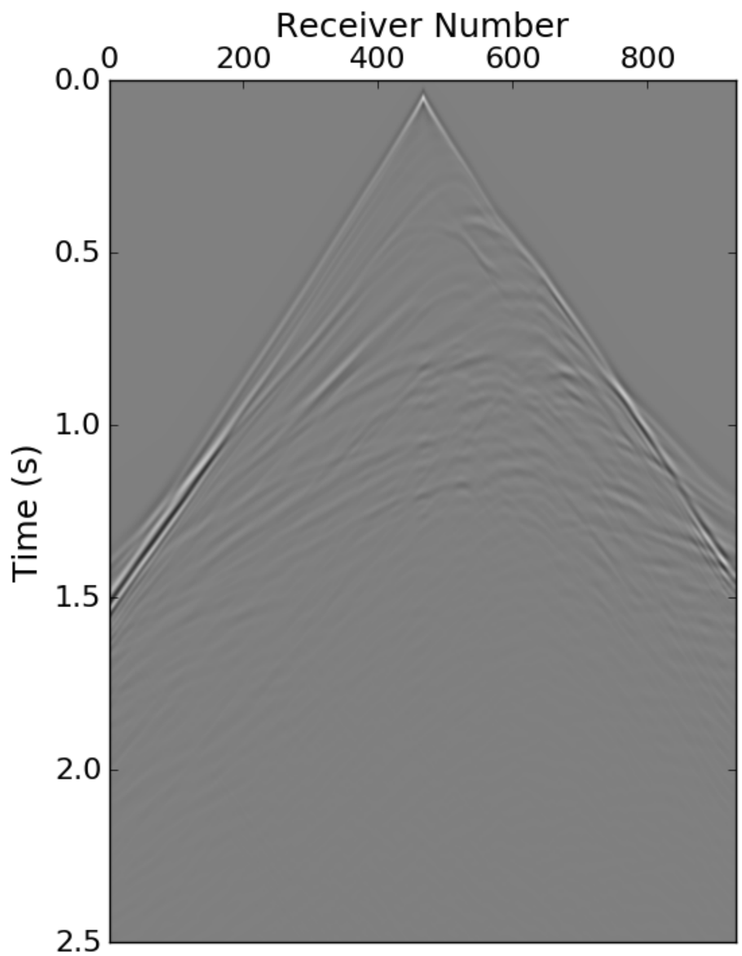

Figure 2.6: Shot gather for a source at $x = 2.35$ km.

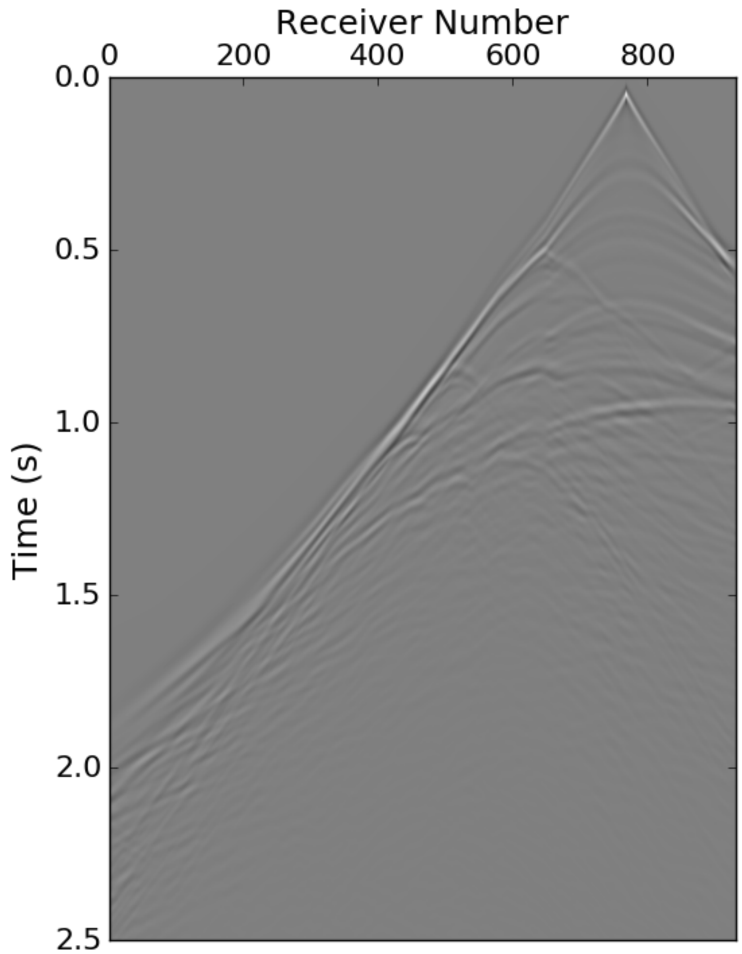

Figure 2.7: Shot gather for a source at $x = 3.85$ km.

2.7 Reverse time migration

Reverse time migration (RTM) (Hemon, 1978; McMechan, 1983; Whitmore, 1983; Baysal et al., 1983) is a two-way wave equation migration scheme that is becoming the favored imaging method in the industry in areas with complex geology. As a consequence of using the complete wave equation, it can handle different types of waves (reflections, refractions, multiples, etc.), (Zhang and Sun, 2009). The concept of RTM follows Claerbout's (1971) imaging principle: a reflector exists at a point (x, z) when a downgoing (source) wavefield, $G(\mathbf{r}, t; \mathbf{r}_s)$, and an upgoing (receiver) wavefield, $G(\mathbf{r}, t; \mathbf{r}_g)$, coincide in time at (x, z), where

$G(\mathbf{r}, t; \mathbf{r}_s)$ and $G(\mathbf{r}, t; \mathbf{r}_g)$ are defined as

$$\left[\bigtriangledown^2 - \mathbf{m}\frac{\partial^2}{\partial t^2}\right] G(\mathbf{r}, t; \mathbf{r}_s) = f(t), \tag{2.18}$$

where $f(t)$ is the source function, and

$$\begin{cases} \left[\bigtriangledown^2 - \mathbf{m}\frac{\partial^2}{\partial t^2}\right] G(\mathbf{r}, t; \mathbf{r}_g) = 0 \\ G(\mathbf{r}_g, t; \mathbf{r}_g) = G(\mathbf{r}_g, t; \mathbf{r}_s), \end{cases} \tag{2.19}$$

respectively. As a result, one can obtain the reflectivity model by deconvolving the receiver and source wavefields, equation (2.20).

$$R(\mathbf{r}) = \int d\omega \frac{G(\mathbf{r}, \omega; \mathbf{r}_g)}{G(\mathbf{r}, \omega; \mathbf{r}_s)} \tag{2.20}$$

This is easily done for the one-way wave equation migration in the frequency domain, as the deconvolution process in time domain is simply a division in frequency domain (Zhang and Sun, 2009). Another approach is to apply a cross-correlation imaging condition (Claerbout, 1971)

$$I(\mathbf{r}) = G(\mathbf{r}, t; \mathbf{r}_s) \otimes G(\mathbf{r}, -t; \mathbf{r}_g), \tag{2.21}$$

where $\otimes$ denotes cross-correlation and $I(\mathbf{r})$ is assumed to be a good representation of the subsurface.

2.7.1 Laplacian filter

Reverse time migration tends to produce low-frequency artifacts as a consequence of the conventional cross-correlation imaging condition, equation (2.21). Commonly, migration artifacts occur at shallow depths and above strong reflectors (Zhang and Sun, 2009), and they can mask deeper events.

In RTM, cross-correlating a source wavefield with a reversed receiver wavefield results in energy focusing, or maximum cross-correlation occurring, at reflectors locations. The travel time of seismic energy from a source to a subsurface location, t_s, and the travel time from the same subsurface location to a receiver, t_r, is the recorded two-way travel time, t.

$$t_s + t_r = t \tag{2.22}$$

The sum of any two segments along the ray path, taken by the seismic energy, will add up to the recorded two-way travel time; creating a potential location for the subsurface reflector. As a result, the cross-correlation will create an unrealistic, low-frequency contaminated, image of the subsurface (Figure 2.8).

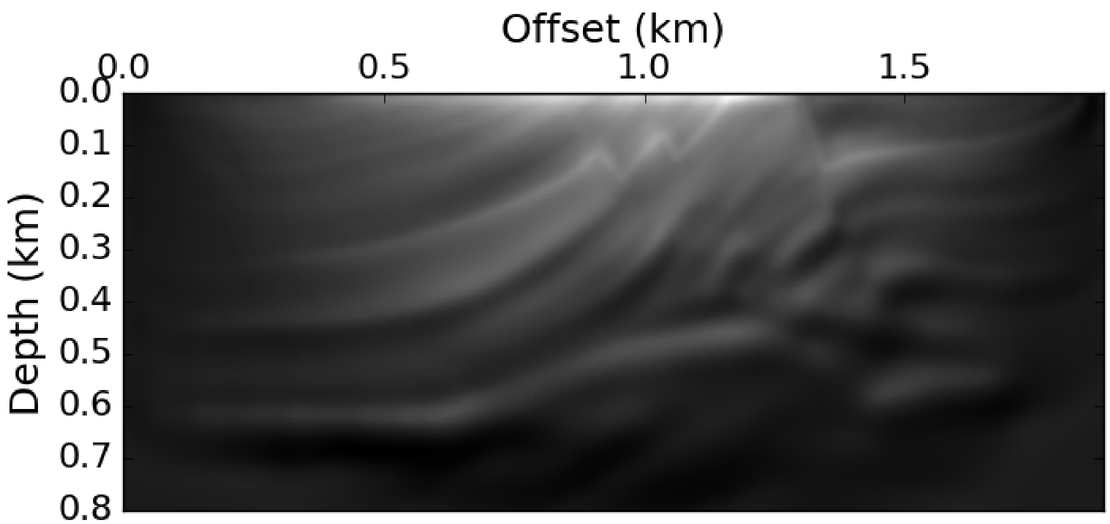

Figure 2.8: RTM of Marmousi model contaminated with low-frequency artifacts.

One way to eliminate such artifacts is by applying a Laplacian filter,

$$\nabla^2 I = \left(\frac{\partial^2 I}{\partial x^2} + \frac{\partial^2 I}{\partial z^2} \right), \tag{2.23}$$

to the RTM migrated image, $I(x, z)$. The Laplacian filter will suppress the low-frequency artifacts and create an interpretable image (Figure 2.9). However, it will remove low-frequency signal, and will increase the high-frequency noise (Guitton et al., 2006). Also, it introduces a 180° phase-shift to the signal and changes its amplitude.

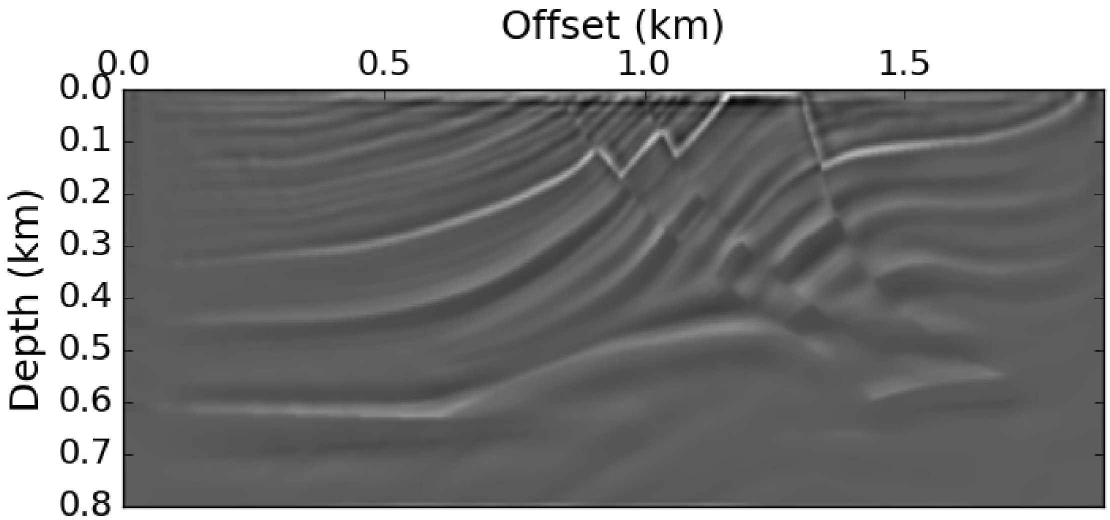

Figure 2.9: RTM of Marmousi model after applying Laplacian filter.

To understand the Laplacian filter, I investigate its behavior in the Fourier domain, where the Laplacian operator, equation (2.23), becomes

$$\mathcal{F}\left\{\nabla^2 I\right\} = \mathcal{F}\left\{\frac{\partial^2 I}{\partial x^2} + \frac{\partial^2 I}{\partial z^2}\right\} = -(k_x^2 + k_z^2)\mathcal{F}\left\{I\right\}. \tag{2.24}$$

The Laplacian scales the Fourier spectrum of the migrated image by $(k_x^2 + k_z^2)$, and this attenuates the low-frequency energy and applies a gain to the high-frequency energy.

2.8 Modeling by seismic demigration

Modeling by seismic demigration is an integral part of RWI. The first step towards modeling by seismic demigration is to generate a reflectivity model of the subsurface from the observed data. The reflectivity model, $I(\mathbf{r})$, is given by equation (2.21). Then the demigrated data, equation (2.25), is produced by using the migrated image as a source in depth, in a concept similar to the exploding reflector model. The source term in the wave equation, used to generate the demigrated data, is created by correlating the source wavefield with the migrated image, equation (2.26).

$$d_{cal}(\mathbf{r}_g, t; \mathbf{r}_s) = \delta G(\mathbf{r}_g, t; \mathbf{r}_s), \tag{2.25}$$

where $\delta G(\mathbf{r}_g, \mathbf{r}_s, t)$ is given by

$$\left[\bigtriangledown^2 - \mathbf{m}\frac{\partial^2}{\partial t^2}\right] \delta G(\mathbf{r}, t; \mathbf{r}_s) = I(\mathbf{r})G(\mathbf{r}, t; \mathbf{r}_s). \tag{2.26}$$

In modeling by seismic demigration, the necessary wavefields are measured using a smooth velocity model; hence, the wavefield's ray paths remain unchanged and the source wavefield, $G(\mathbf{r}, t; \mathbf{r}_s)$, is mainly downgoing. The demigrated source wavefield, $\delta G(\mathbf{r}, t; \mathbf{r}_s)$, on the other hand, is an upgoing and downgoing wavefield that only exists when the source wavefield encounters sources in depth. Also, the migrated image, $I(\mathbf{r})$, which serves as a source in depth, is a representation of the zero-offset reflection coefficients. The amplitude versus offset (AVO) effect, in seismic data, is governed by the Zoeppritz equations, which describes a non-linear relationship between reflection coefficients and changes in the physical properties (e.g., P-wave velocity, S-wave velocity and density) of the subsurface (Innanen, 2015). Additionally, the relationship is closely related to Snell's law, which is only dependent on the velocity contrasts in the subsurface. Consequently, modeling by seismic demigration produces data with no AVO information.

2.9 Conclusion

In this chapter, I reviewed the acoustic wave equation, the Clayton-Engquist absorbing boundary conditions, and the wave equation discretization. Also, I covered the stability and dispersion criteria needed to minimize errors in numerical modeling. Afterward, I presented the concept of reverse-time migration. Finally, I reviewed the process of modeling by seismic demigration.

Chapter 3

Theory of reflection-based waveform inversion

3.1 Introduction

Full waveform inversion (FWI) is an ill-posed data-fitting procedure that aims at reconstructing the Earth's physical parameters by iteratively minimizing the least-squares norm of the difference between the predicted and observed data (Lailly, 1983; Tarantola, 1984; Virieux and Operto, 2009). The resolution of the FWI reconstruction is related to the diffraction tomography principle (Devaney, 1982; Miller et al., 1987; Wu and Toksöz, 1987; Brossier et al., 2015); which relates the recoverable wavenumber $\mathbf{k}$, sampled at a point diffractor (Figure 3.1), to the local wavelength and aperture angle θ according to equation (3.1).

$$\mathbf{k} = \frac{4\pi}{\lambda_0} \cos\left(\frac{\theta}{2}\right)\mathbf{n}, \tag{3.1}$$

where λ_0 is the local wavelength, and $\mathbf{n} = \frac{\mathbf{q}_s+\mathbf{q}_r}{\|\mathbf{q}_s+\mathbf{q}_r\|}$ (Figure 3.1).

In a narrow-aperture acquisition geometry, where the depth of investigation is larger than the offset range, the shallow area of the subsurface is sampled by reflections, refractions, and direct waves; while only reflections sample the deep section. According to equation (3.1), in the deep part of the model, due to the small range of θ in narrow-aperture acquisition with smooth background velocity, only high-wavenumbers will be reconstructed; however, in the shallow part both low and high wavenumbers will be reconstructed (Brossier et al., 2015); hence, a successful FWI requires the presence of long-offset data, low frequency data, an accurate starting model, and a good signal-to-noise ratio in the data.

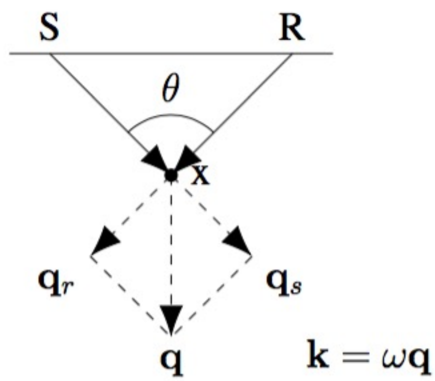

Figure 3.1: Illustration of the relationship between the wavenumber $\mathbf{k}$ and the acquisition geometry for a point diffractor. S denotes source, R denotes receiver, θ is the aperture angle, x is a point diffractor, $\mathbf{q}_s$ and $\mathbf{q}_r$ are the slowness vectors, $\mathbf{q} = \mathbf{q}_s + \mathbf{q}_r$, ω is the angular frequency, and $\mathbf{k}$ is the recoverable wavenumber.

An alternative approach to the conventional FWI, aiming at retrieving the low-wavenumber components of the velocity in areas sampled by reflected data only, was proposed by Xu et al. (2012). It is known as reflection-based waveform inversion (RWI). In this new approach, the velocity model is decomposed into a background/transmission model that I seek to resolve and a reflectivity model that is assumed to be known, allowing the emphasis on the transmission wavepaths of the reflected data in the inversion process. There are three main differences between conventional FWI and RWI. First, the primary goal of RWI is to invert for the background model, and not to obtain a high-resolution model. Second, FWI uses the full wavefield in the inversion process, including direct waves, refracted and reflected waves, while RWI uses only reflected waves. Third, RWI relies on a migration/demigration process (Zhou et al., 2012).

3.2 Derivation

I start by defining two equations in an acoustic medium

$$\left[\bigtriangledown^2 + \omega^2 \mathbf{m}_0\right] G_0(\mathbf{r}_g, \omega; \mathbf{r}_s) = \delta(\mathbf{r}_g - \mathbf{r}_s), \tag{3.2}$$

and

$$\left[\bigtriangledown^2 + \omega^2 \mathbf{m}\right] G(\mathbf{r}_g, \omega; \mathbf{r}_s) = \delta(\mathbf{r}_g - \mathbf{r}_s), \tag{3.3}$$

where $\mathbf{m} = \mathbf{m}_0 + \delta\mathbf{m}$ is the actual subsurface model, $\mathbf{m}_0$ is the background model, $\delta\mathbf{m}$ is the reflectivity model, $G_0(\mathbf{r}_g, \omega; \mathbf{r}_s)$ is the predicted data sampled at $\mathbf{r}_g$ due to a source at $\mathbf{r}_s$, and $G(\mathbf{r}_g, \omega; \mathbf{r}_s)$ is the observed data sampled at $\mathbf{r}_g$ due to a source at $\mathbf{r}_s$. It should be noted that the wave equation is parametrized in terms of the slowness squared, i.e., $\mathbf{m} = \mathbf{c}^{-2}$.

I define the misfit function to be the square of the least-squares norm:

$$E(\mathbf{m}_0) = \frac{1}{2} \sum_{\mathbf{r}_s, \mathbf{r}_g} \int d\omega \; \left\| \delta P(\mathbf{r}_g, \omega; \mathbf{r}_s) \right\|^2, \tag{3.4}$$

where $\delta P(\mathbf{r}_g, \omega; \mathbf{r}_s)$ are the data residuals, equation (3.5).

$$\delta P(\mathbf{r}_g, \omega; \mathbf{r}_s) = G(\mathbf{r}_g, \omega; \mathbf{r}_s) - G_0(\mathbf{r}_g, \omega; \mathbf{r}_s) \tag{3.5}$$

Taking the derivative of equation (3.4) in the vicinity of the model parameter $\mathbf{m}_0$ gives

$$\frac{\partial E(\mathbf{m}_0)}{\partial m_0(\mathbf{r})} = - \sum_{\mathbf{r}_s, \mathbf{r}_g} \int d\omega \, \Re \left\{ \frac{\partial G_0(\mathbf{r}_g, \omega; \mathbf{r}_s)}{\partial m_0(\mathbf{r})} \delta P^*(\mathbf{r}_g, \omega; \mathbf{r}_s) \right\}, \tag{3.6}$$

where

$$g(\mathbf{r}) = \frac{\partial E(\mathbf{m}_0)}{\partial m_0(\mathbf{r})}, \tag{3.7}$$

is the gradient, and $\frac{\partial G_0(\mathbf{r}_g, \omega; \mathbf{r}_s)}{\partial m_0(\mathbf{r})}$ is the sensitivity or Fréchet derivative. The sensitivity describes the changes in the wavefield due to changes in the model parameters.

Substituting $\mathbf{m} = \mathbf{m}_0 + \delta\mathbf{m}$ into equation (3.3) yields

$$\left[\bigtriangledown^2 + \omega^2 \mathbf{m}_0\right] G(\mathbf{r}_g, \omega; \mathbf{r}_s) = \delta(\mathbf{r}_g - \mathbf{r}_s) - \omega^2 \delta m(\mathbf{r}_g) G(\mathbf{r}_g, \omega; \mathbf{r}_s), \tag{3.8}$$

and, by the superposition principle, the solution to equation (3.8) is given by

$$G(\mathbf{r}_g, \omega; \mathbf{r}_s) = \int d\mathbf{r}' G_0(\mathbf{r}_g, \omega; \mathbf{r}') \left[\delta(\mathbf{r}' - \mathbf{r}_s) - \omega^2 \delta m(\mathbf{r}') G(\mathbf{r}', \omega; \mathbf{r}_s)\right], \tag{3.9}$$

allowing the equation for G to be written in integral form as:

$$\begin{aligned} G(\mathbf{r}_g, \omega; \mathbf{r}_s) &= G_0(\mathbf{r}_g, \omega; \mathbf{r}_s) - \omega^2 \int d\mathbf{r}' G_0(\mathbf{r}_g, \omega; \mathbf{r}') \delta m(\mathbf{r}') G(\mathbf{r}', \omega; \mathbf{r}_s), \\ \delta G(\mathbf{r}_g, \omega; \mathbf{r}_s) &= -\omega^2 \int d\mathbf{r}' G_0(\mathbf{r}_g, \omega; \mathbf{r}') \delta m(\mathbf{r}') G(\mathbf{r}', \omega; \mathbf{r}_s). \end{aligned} \tag{3.10}$$

Using a Born series to eliminate $G(\mathbf{r}', \omega; \mathbf{r}_s)$ yields

$$\begin{aligned} &\delta G(\mathbf{r}_g, \omega; \mathbf{r}_s) = -\omega^2 \int d\mathbf{r}' G_0(\mathbf{r}_g, \omega; \mathbf{r}') \delta m(\mathbf{r}') G_0(\mathbf{r}', \omega; \mathbf{r}_s) \\ &+ \omega^4 \int d\mathbf{r}' G_0(\mathbf{r}_g, \omega; \mathbf{r}') \delta m(\mathbf{r}') \int d\mathbf{r}'' G_0(\mathbf{r}', \omega; \mathbf{r}'') \delta m(\mathbf{r}'') G_0(\mathbf{r}'', \omega; \mathbf{r}_s) \\ &+ \dots . \end{aligned} \tag{3.11}$$

Next, I localize the perturbation model $\delta m(\mathbf{r})$ by introducing the delta function so that

$$\delta m(\mathbf{r}') = \delta m \, \delta(\mathbf{r}' - \mathbf{r}), \tag{3.12}$$

which allows us to evaluate the integrals easily. By substituting equation (3.12) into equation (3.11) to obtain

$$\begin{aligned} &\delta G(\mathbf{r}_g, \omega; \mathbf{r}_s) = -\omega^2 G_0(\mathbf{r}_g, \omega; \mathbf{r}) \delta m \, G_0(\mathbf{r}, \omega; \mathbf{r}_s) \\ &+ \omega^4 G_0(\mathbf{r}_g, \omega; \mathbf{r}) \delta m \, G_0(\mathbf{r}, \omega; \mathbf{r}) \delta m \, G_0(\mathbf{r}, \omega; \mathbf{r}_s) + \dots \\ &= -\omega^2 G_0(\mathbf{r}_g, \omega; \mathbf{r}) \delta m \, G_0(\mathbf{r}, \omega; \mathbf{r}_s) [1 - \omega^2 \delta m \, G_0(\mathbf{r}, \omega; \mathbf{r}) + \dots]. \end{aligned} \tag{3.13}$$

Noting that the series expansion of $\frac{1}{1+x}$ is $(1 - x + x^2 - \dots)$, equation (3.13) can be re-written as

$$\begin{aligned} \delta G(\mathbf{r}_g, \omega; \mathbf{r}_s) &= -\frac{\omega^2 G_0(\mathbf{r}_g, \omega; \mathbf{r}) \delta m \, G_0(\mathbf{r}, \omega; \mathbf{r}_s)}{1 + \omega^2 \delta m \, G_0(\mathbf{r}, \omega; \mathbf{r})} \\ \Rightarrow \frac{\delta G(\mathbf{r}_g, \omega; \mathbf{r}_s)}{\delta m} &= -\frac{\omega^2 G_0(\mathbf{r}_g, \omega; \mathbf{r}) G_0(\mathbf{r}, \omega; \mathbf{r}_s)}{1 + \omega^2 \delta m \, G_0(\mathbf{r}, \omega; \mathbf{r})}. \end{aligned} \tag{3.14}$$

Taking the limit so that δm vanishes gives the conventional FWI kernel

$$\frac{\partial G_0(\mathbf{r}_g, \omega; \mathbf{r}_s)}{\partial m_0(\mathbf{r})} = \lim_{\delta m \to 0} \frac{\delta G(\mathbf{r}_g, \omega; \mathbf{r}_s)}{\delta m} = -\omega^2 G_0(\mathbf{r}_g, \omega; \mathbf{r}) G_0(\mathbf{r}, \omega; \mathbf{r}_s). \tag{3.15}$$

In conventional FWI, we tend to resolve and update a velocity model that consists of a background part and a reflectivity part. In other words, to find an updated model $\mathbf{m}_{n+1}$, we need to update a current model $\mathbf{m}_n$, which is composed of a background part and perturbation part, by solving for a model update $\delta\mathbf{m}_n$. However, in RWI we are interested in updating the background part of the velocity model. Taking derivative of equation (3.10) with respect to the background model $\mathbf{m}_0$, to obtain equation (3.16), provides us with the type of update that we seek.

$$\begin{aligned}\frac{\partial \delta G(\mathbf{r}_g,\omega;\mathbf{r}_s)}{\partial m_0(\mathbf{r}'')} = -\omega^2 \int d\mathbf{r}' \Bigg(& \frac{\partial G_0(\mathbf{r}_g,\omega;\mathbf{r}')}{\partial m_0(\mathbf{r}'')} G(\mathbf{r}',\omega;\mathbf{r}_s) \\ & + G_0(\mathbf{r}_g,\omega;\mathbf{r}') \frac{\partial G(\mathbf{r}',\omega;\mathbf{r}_s)}{\partial m_0(\mathbf{r}'')} \Bigg) \delta m(\mathbf{r}').\end{aligned} \tag{3.16}$$

But we have that

$$\frac{\partial G_0(\mathbf{r}_g,\omega;\mathbf{r}')}{\partial m_0(\mathbf{r}'')} = -\omega^2 G_0(\mathbf{r}_g,\omega;\mathbf{r}'') G_0(\mathbf{r}'',\omega;\mathbf{r}'), \tag{3.17}$$

and

$$\frac{\partial G(\mathbf{r}',\omega;\mathbf{r}_s)}{\partial m_0(\mathbf{r}'')} = -\omega^2 G(\mathbf{r}',\omega;\mathbf{r}'') G(\mathbf{r}'',\omega;\mathbf{r}_s), \tag{3.18}$$

so, substituting equations (3.17) and (3.18) into equation (3.16) to obtain

$$\begin{aligned}\frac{\partial \delta G(\mathbf{r}_g,\omega;\mathbf{r}_s)}{\partial m_0(\mathbf{r}'')} = \omega^4 \int d\mathbf{r}' \Bigg(& G_0(\mathbf{r}_g,\omega;\mathbf{r}'') G_0(\mathbf{r}'',\omega;\mathbf{r}') G(\mathbf{r}',\omega;\mathbf{r}_s) \\ & + G_0(\mathbf{r}_g,\omega;\mathbf{r}') G(\mathbf{r}',\omega;\mathbf{r}'') G(\mathbf{r}'',\omega;\mathbf{r}_s) \Bigg) \delta m(\mathbf{r}').\end{aligned} \tag{3.19}$$

By re-writing equation (3.19) as

$$\begin{aligned}\frac{\partial \delta G(\mathbf{r}_g,\omega;\mathbf{r}_s)}{\partial m_0(\mathbf{r}'')} = & -\omega^2 G_0(\mathbf{r}_g,\omega;\mathbf{r}'') \left[-\omega^2 \int d\mathbf{r}' G_0(\mathbf{r}'',\omega;\mathbf{r}') \delta m(\mathbf{r}') G(\mathbf{r}',\omega;\mathbf{r}_s) \right] \\ & - \omega^2 G(\mathbf{r}'',\omega;\mathbf{r}_s) \left[-\omega^2 \int d\mathbf{r}' G_0(\mathbf{r}_g,\omega;\mathbf{r}') \delta m(\mathbf{r}') G(\mathbf{r}',\omega;\mathbf{r}'') \right],\end{aligned} \tag{3.20}$$

the expressions within $[\cdot]$ can be replaced by the perturbed wavefield, equation (3.10), giving, finally

$$\frac{\partial \delta G(\mathbf{r}_g,\omega;\mathbf{r}_s)}{\partial m_0(\mathbf{r}'')} = -\omega^2 \Bigg(G_0(\mathbf{r}_g,\omega;\mathbf{r}'') \delta G(\mathbf{r}'',\omega;\mathbf{r}_s) + \delta G(\mathbf{r}_g,\omega;\mathbf{r}'') G(\mathbf{r}'',\omega;\mathbf{r}_s) \Bigg), \tag{3.21}$$

where $\frac{\partial \delta G(\mathbf{r}_g,\omega;\mathbf{r}_s)}{\partial m_0(\mathbf{r}'')}$ is the RWI kernel. In equation (3.21), $G(\mathbf{r}'',\omega;\mathbf{r}_s)$ corresponds to the actual source wavefield, however, since obtaining the actual source wavefield is not possible, it is replaced with the modeled source wavefield $G_0(\mathbf{r}'',\omega;\mathbf{r}_s)$. The gradient of the misfit function with respect to the background model $\mathbf{m}_0$ is obtained by substituting equation (3.21) into equation (3.6) to give

$$\begin{aligned} g(\mathbf{r}) = \sum_{\mathbf{r}_s,\mathbf{r}_g} \int d\omega\, \omega^2 \Bigg(& \Big[\delta G(\mathbf{r},\omega;\mathbf{r}_s)\Big] \times \Big[G_0(\mathbf{r},\omega;\mathbf{r}_g)\delta P^*(\mathbf{r}_g,\omega;\mathbf{r}_s)\Big] \\ & + \Big[G_0(\mathbf{r},\omega;\mathbf{r}_s)\Big] \times \Big[\delta G(\mathbf{r},\omega;\mathbf{r}_g)\delta P^*(\mathbf{r}_g,\omega;\mathbf{r}_s)\Big]\Bigg), \end{aligned} \tag{3.22}$$

where $\delta G(\mathbf{r},\omega;\mathbf{r}_s)$ is the demigrated source wavefield, $G_0(\mathbf{r},\omega;\mathbf{r}_g)$ is the receiver wavefield, $G_0(\mathbf{r},\omega;\mathbf{r}_s)$ is the source wavefield, $\delta G(\mathbf{r},\omega;\mathbf{r}_g)$ is the demigrated receiver wavefield, and $\delta P^*(\mathbf{r}_g,\omega;\mathbf{r}_s)$ is the complex conjugate of the data residual. Equation (3.22) depends on both the background model and the perturbation model (through $\delta G(\mathbf{r},\omega;\mathbf{r}_s)$ and $\delta G(\mathbf{r},\omega;\mathbf{r}_g)$).

The corresponding equation in time domain to equation (3.22) is given by

$$\begin{aligned} g(\mathbf{r}) = \sum_{\mathbf{r}_s,\mathbf{r}_g} \int_0^T dt \Bigg(& \Big[\delta \ddot{G}(\mathbf{r},t;\mathbf{r}_s)\Big] \Big[G_0(\mathbf{r},T-t;\mathbf{r}_g) * \delta P(\mathbf{r}_g,T-t;\mathbf{r}_s)\Big] \\ & + \Big[\ddot{G}_0(\mathbf{r},t;\mathbf{r}_s)\Big] \Big[\delta G(\mathbf{r},T-t;\mathbf{r}_g) * \delta P(\mathbf{r}_g,T-t;\mathbf{r}_s)\Big]\Bigg), \end{aligned} \tag{3.23}$$

where $\big[G_0(\mathbf{r},T-t;\mathbf{r}_g) * \delta P(\mathbf{r}_g,T-t;\mathbf{r}_s)\big]$ is the back-propagated data residual wavefield, $\big[\delta G(\mathbf{r},T-t;\mathbf{r}_g) * \delta P(\mathbf{r}_g,T-t;\mathbf{r}_s)\big]$ is the demigrated receiver wavefield, $\ddot{G}$ corresponds to the second time derivative of G, and $*$ represents convolution. The parametrization of the gradient (equations 3.22 and 3.23) is in terms of slowness squared $\left(m(\mathbf{r}) = \frac{1}{v(\mathbf{r})^2}\right)$.

3.3 Sensitivity Kernels

To understand the advantage of model decomposition, I investigate the contribution of direct and reflected waves to the FWI and the RWI sensitivity kernels. The sensitivity kernel describes the perturbation in the data domain due to a perturbation in the model parameter

(Chi et al., 2015). Equation (3.15) is the conventional FWI sensitivity kernel in the frequency domain. The corresponding FWI kernel in the time domain, $\mathbf{K}_{FWI}$, is given by the cross-correlation of the second time derivative of the source wavefield with the time-reversed back-propagated receiver wavefield:

$$\mathbf{K}_{FWI} = \ddot{G}(\mathbf{r}, t; \mathbf{r}_s) \otimes G(\mathbf{r}, -t; \mathbf{r}_g), \tag{3.24}$$

where $G(\mathbf{r}, t; \mathbf{r}_g)$ satisfies

$$\begin{cases} \left[\bigtriangledown^2 - \mathbf{m}\frac{\partial^2}{\partial t^2}\right] G(\mathbf{r}, t; \mathbf{r}_g) = 0 \\ G(\mathbf{r}_s, t; \mathbf{r}_g) = G(\mathbf{r}_g, t; \mathbf{r}_s), \end{cases} \tag{3.25}$$

and $G(\mathbf{r}, t; \mathbf{r}_s)$ satisfies

$$\left[\bigtriangledown^2 - \mathbf{m}\frac{\partial^2}{\partial t^2}\right] G(\mathbf{r}, t; \mathbf{r}_s) = \delta(\mathbf{r} - \mathbf{r}_s), \tag{3.26}$$

and where $G(\mathbf{r}_g, t; \mathbf{r}_s)$ is the recorded data. The sensitivity kernel of RWI in the frequency domain is given by equation (3.21), and the corresponding kernel in time domain, $\mathbf{K}_{RWI}$, is given by

$$\mathbf{K}_{RWI} = \delta\ddot{G}(\mathbf{r}, t; \mathbf{r}_s) \otimes G(\mathbf{r}, -t; \mathbf{r}_g) + \ddot{G}(\mathbf{r}, t; \mathbf{r}_s) \otimes \delta G(\mathbf{r}, -t; \mathbf{r}_g), \tag{3.27}$$

where $\delta\ddot{G}(\mathbf{r}, t; \mathbf{r}_s)$ is the second time derivative of the demigrated source wavefield, $G(\mathbf{r}, -t; \mathbf{r}_g)$ is the time reversed receiver wavefield, $\ddot{G}(\mathbf{r}, t; \mathbf{r}_s)$ is the second time derivative of the source wavefield, and $\delta G(\mathbf{r}, -t; \mathbf{r}_g)$ is the demigrated receiver wavefield.

To construct example FWI and RWI sensitivity kernels, I use a two-layer model, where the velocity of the first layer is $2000\, m/s$ and the velocity of the second layer is $3000\, m/s$, and the interface is at $0.6\, km$ depth. In this model, a source is placed at $(0.33, 0.33)\, km$ and a receiver is placed at $(0.66, 0.33)\, km$, (Figure 3.2). In constructing the sensitivity kernels, I use the full bandwidth by utilizing the time domain form of the kernels.

Analyzing the conventional FWI sensitivity sub-kernels (Figures 3.3a, 3.3b, and 3.3c) indicates that with a smooth initial model, early iterations will update the low-wavenumber components in the shallow part of the model (Figure 3.3a), and will update the high-wavenumber components in the deep part of the model, (Figure 3.3b), (Chi et al., 2015).

Figure (3.3b) indicates that the high-wavenumber update, in the deep section, will exhibit a migration-like reconstruction (Brossier et al., 2015).

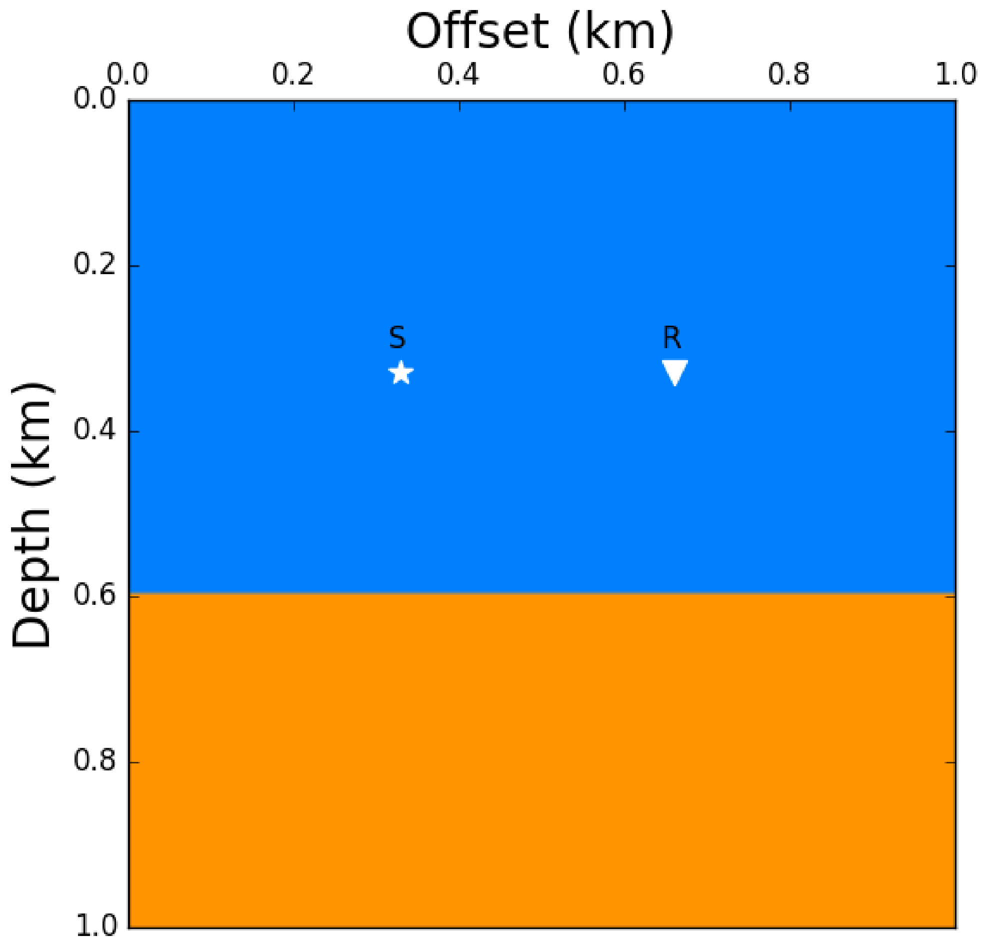

Figure 3.2: Velocity model used to generated sensitivity kernels. The velocity of the first layer is 2000 m/s and the velocity of the second layer is 3000 m/s. S, ☆, denotes the source and R, ▽, denotes the receiver.

Such behavior in the inversion process is a result of the absence of reflected waves in the predicted data at early iterations. As the number of iterations increases, low-wavenumber components in the deep part will start to update (Figure 3.3c); however, the high-wavenumber contribution is stronger; hence, the inversion process will try to match the predicted and observed data by updating the high-wavenumber components (Chi et al., 2015). On the other hand, the predicted data in RWI will contain reflected waves, as it is generated through a migration/demigration process (Zhou et al., 2012). The RWI sensitivity kernel indicates that the reflected waves contribute towards updating the background model (Figure 3.3d).

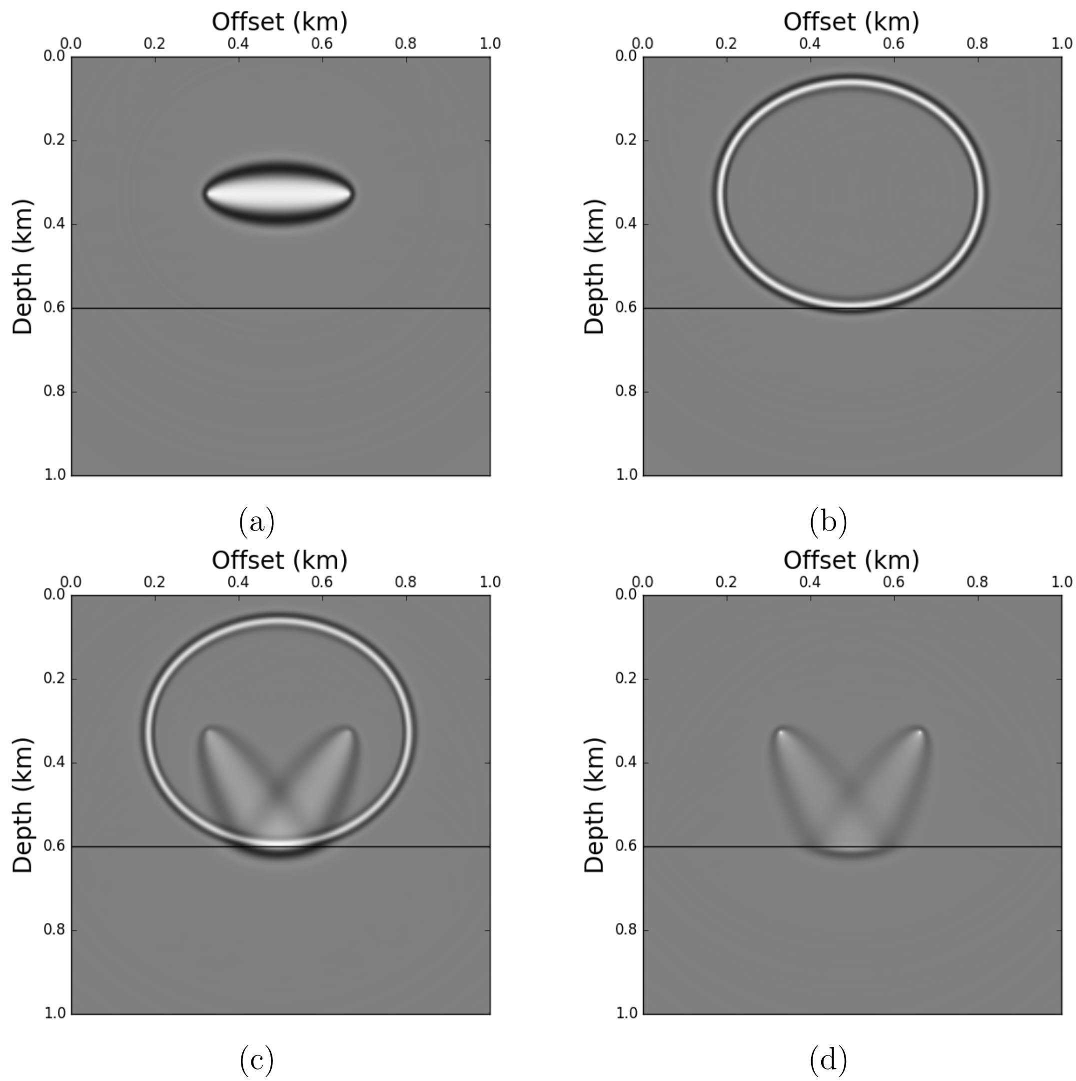

Figure 3.3: FWI and RWI sensitivity kernels. (a) FWI direct wave sub-kernel. (b) Migration ellipse. This is the FWI reflected wave sub-kernel when model is smooth and does not contain reflectivity information. (c) FWI reflected wave sub-kernel. (d) RWI sensitivity kernel. I use a Ricker wavelet as a source function and the full bandwidth in generating the sensitivity kernels. The solid line is the interface between the two media.

3.4 RWI workflow

In this section, I present the RWI workflow. The first step in RWI is to perform an RTM to generate an image, $I(\mathbf{r})$, of the subsurface, as follows

$$\left[\nabla^2 - \mathbf{m}\frac{\partial^2}{\partial t^2}\right] G(\mathbf{r}, t; \mathbf{r}_s) = f(t), \tag{3.28}$$

$$\begin{cases} \left[\nabla^2 - \mathbf{m}\frac{\partial^2}{\partial t^2}\right] G(\mathbf{r}, t; \mathbf{r}_g) = 0 \\ G(\mathbf{r}_s, t; \mathbf{r}_g) = G(\mathbf{r}_g, t; \mathbf{r}_s), \end{cases} \tag{3.29}$$

$$I(\mathbf{r}) = G(\mathbf{r}, t; \mathbf{r}_s) \otimes G(\mathbf{r}, -t; \mathbf{r}_g). \tag{3.30}$$

Next, the migrated image, equation (3.30), and the source wavefield, equation (3.28), are used to compute the predicted data by modeling by seismic demigration, according to

$$\left[\nabla^2 - \mathbf{m}\frac{\partial^2}{\partial t^2}\right] \delta G(\mathbf{r}, t; \mathbf{r}_s) = I(\mathbf{r}) G(\mathbf{r}, t; \mathbf{r}_s). \tag{3.31}$$

From the observed and predicted data we obtain the data residual

$$\delta P(\mathbf{r}_g, t; \mathbf{r}_s) = G(\mathbf{r}_g, t; \mathbf{r}_s) - \delta G(\mathbf{r}_g, t; \mathbf{r}_s). \tag{3.32}$$

Afterwards, the data residual wavefield is computed as follows

$$\begin{cases} \left[\nabla^2 - \mathbf{m}\frac{\partial^2}{\partial t^2}\right] G(\mathbf{r}, t; \mathbf{r}_g) = 0 \\ G(\mathbf{r}_s, t; \mathbf{r}_g) = \delta P(\mathbf{r}_g, t; \mathbf{r}_s). \end{cases} \tag{3.33}$$

Next, the data residual wavefield is demigrated according to

$$\left[\nabla^2 - \mathbf{m}\frac{\partial^2}{\partial t^2}\right] \delta G(\mathbf{r}, t; \mathbf{r}_g) = I(\mathbf{r}) G(\mathbf{r}, t; \mathbf{r}_g). \tag{3.34}$$

Afterwards, we calculate the source and receiver sides of the gradient as follows

$$K_g(\mathbf{r}) = \sum_{\mathbf{r}_s, \mathbf{r}_g} \delta \ddot{G}(\mathbf{r}, t; \mathbf{r}_s) \otimes G(\mathbf{r}, -t; \mathbf{r}_g), \tag{3.35}$$

$$K_s(\mathbf{r}) = \sum_{\mathbf{r}_s, \mathbf{r}_g} \ddot{G}(\mathbf{r}, t; \mathbf{r}_s) \otimes \delta G(\mathbf{r}, -t; \mathbf{r}_g), \tag{3.36}$$

where $\delta\ddot{G}(\mathbf{r}, t; \mathbf{r}_s)$ is the second time derivative of the demigrated source wavefield, $G(\mathbf{r}, t; \mathbf{r}_g)$ is the data residual receiver wavefield, $\ddot{G}(\mathbf{r}, t; \mathbf{r}_s)$ is the second time derivative of the source wavefield, and $\delta G(\mathbf{r}, t; \mathbf{r}_g)$ is the demigrated data residual receiver wavefield. Finally, the RWI gradient is obtained by combining $K_s(\mathbf{r})$ and $K_g(\mathbf{r})$, equation (3.37). In Figure (3.4) the RWI workflow is shown.

$$g(\mathbf{r}) = K_s(\mathbf{r}) + K_g(\mathbf{r}). \tag{3.37}$$

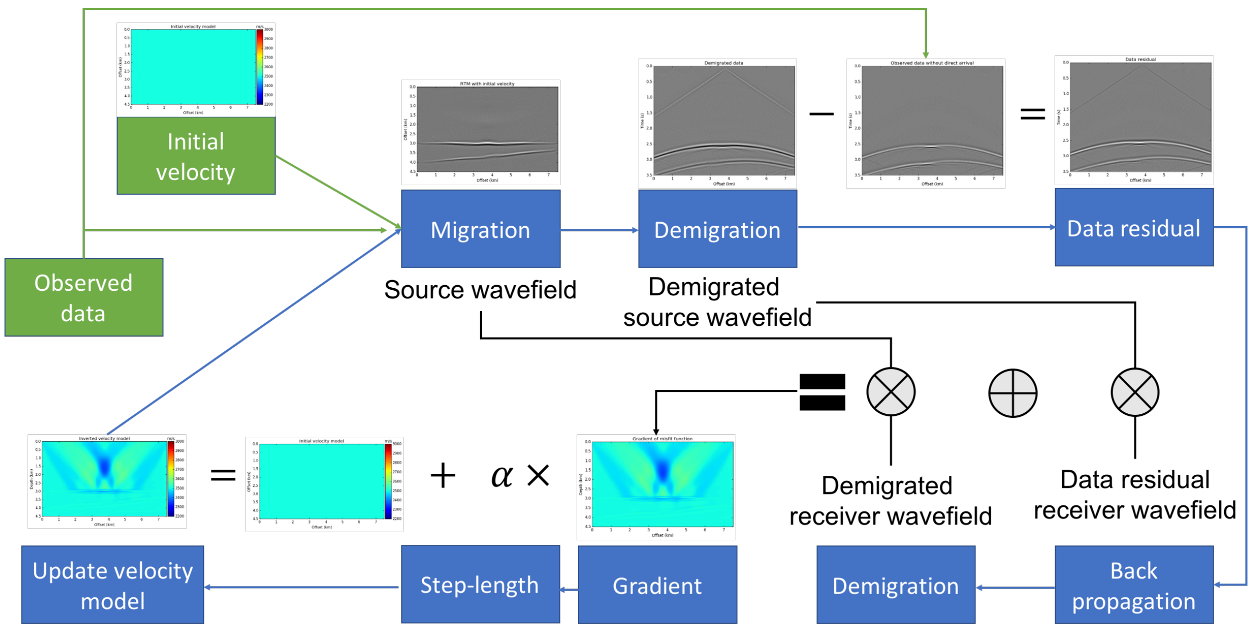

Figure 3.4: RWI workflow.

3.5 Understanding the RWI gradient

In this section, I discuss the mechanisms, through which RWI constructs the long-wavelength components of the velocity model. First, I state the FWI gradient and restate the source and receiver sides of the RWI gradient, equations (3.35) and (3.36), as follows

$$K_{FWI}(\mathbf{r}) = \sum_{\mathbf{r}_s, \mathbf{r}_g} \ddot{G}_s \otimes G_g, \tag{3.38}$$

$$K_g(\mathbf{r}) = \sum_{\mathbf{r}_s, \mathbf{r}_g} \delta\ddot{G}_s \otimes G_g, \tag{3.39}$$

$$K_s(\mathbf{r}) = \sum_{\mathbf{r}_s, \mathbf{r}_g} \ddot{G}_s \otimes \delta G_g, \tag{3.40}$$

where $\delta\ddot{G}_s = \delta\ddot{G}(\mathbf{r}, t; \mathbf{r}_s)$, $G_g = G(\mathbf{r}, -t; \mathbf{r}_g)$, $\ddot{G}_s = \ddot{G}(\mathbf{r}, t; \mathbf{r}_s)$, and $\delta G_g = \delta G(\mathbf{r}, -t; \mathbf{r}_g)$. To illustrate how the gradient is formed in RWI, I use a two-layer model, with one source placed at $(x, z) = (0.5, 0.2)\,km$ and one receiver placed at $(x, z) = (1.5, 0.2)\,km$ (Figure 3.5). The velocity of the first layer is $2000\,m/s$ and the velocity of the second layer is $3000\,m/s$. To calculate the wavefields I use a constant velocity model, where the velocity is $2000\,m/s$.

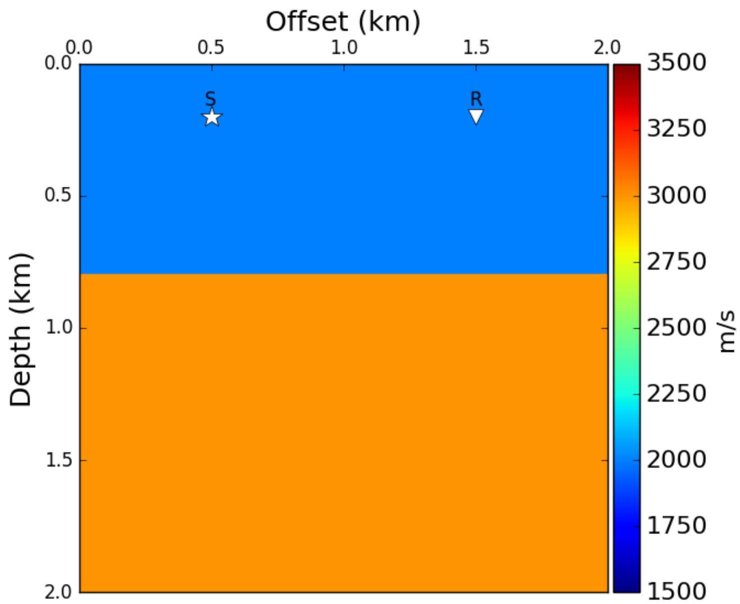

Figure 3.5: Velocity model used to analysis the RWI gradient. The velocity of the first layer is $2000\,m/s$ and the velocity of the second layer is $3000\,m/s$. S, $\star$, denotes the source and R, $\bigtriangledown$, denotes the receiver.

In FWI, the initial velocity model and the early iterations inverted velocity do not contain any significant reflectivity information. As a consequence, the computed source, $\ddot{G}_s$, and receiver, G_r, wavefields are strictly downgoing and upgoing wavefields, respectively. Hence, the FWI kernel, equation (3.38), will produce a migration-like update (Figure 3.6).

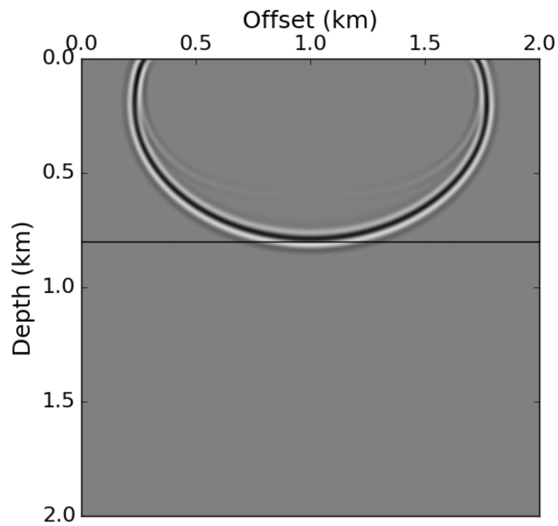

Figure 3.6: FWI kernel. The solid line is the interface between the two media.

Similarly, in RWI, the initial and inverted velocity models are smooth models that do not generate reflected waves. However, decomposing the velocity model, into a background part and a reflectivity part, which influences the residuals via seismic demigration, will result in reflected waves contributing to updating the long-wavelength components of the velocity model. In RWI, the demigrated wavefields explode when the wavefields encounter sources in depth.

In Figures (3.7a) and (3.7b) the source and demigrated source wavefields at time $t = 0.5\,s$ are plotted, respectively. As stated above, the source wavefield, $\ddot{G}_s$, is a downgoing wavefield (Figure 3.7a); however, the demigrated source wavefield is comprised of upgoing and downgoing components. The upgoing wavefield forms above reflectors, and the downgoing wavefield forms below reflectors in the demigrated wavefield. In Figures (3.8a) and (3.8b) the receiver and the demigrated receiver wavefields at time $t = 0.5\,s$ are plotted, respectively. Similar to the demigrated source wavefield, the demigrated receiver wavefield is comprised of upgoing and downgoing waves. The source-side kernel (Figure 3.9a) is formed by cross-correlating the demigrated receiver wavefield with the source wavefield, equation (3.40). The long-wavelength component in the kernel forms, as a result of cross-correlating wavefields of the same type, downgoing wavefields. In Figure (3.9b) the receiver-side of the RWI kernel is plotted. Similar to the source-side of the kernel, the receiver kernel constructs the long-wavelength component by cross-correlating wavefields of the same type, upgoing wavefields. Combining the source- and receiver-side kernels give the RWI kernel (Figure 3.10).

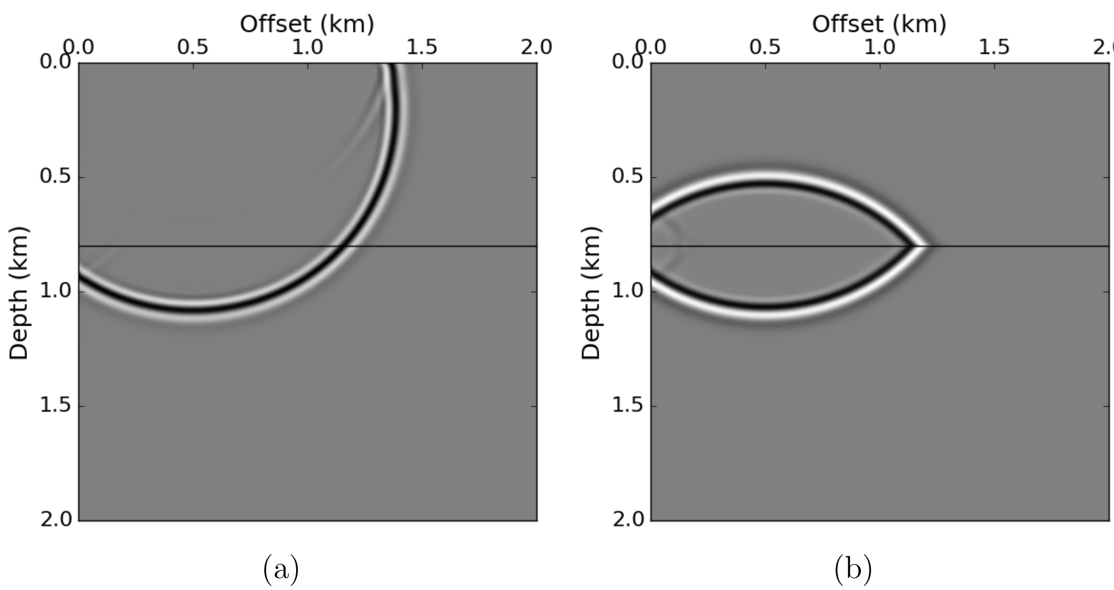

Figure 3.7: Snapshot at time $t = 0.5\,s$ of (a) the source wavefield and (b) the demigrated source wavefield. The solid line is the interface between the two media.

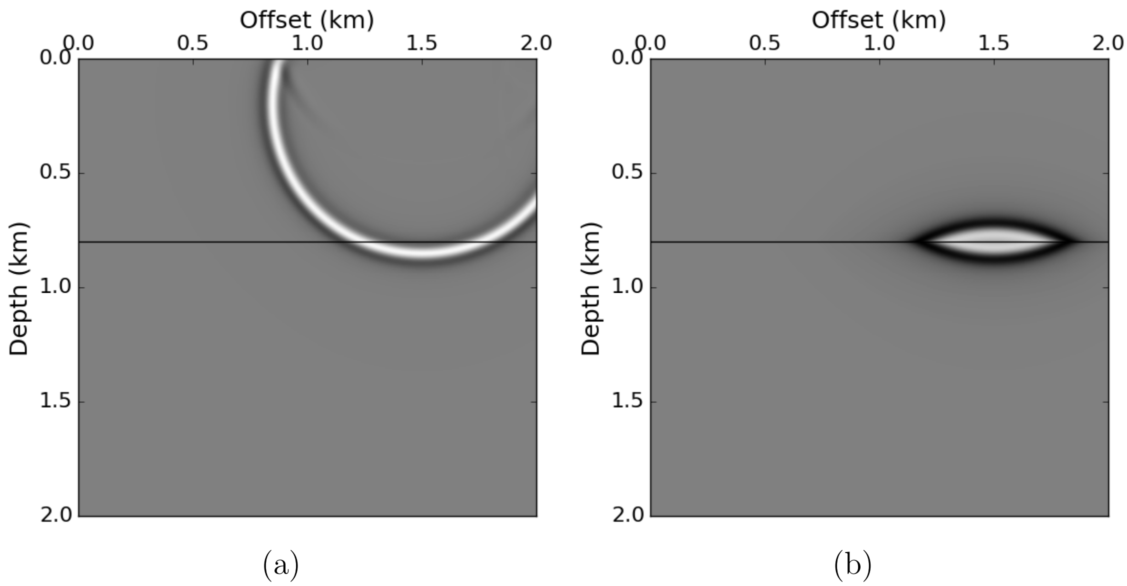

Figure 3.8: Snapshot at time $t = 0.5\,s$ of (a) the receiver wavefield and (b) the demigrated receiver wavefield. The solid line is the interface between the two media.

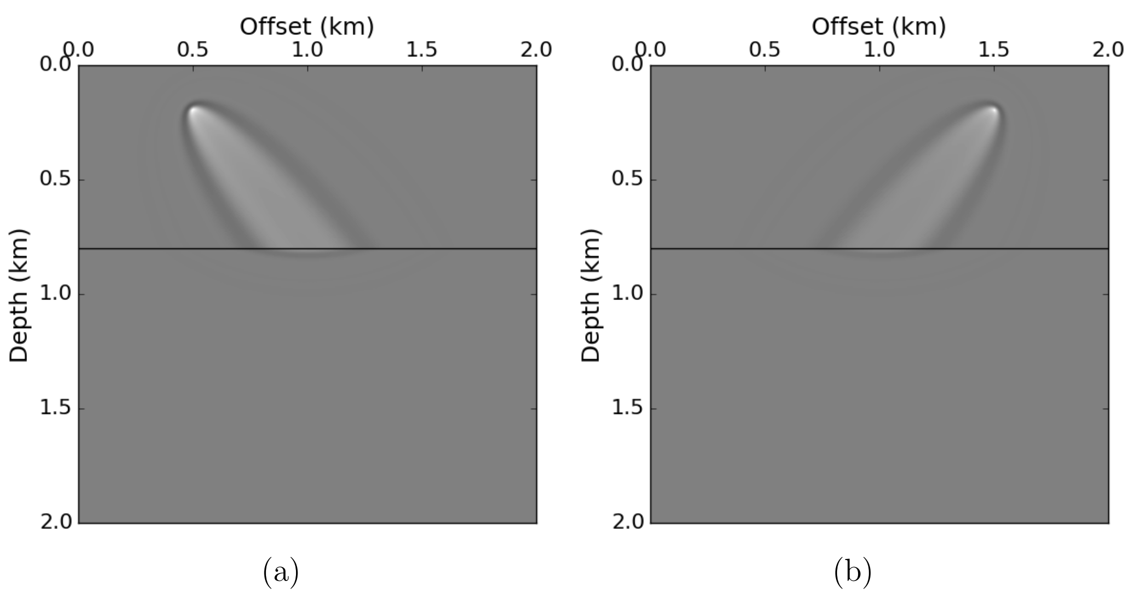

Figure 3.9: (a) Source-side and (b) receiver-side of the RWI kernel. The solid line is the interface between the two media.

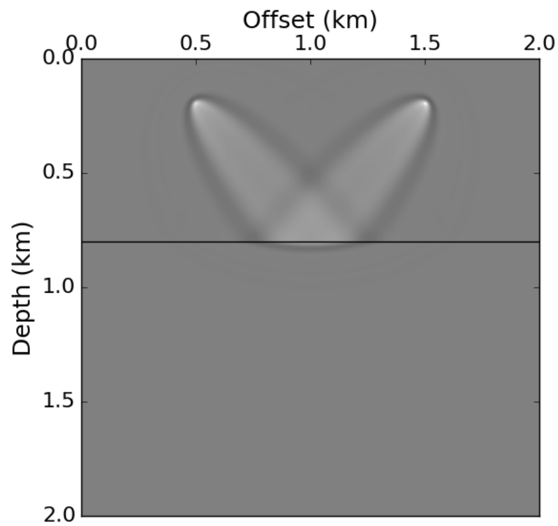

Figure 3.10: RWI kernel. The solid line is the interface between the two media.

3.6 Conclusion

In this chapter, I covered the derivation and basic character of the RWI gradient. I discussed the advantage of RWI over FWI in retrieving the background part of the velocity model when recorded data lacks sufficient low-frequency information. Afterward, I presented the RWI workflow. Finally, I reviewed the process at which RWI constructs the long-wavelength components, in the gradient, from reflection data.

Chapter 4

RWI in simple media

4.1 Introduction

Our objective in this chapter is to examine in as simple a manner as possible, the way RWI retrieves the long wavelength components of the velocity model. Moreover, I explore the effects of correcting for source-receiver illumination within the gradient, which is equivalent to applying the diagonal of the Hessian (Plessix and Mulder, 2004; Shin et al., 2001), on the inversion results. In order to carry out these experiments, RWI codes in Python complementing the finite difference codes were written from scratch. An outcome of this thesis, in addition to the aspects of RWI I study in detail, is a set of simple codes with which other questions and issues pertaining to RWI can be addressed.

4.2 Modeling

For this analysis, I use a slightly modified version of the model used by Wang et al. (2013). It is a three-layer model of dimension $7500\,m \times 4500\,m$ (Figure 4.1). The model is composed of a background velocity of $2500\,m/s$ with a non-reflective low-velocity Gaussian anomaly. The center of the anomaly has a velocity of $2200\,m/s$. The first interface is a horizontal reflector located at $3000\,m$ in depth, with a velocity of $2750\,m/s$. The second interface is a dipping reflector with a velocity of $3000\,m/s$. The second layer varies from $375\,m$ to $1125\,m$ in thickness. A constant velocity model is used as an initial model with a velocity of $2500\,m/s$ (Figure 4.2). In Figure (4.4) a vertical velocity profile across the center of the model, at $x = 3750\,m$, is plotted for both the true and the initial velocity models.

For the acquisition, fifty shots were used in this experiment, with the first shot at $x = 75\,m$

and the last shot at $x = 7425\,m$, with a shot spacing of $150\,m$. There are 500 receivers with $15\,m$ spacing. The depth of all sources and receivers is $15\,m$. The recording time is $3.5\,s$ with a $3.0\,ms$ time interval. The source wavelet is a Ricker wavelet with $10\,Hz$ dominant frequency. RWI is formulated such that the inversion is only applicable to reflection-only data; hence, I mute direct arrivals in the observed data. A sample of the observed data at $x = 3675\,m$ is plotted in Figure (4.3), where the effect of the Gaussian anomaly on the reflected waves can be observed. Table (4.1) summarizes the acquisition geometry and the model parameters.

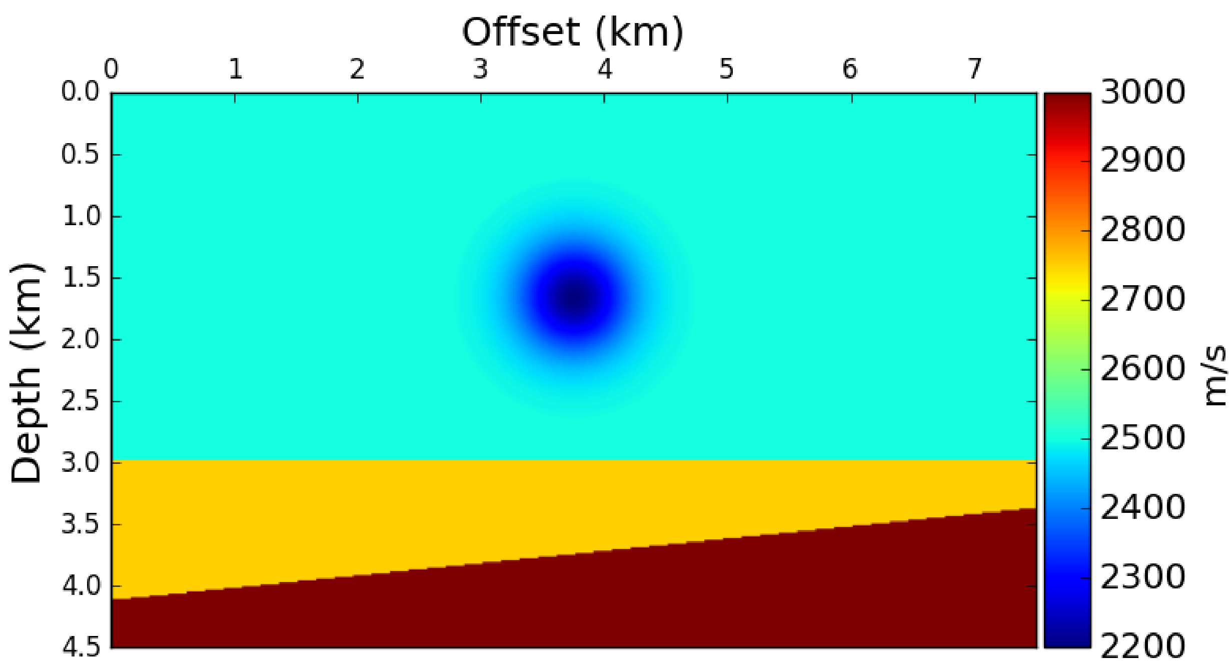

Figure 4.1: True velocity model.

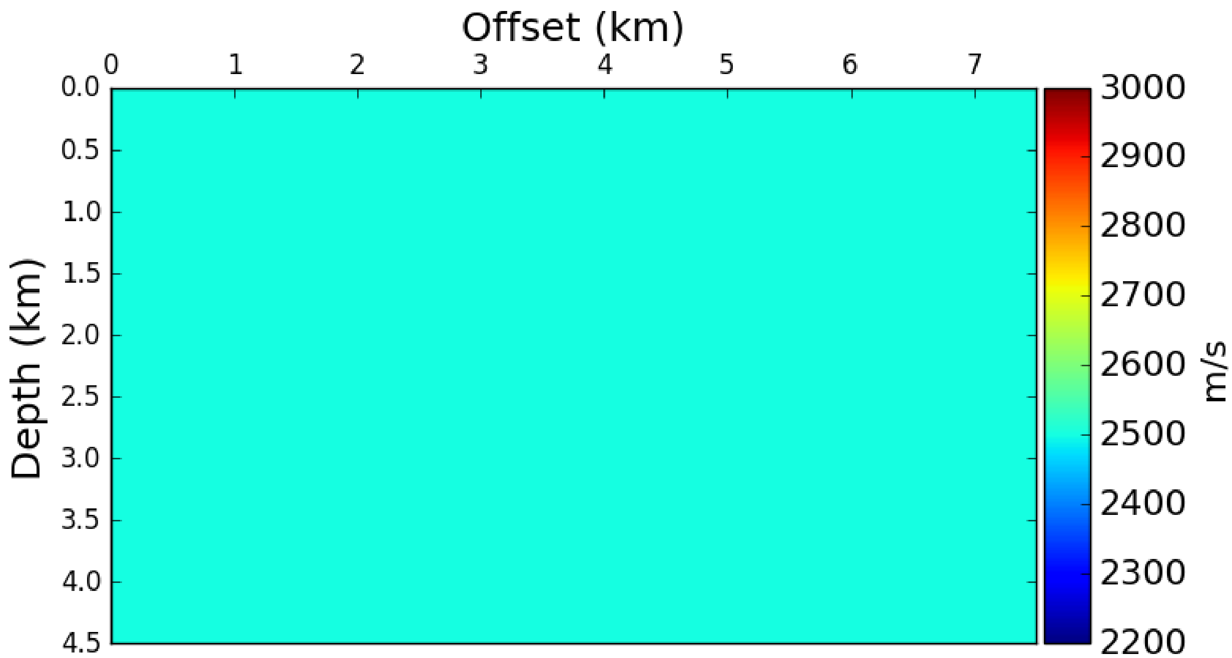

Figure 4.2: Initial velocity model.

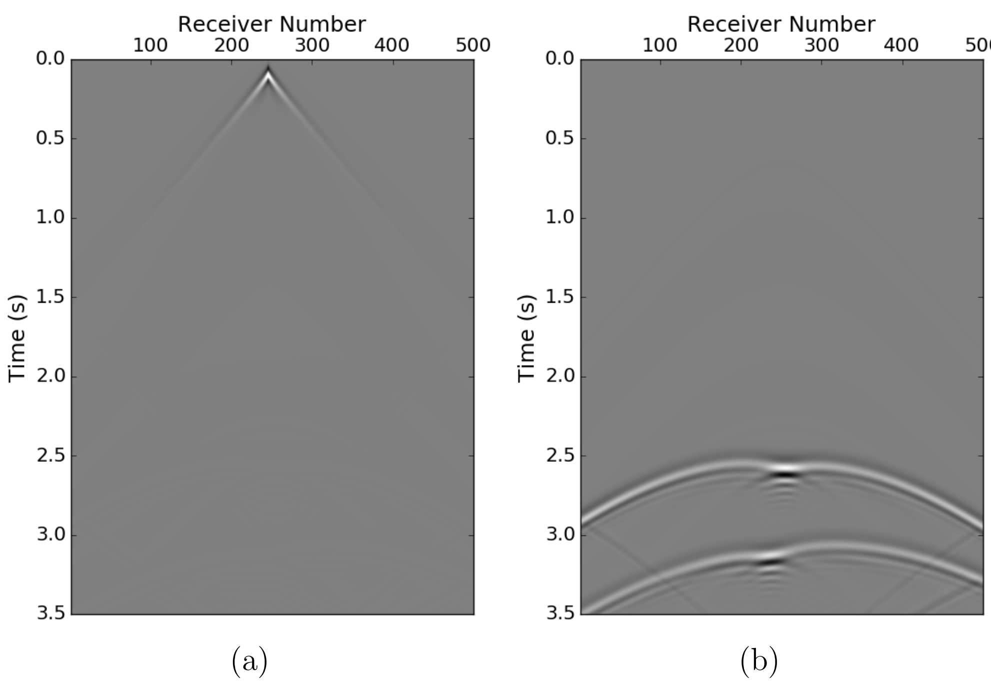

Figure 4.3: Observed data at $x = 3675\,m$ (a) with direct arrivals and (b) without direct arrivals.

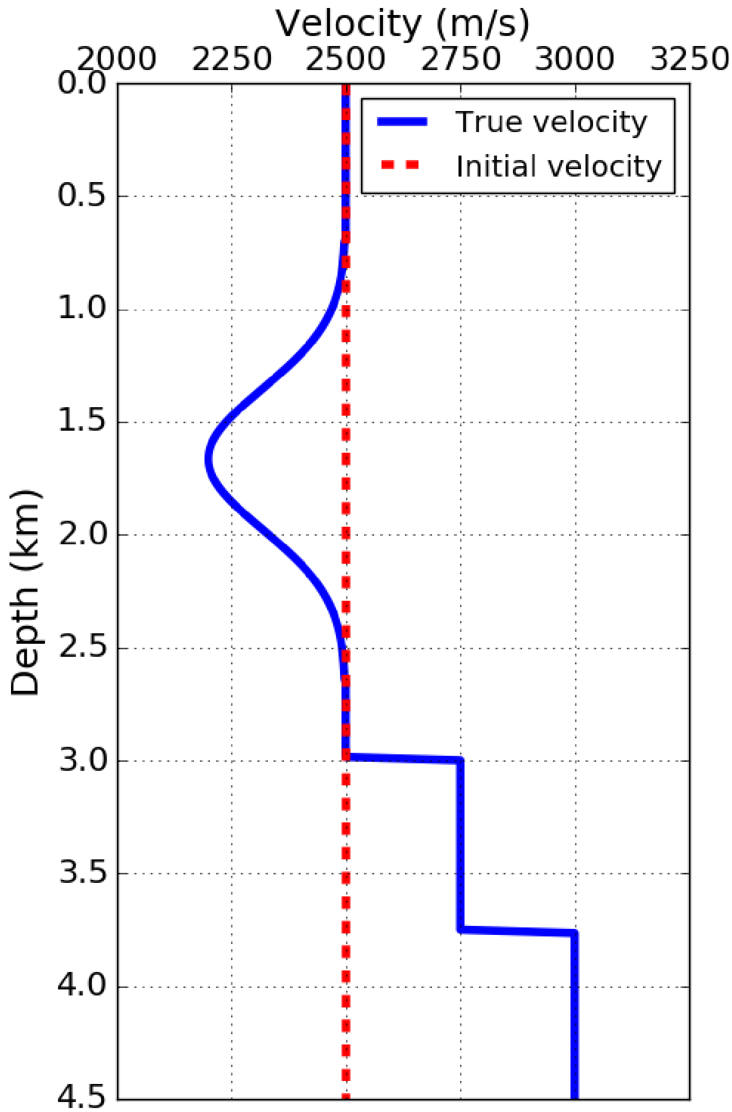

Figure 4.4: Vertical velocity profile at $x = 3750\,m$ for the true and initial velocity models.

Acquisition geometry and model parameters			
nx	501	nz	301
dx	15.0 m	dt	3.0 ms
t_{max}	3.5 s	nt	1166
Source x_0	75 m	Source x_{end}	7425 m
Receiver x_0	15 m	Receiver x_{end}	7500 m
Shot spacing	150 m	Receiver spacing	15 m
Number of shots	50	Number of receivers	500
Depth of shots	15 m	Depth of receiver	15 m

Table 4.1: Acquisition geometry and model parameters.

4.3 Inversion

4.3.1 RWI equations

In this section, I present the set of equations used to generate the source wavefield and the data residuals receiver wavefield used in the gradient calculation, equations (3.35 and 3.36), and the source and the receiver wavefields needed to migrate the observed data, equation (3.30). The equation used to generate the source wavefield, used in the gradient calculation, is given by

$$\left[\bigtriangledown^2 - \mathbf{m}\frac{\partial^2}{\partial t^2}\right] G(\mathbf{r}, t; \mathbf{r}_s) = f(t), \tag{4.1}$$

and the data residuals receiver wavefield equation, used in the gradient calculation, is

$$\left[\bigtriangledown^2 - \mathbf{m}\frac{\partial^2}{\partial t^2}\right] G(\mathbf{r}, t; \mathbf{r}_g) = \delta P(\mathbf{r}, t; \mathbf{r}_g). \tag{4.2}$$

The source wavefield equation used to produce the RTM image is

$$\begin{cases} \left[\bigtriangledown^2 - \mathbf{m}\frac{\partial^2}{\partial t^2}\right] G(\mathbf{r}, t; \mathbf{r}_s) = 0 \\ G(\mathbf{r}, t; \mathbf{r}_s) = \int_0^t dt' f(t'), \end{cases} \tag{4.3}$$

and the equation used to calculate the receiver wavefield needed for the RTM is

$$\begin{cases} \left[\nabla^2 - \mathbf{m}\frac{\partial^2}{\partial t^2}\right] G(\mathbf{r}, t; \mathbf{r}_g) = 0 \\ G(\mathbf{r}_s, t; \mathbf{r}_g) = G(\mathbf{r}_g, t; \mathbf{r}_s). \end{cases} \tag{4.4}$$

The equations used to calculate the demigrated source and demigrated receiver wavefields remain unchanged, equations (3.31) and (3.34). According to Zhang and Sun (2009), equation (4.3) is the proper choice when calculating the true-amplitude angle domain common image gathers, when using the cross-correlation imaging condition, equation (3.30). This set of equations provide the correct results for the model tested in this chapter, keeping in mind that the solution is known. In a later section, I show that this set of equations is the only set working for the model presented in this chapter.

4.3.2 Without source-receiver illumination compensation

In this section, I examine the RWI results for gradients with no source-receiver illumination compensation applied to them. In Figure (4.5) the RTM migrated image using the initial velocity model (Figure 4.2) is plotted. Due to the inaccuracy of the velocity model, the horizons are unfocused and false structures are present.

In Figure (4.6) the RWI gradient for the first iteration is plotted. The update information in the gradient is mainly for the first layer, and updates below that hardly can be seen. Still, the gradient captures the general characteristics of the true velocity model.

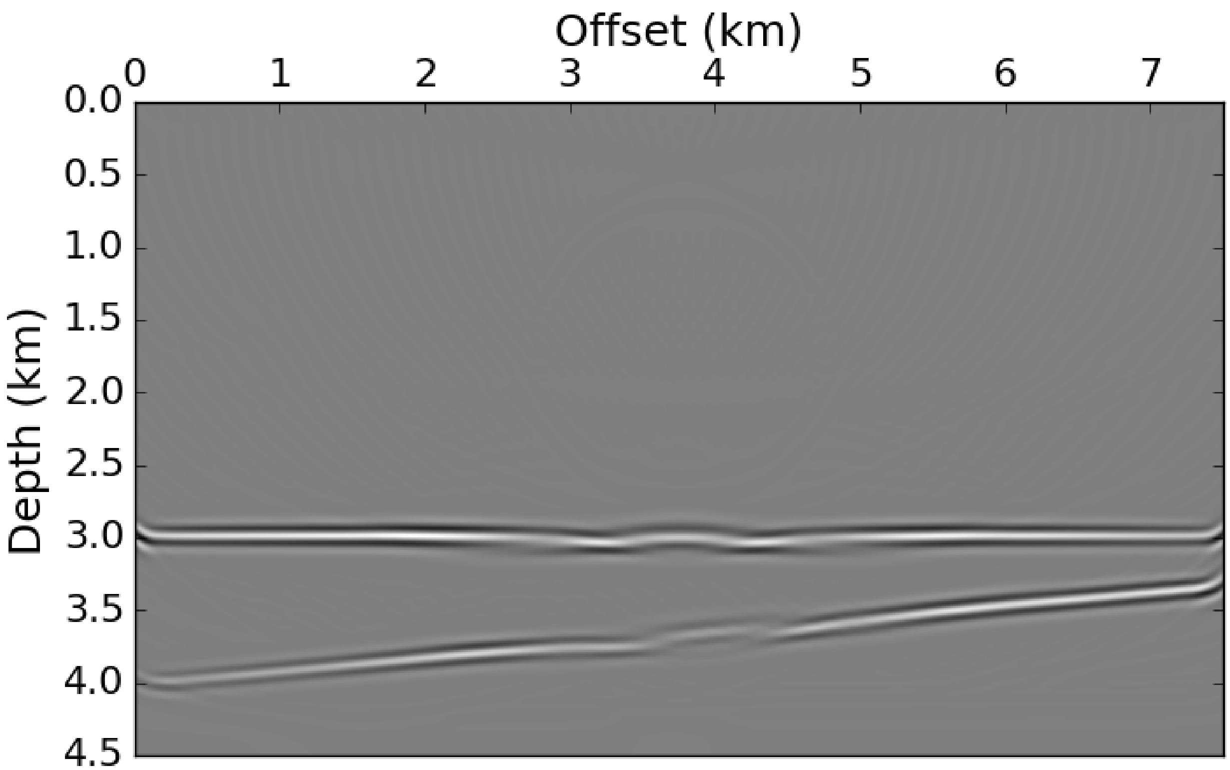

Figure 4.5: RTM image migrated using the initial velocity.

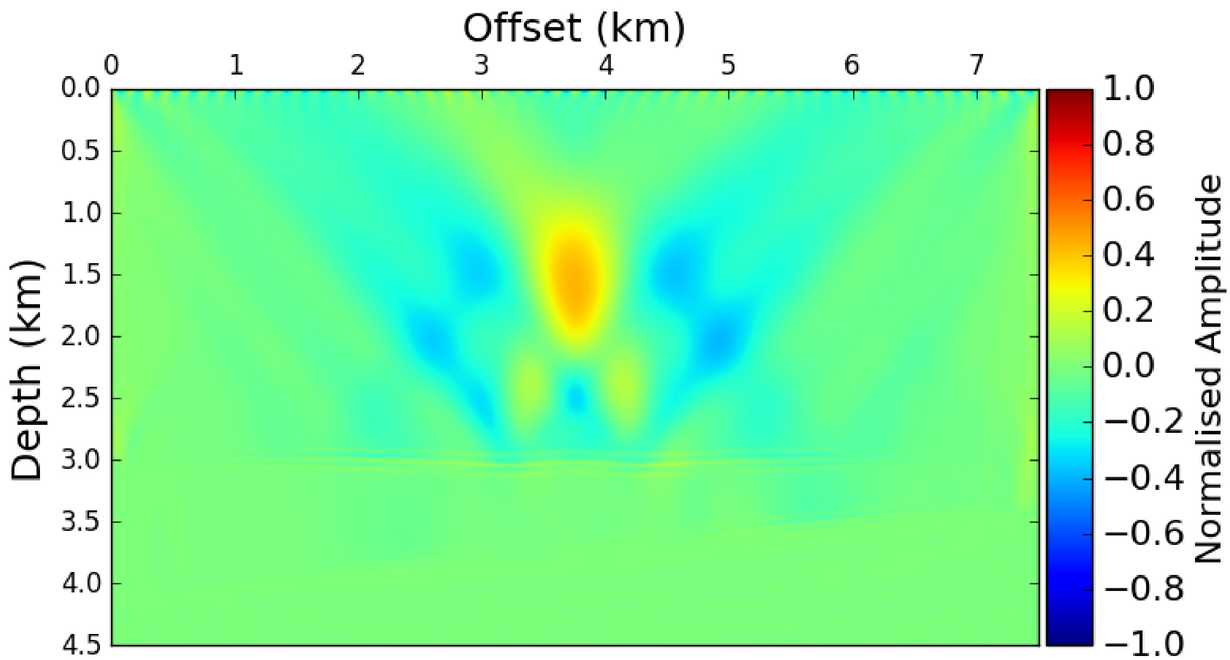

Figure 4.6: RWI gradient without source-receiver illumination - (iteration = 1).

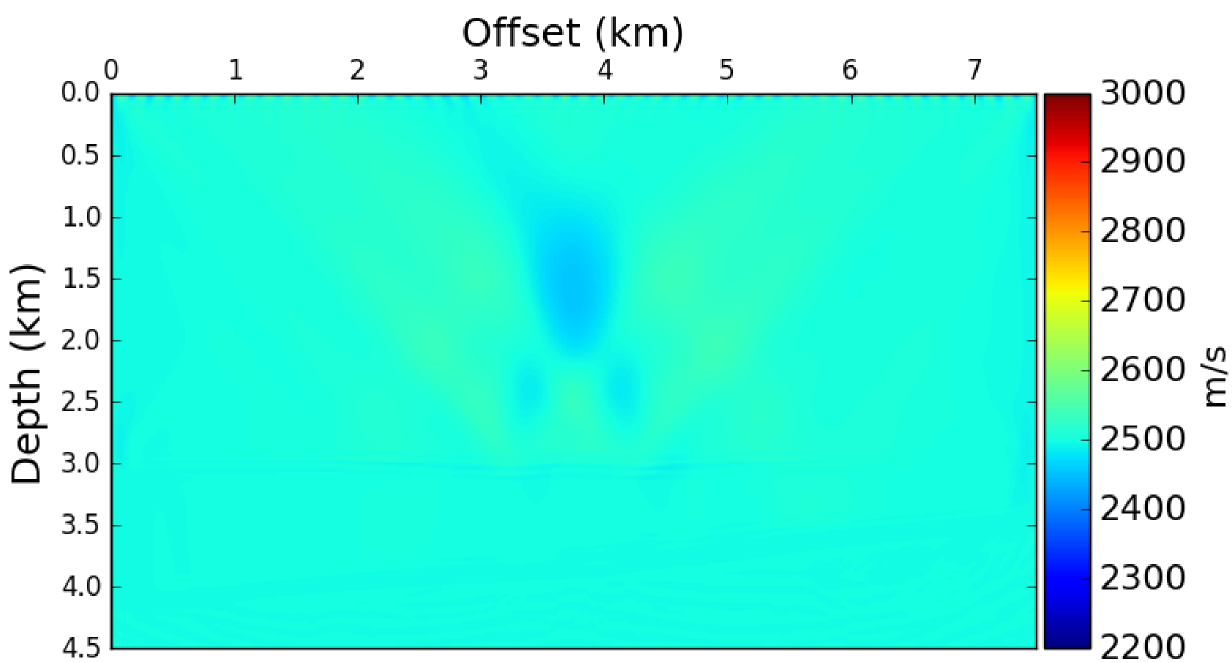

Figure 4.7: Updated velocity model using RWI - (iteration = 1).

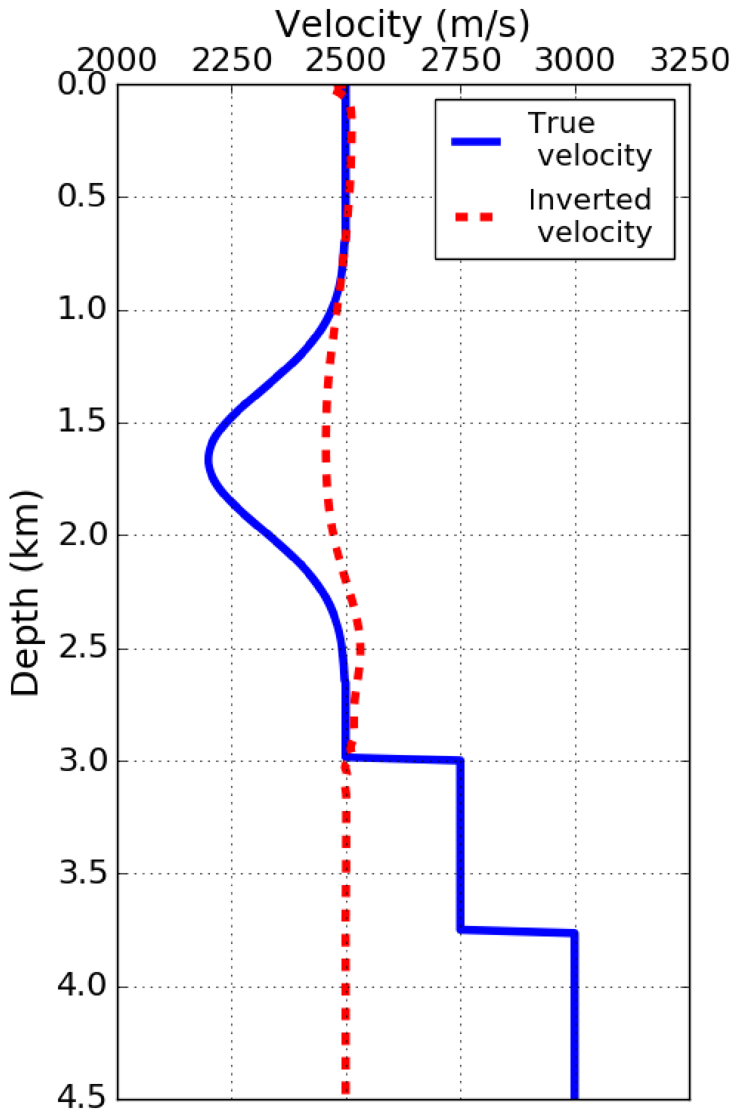

Figure 4.8: Vertical velocity profile at $x = 3750\,m$ for the true and inverted velocity models - (iteration = 1).

The updated velocity, after one iteration, is plotted in Figure (4.7). The Gaussian anomaly starts to form in the inverted velocity at the correct location; however, the boundary of the lens is not entirely resolved. Since RWI aims at recovering the background part of the velocity model, fully resolving that boundary is not expected, nonetheless, according to equation (3.21), we anticipate to see a contribution from the high-frequency part of the velocity model towards the model update. In Figure (4.8) a vertical velocity profile across the center of the model, at $x = 3750\,m$, is plotted for both the true and the inverted velocity models.

In Figure (4.9) the RTM result produced using the inverted velocity is plotted. The horizons are well-focused and more coherent than from the RTM image migrated using the initial velocity (Figure 4.5), and the false structures start to diminish.

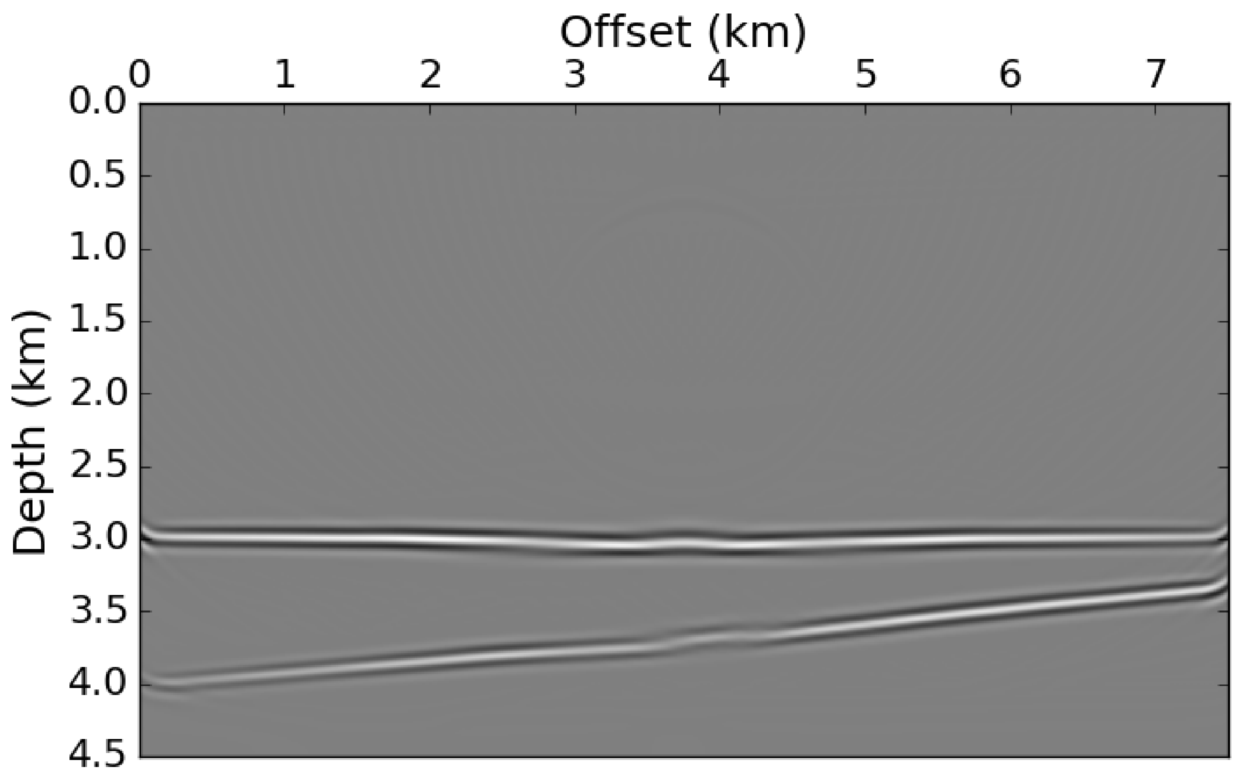

Figure 4.9: RTM image migrated using the inverted velocity - (iteration = 1).

The fifth iteration gradient is plotted in Figure (4.10). In contrast to the gradient of the first iteration (Figure 4.6), update information below the first interface becomes visible, and the second reflector starts to emerge. However, the gradient is creating a false structure. As stated in Section (2.8), predicted data does not contain any AVO information, due to the nature of modeling by seismic demigration. As a consequence, the false structure is most likely caused by our attempt to minimize the misfit between "real" data with AVO information, and predicted data without AVO information, even though a simple model is being used. This issue will be further discussed in Chapter (6).

In Figure (4.11) the inverted velocity after five iterations is plotted. The Gaussian lens is more defined in this model; however, there is an increase in the velocity around the anomaly, due to the acquisition geometry and the amplitude mismatch. When the wavepath of a source-receiver pair does not span the lens, that wavepath will contribute to the gradient with a negative sign; hence, it will update the velocity in the positive direction. In Figure (4.12) a vertical velocity profile across the center of the model, at $x = 3750\,m$, is plotted for both the true and the inverted velocity models. There is a general increase in the velocity in the first layer, except at the anomaly. Also, there is a slight increase in the velocity of the second layer. The convergence rate of the inversion process is plotted in Figure (4.14). After the second iteration, the inversion converged to a final solution.

The migrated image using this inverted velocity (Figure 4.11) is plotted in Figure (4.13). Although horizons are more coherent and well-focused, compared to results from before, major false structures are created with this velocity.

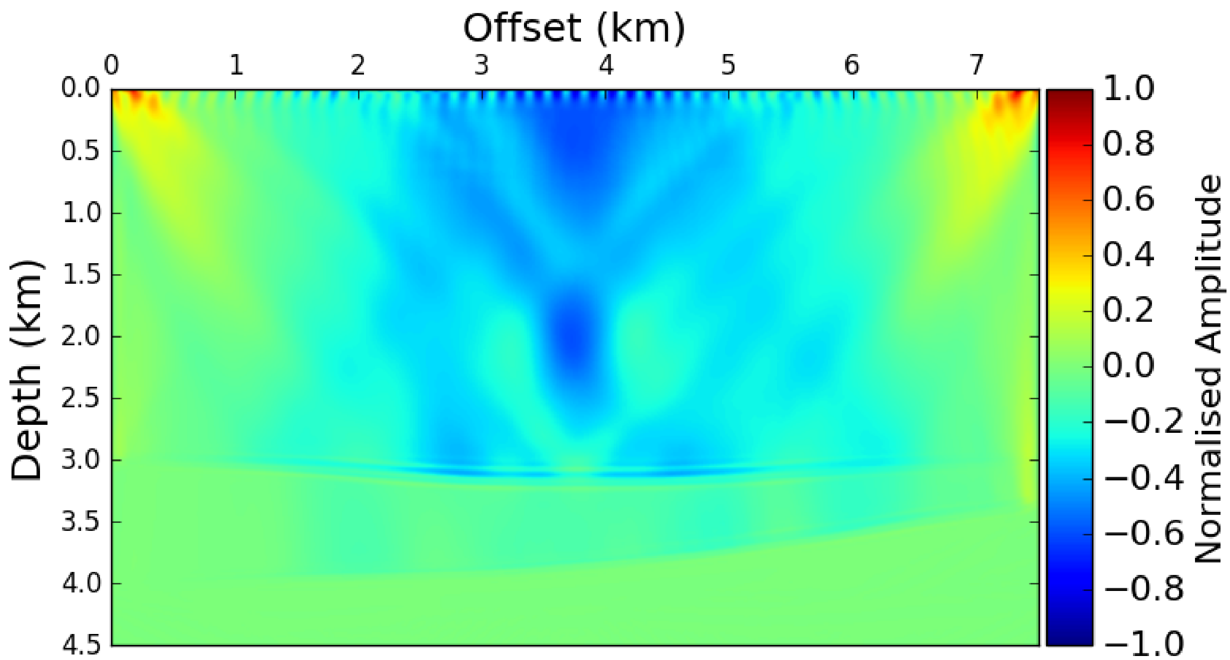

Figure 4.10: RWI gradient without source-receiver illumination - (iteration = 5).

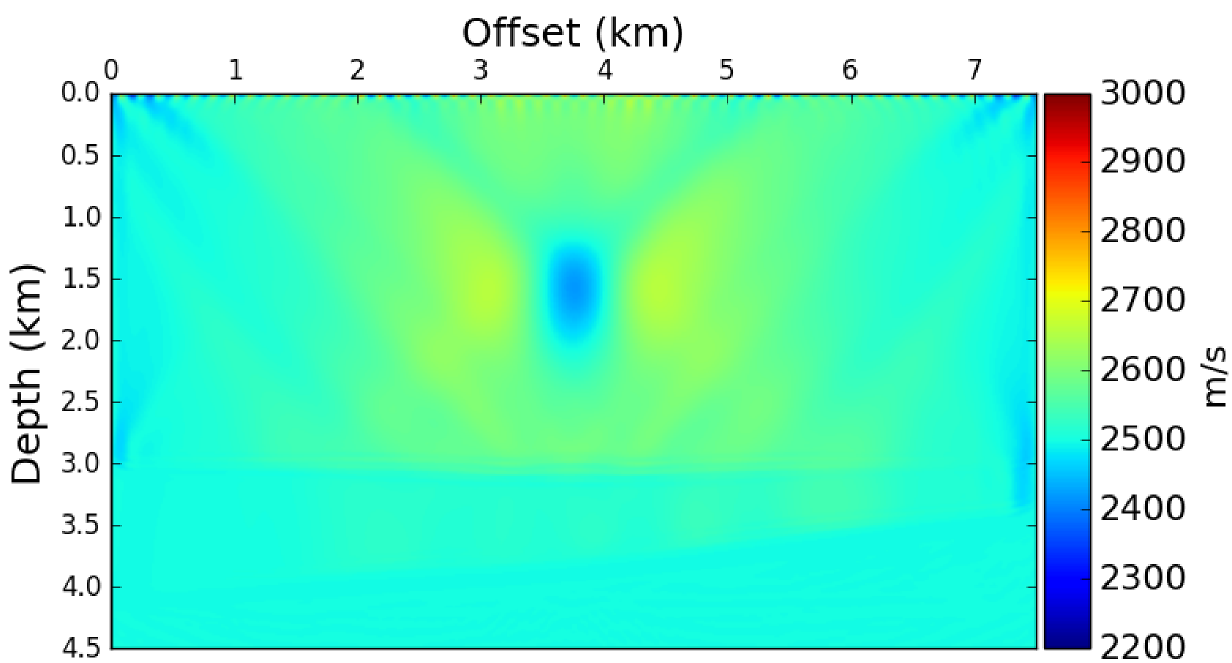

Figure 4.11: Updated velocity model using RWI - (iteration = 5).

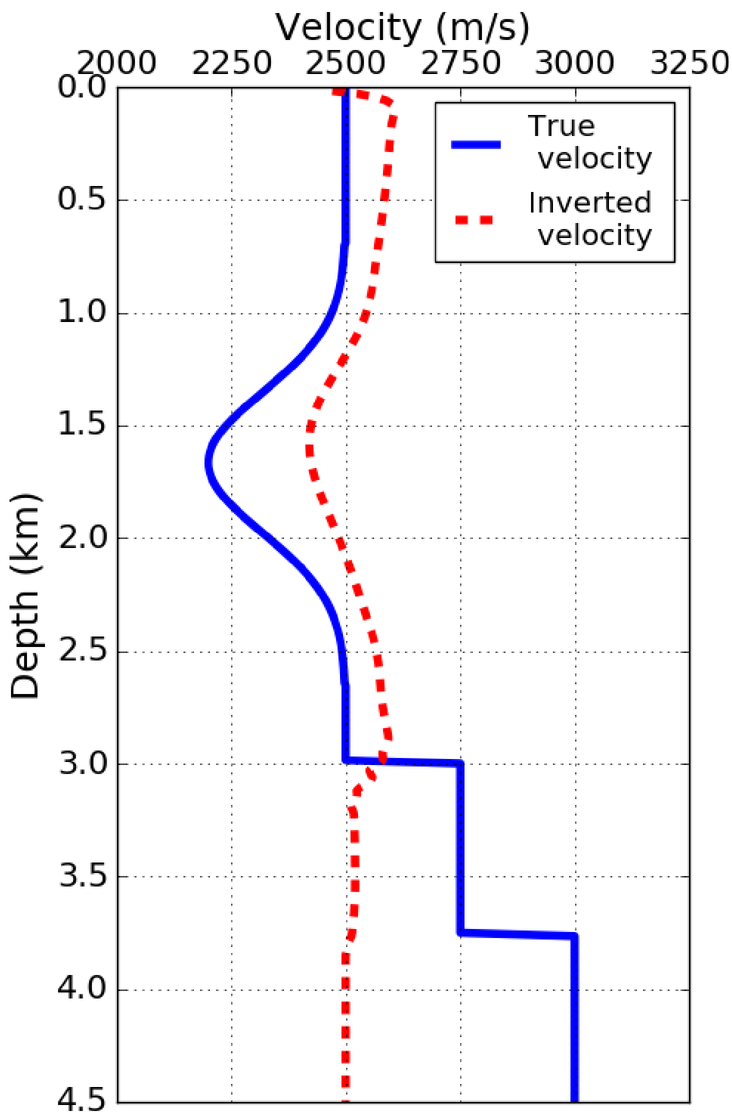

Figure 4.12: Vertical velocity profile at $x = 3750\,m$ for the true and inverted velocity models - (iteration = 5).

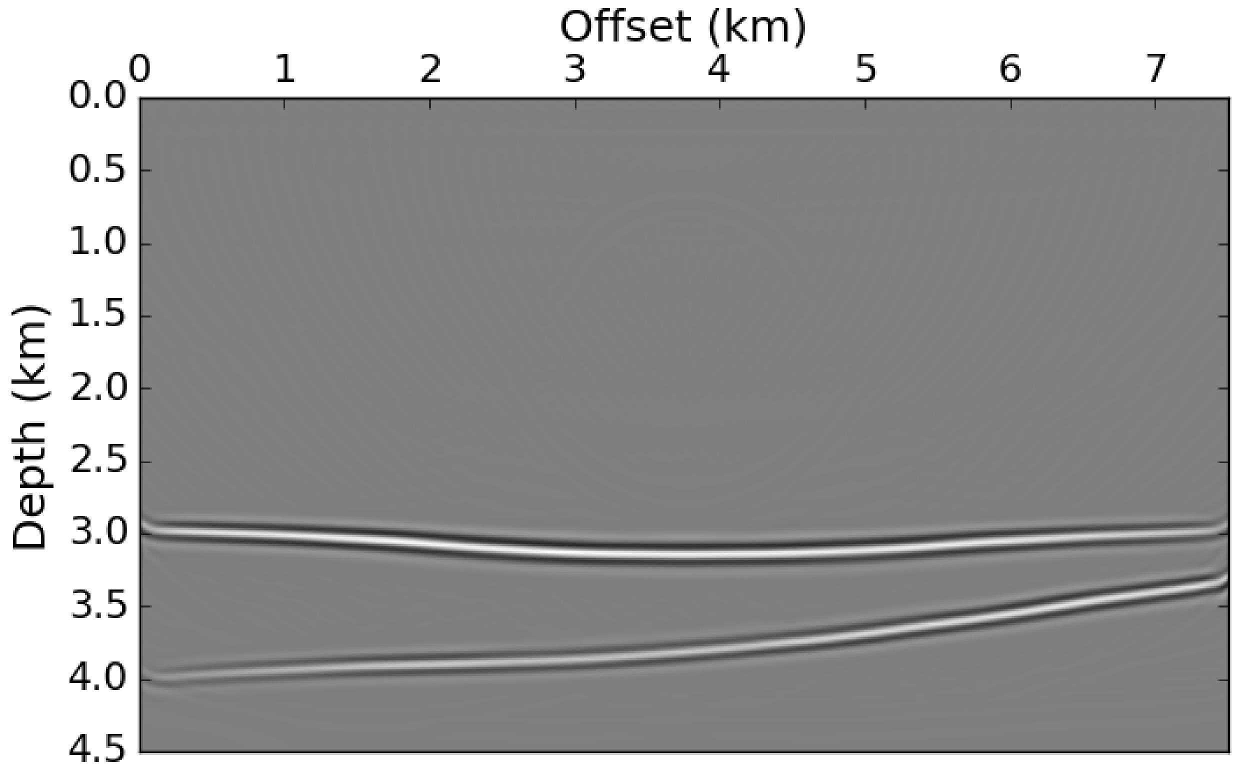

Figure 4.13: RTM image migrated using the inverted velocity - (iteration = 5).

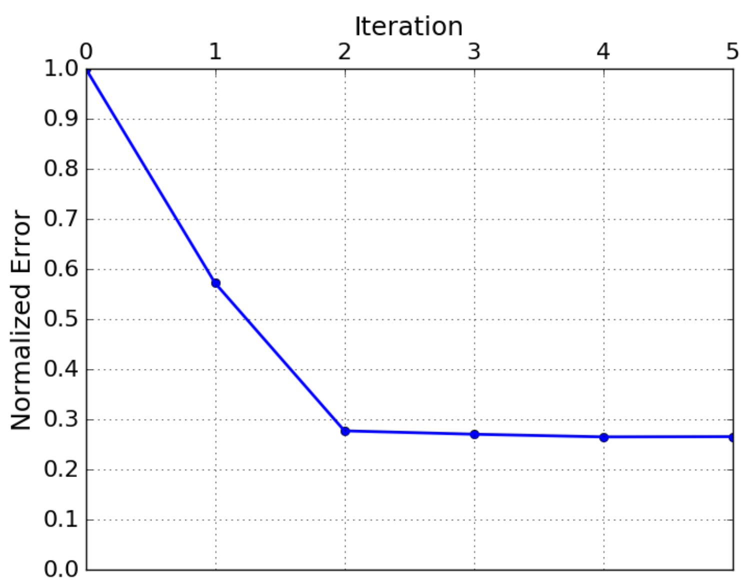

Figure 4.14: Normalized objective function per iteration.

4.3.3 With source-receiver illumination compensation

In this section, I examine the RWI results when applying source-receiver illumination compensation to the gradient. The conventional RWI gradient, used in the previous section, is given

$$g(\mathbf{r}) = \sum_{\mathbf{r}_s,\mathbf{r}_g} \left[\delta\ddot{G}(\mathbf{r},t;\mathbf{r}_s) \otimes G(\mathbf{r},-t;\mathbf{r}_g) + \ddot{G}(\mathbf{r},t;\mathbf{r}_s) \otimes \delta G(\mathbf{r},-t;\mathbf{r}_g)\right], \tag{4.5}$$

while the new gradient, with source-receiver illumination compensation, is given by

$$\begin{aligned} g(\mathbf{r}) = \Bigg[& \frac{\sum_{\mathbf{r}_s,\mathbf{r}_g}\left(\delta\ddot{G}(\mathbf{r},t;\mathbf{r}_s) \otimes G(\mathbf{r},-t;\mathbf{r}_g)\right)}{\left(\sum_{\mathbf{r}_s}\delta\ddot{G}(\mathbf{r},t;\mathbf{r}_s)^2\right)\left(\sum_{\mathbf{r}_g}G(\mathbf{r},-t;\mathbf{r}_g)^2\right)} + \\ & \frac{\sum_{\mathbf{r}_s,\mathbf{r}_g}\left(\ddot{G}(\mathbf{r},t;\mathbf{r}_s) \otimes \delta G(\mathbf{r},-t;\mathbf{r}_g)\right)}{\left(\sum_{\mathbf{r}_s}\ddot{G}(\mathbf{r},t;\mathbf{r}_s)^2\right)\left(\sum_{\mathbf{r}_g}\delta G(\mathbf{r},-t;\mathbf{r}_g)^2\right)}\Bigg]. \end{aligned} \tag{4.6}$$

The gradient of the first iteration is plotted in Figure (4.15). Applying source- receiver illumination improves the resolution of the gradient and enhances the contribution from the deeper parts of the model, otherwise masked by the shallow reflector. Also, the illumination improves the contribution from the high-frequency components and suppresses artifacts caused by the imaging condition. However, the illumination introduces artifacts at the sides of the model.

The updated velocity and the vertical velocity profile, at $x = 3750\,m$, after the first iteration, are plotted in Figures (4.16) and (4.17), respectively. Unlike the results from the previous section, the interfaces between the layers are more visible, and the velocity of the Gaussian anomaly is more accurately inverted. There is an increase in the velocity immediately below the lens, and there is a slight increase in the velocity of the second layer.

The RTM migrated image using the inverted velocity is plotted in Figure (4.17). This image, compared to the RTM migrated image using the first iteration velocity from the previous section (Figure 4.9), is more focused and the false structures completely diminished. This is especially evident for the second reflector.

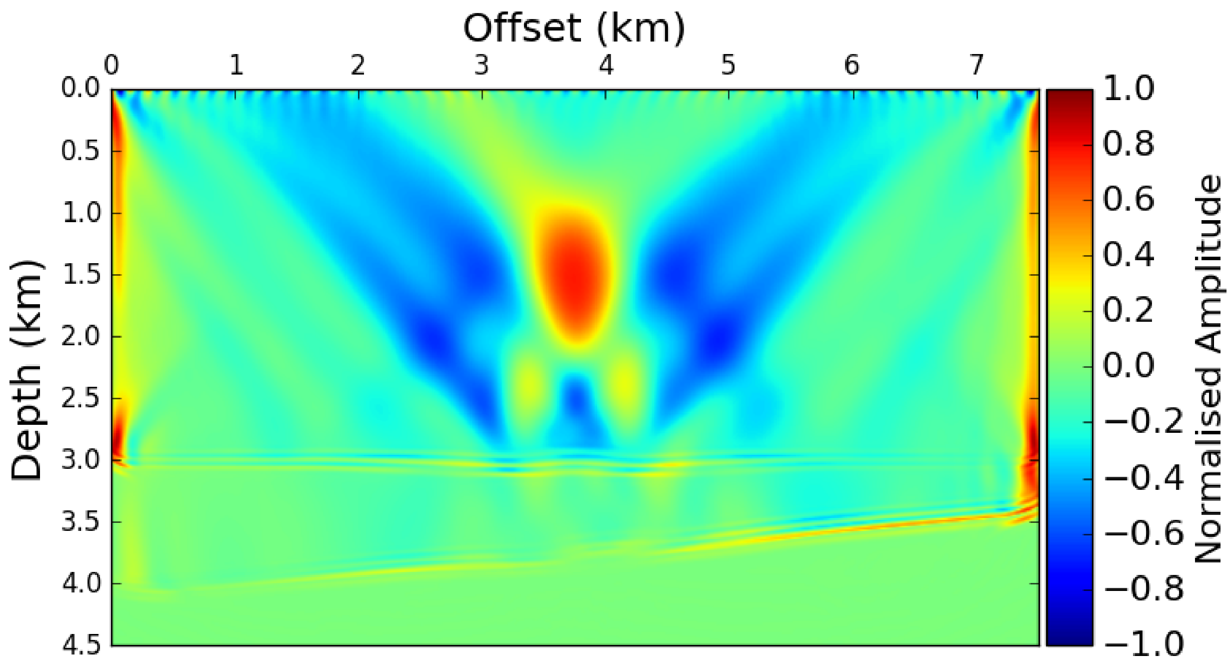

Figure 4.15: RWI gradient with source-receiver illumination - (iteration = 1).

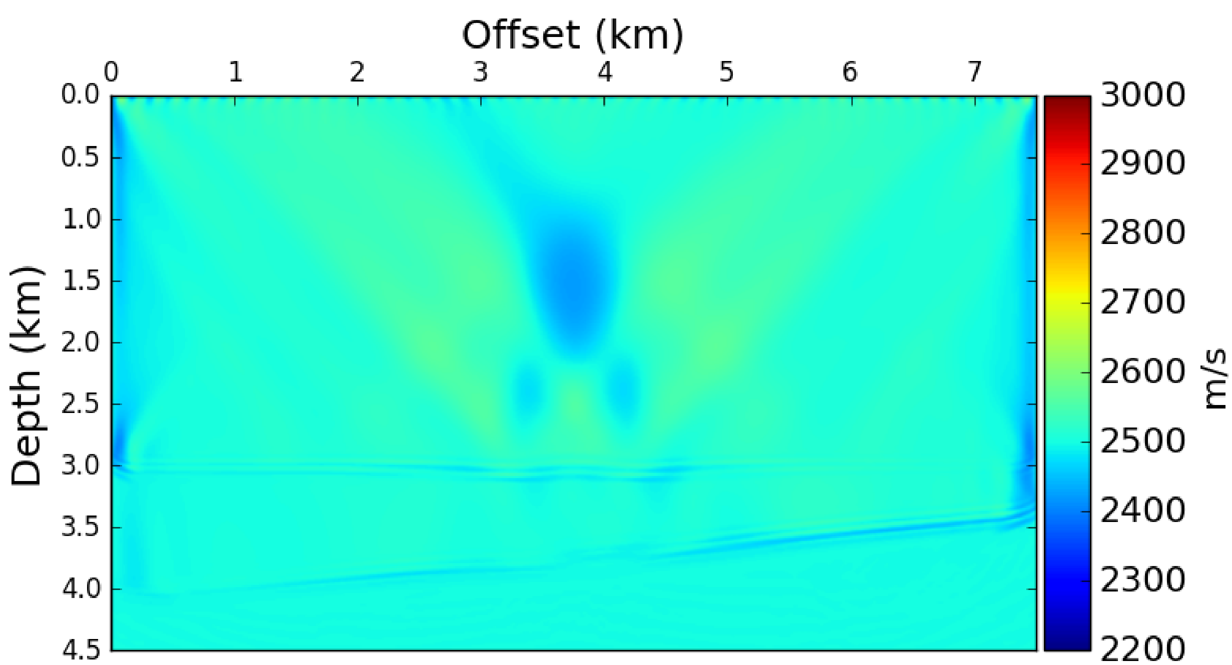

Figure 4.16: Updated velocity model using RWI - (iteration = 1).

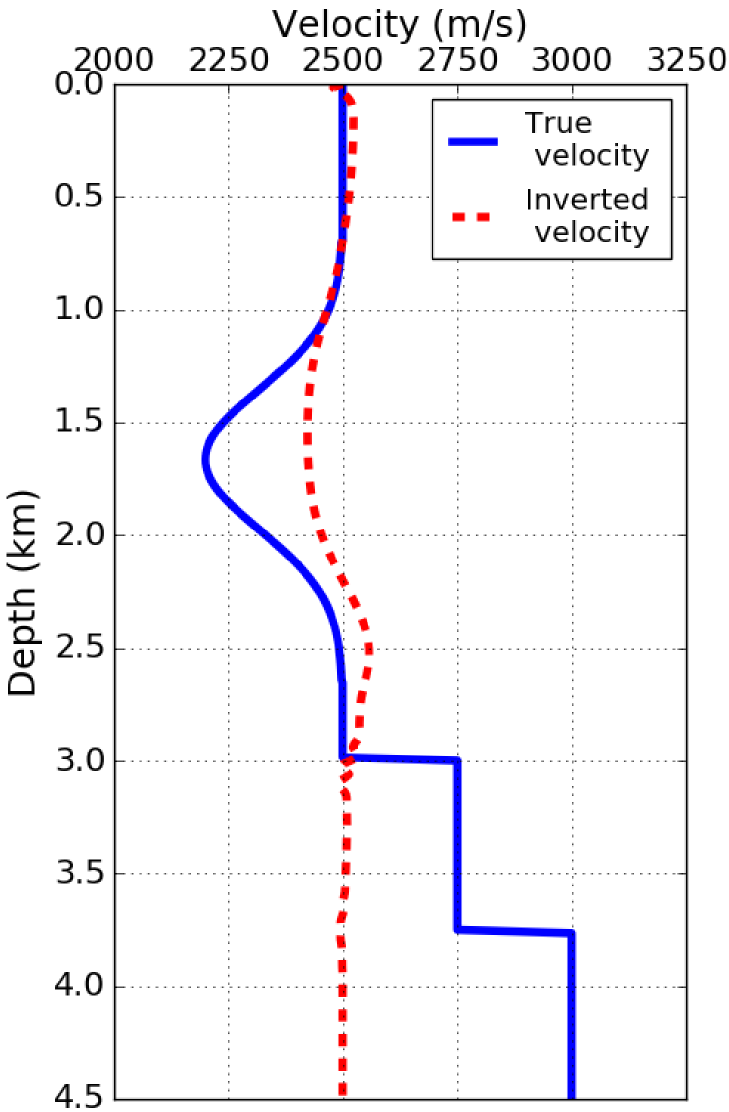

Figure 4.17: Vertical velocity profile at $x = 3750\,m$ for the true and inverted velocity models - (iteration = 1).

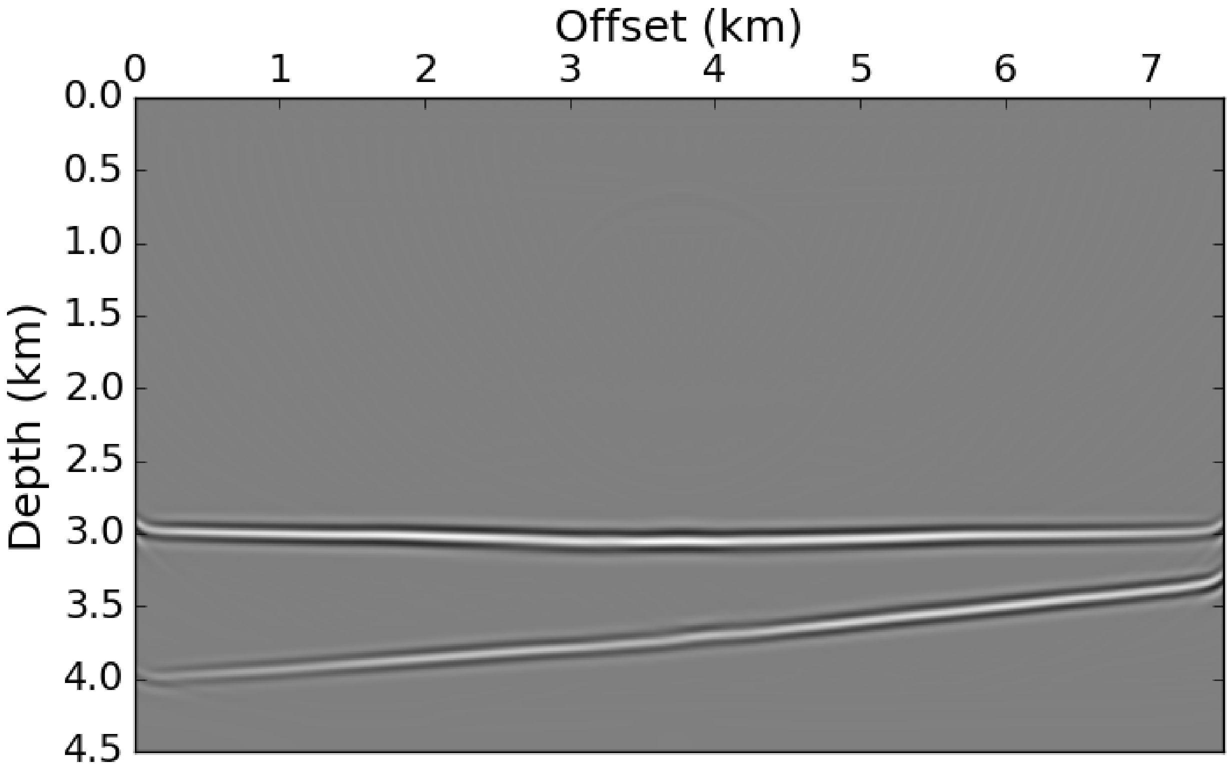

Figure 4.18: RTM image migrated using the inverted velocity - (iteration = 1).

In Figure (4.19) the gradient computed as a part of the fifth iteration is plotted. The magnitude of the update is relatively small. However, there are strong artifacts at the upper corners and the sides of the model. This is caused by limited offsets in the acquisition geometry. The second interface is more defined than the first interface, which indicates that there is more update information included from the second reflector when using source-receiver illumination compensation. The updated velocity model associated with this gradient is plotted in Figure (4.20). There is an increase in the velocity in the inverted model for both the first and second layers, including the Gaussian anomaly. This is easier visualized in the velocity profile (Figure 4.21), where I observe that the lens is better inverted after the first iteration.

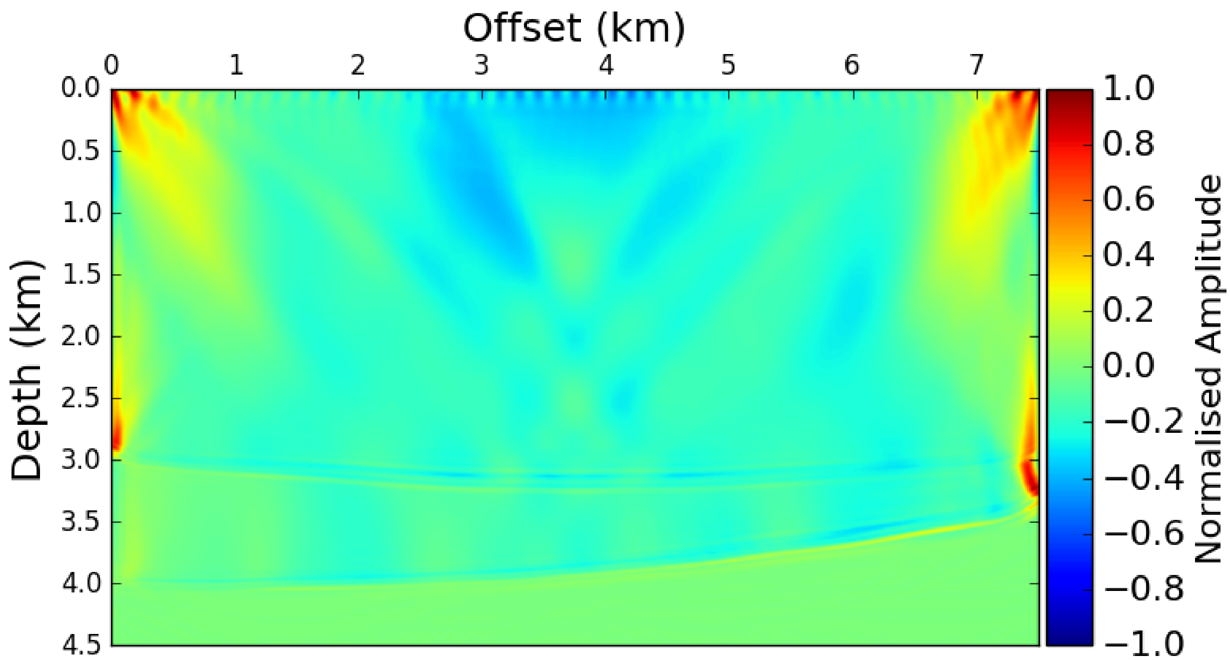

Figure 4.19: RWI gradient with source-receiver illumination - (iteration = 5).

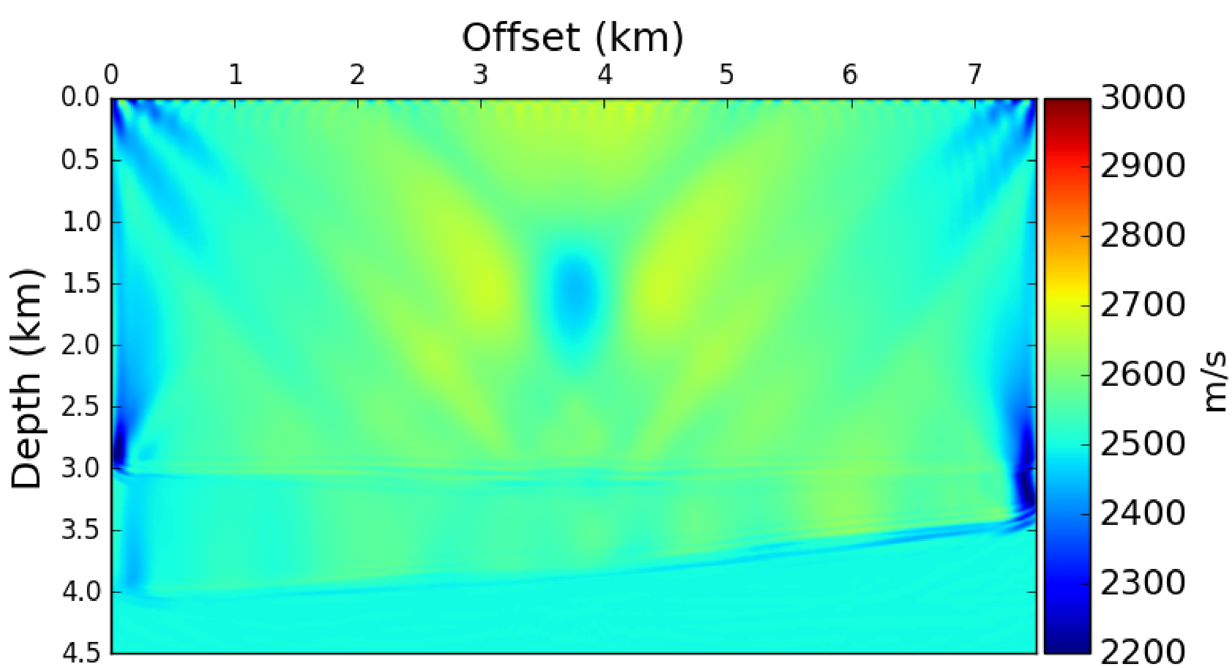

Figure 4.20: Updated velocity model using RWI - (iteration = 5).

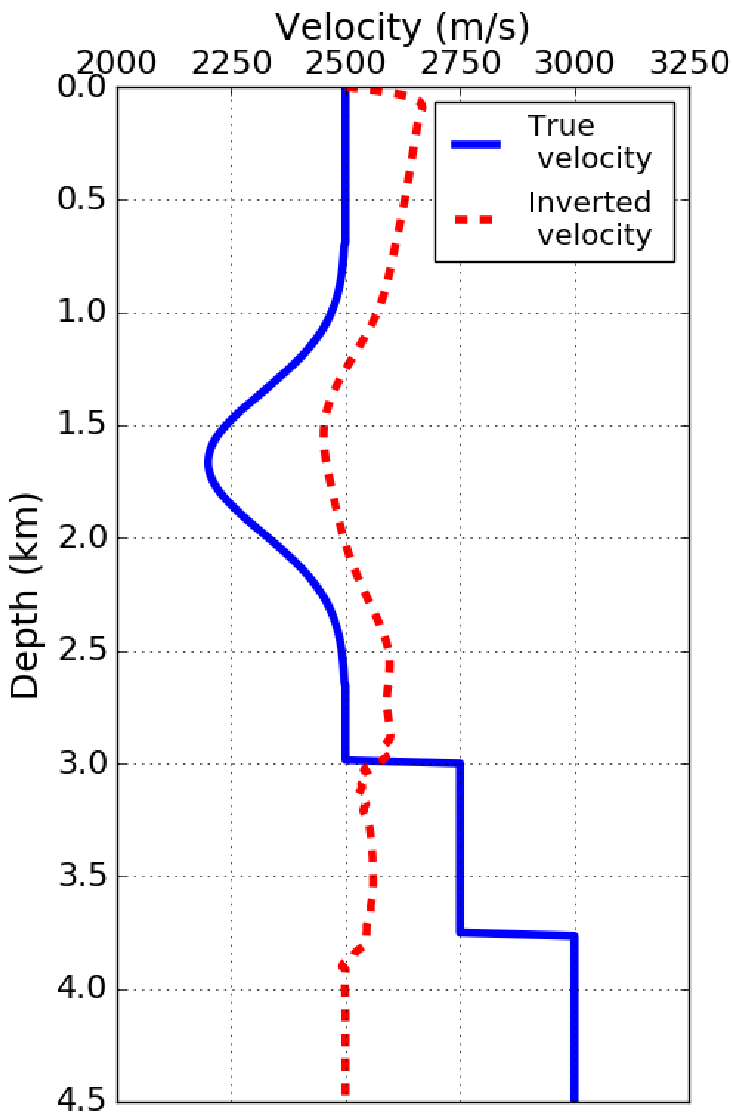

Figure 4.21: Vertical velocity profile at $x = 3750\,m$ for the true and inverted velocity models - (iteration = 5).

In Figure (4.22) the migrated image using the fifth iteration inverted velocity is plotted. Again, later iterations produce images with more coherent and well-focused horizons, but also introduce false structures, due to the velocity increase in the first layer. The curvature of the structure is larger, I observe, when source-receiver illumination is applied. From the misfit error per iteration plot (Figure 4.23), I conclude that the illumination compensation speeds up convergence.

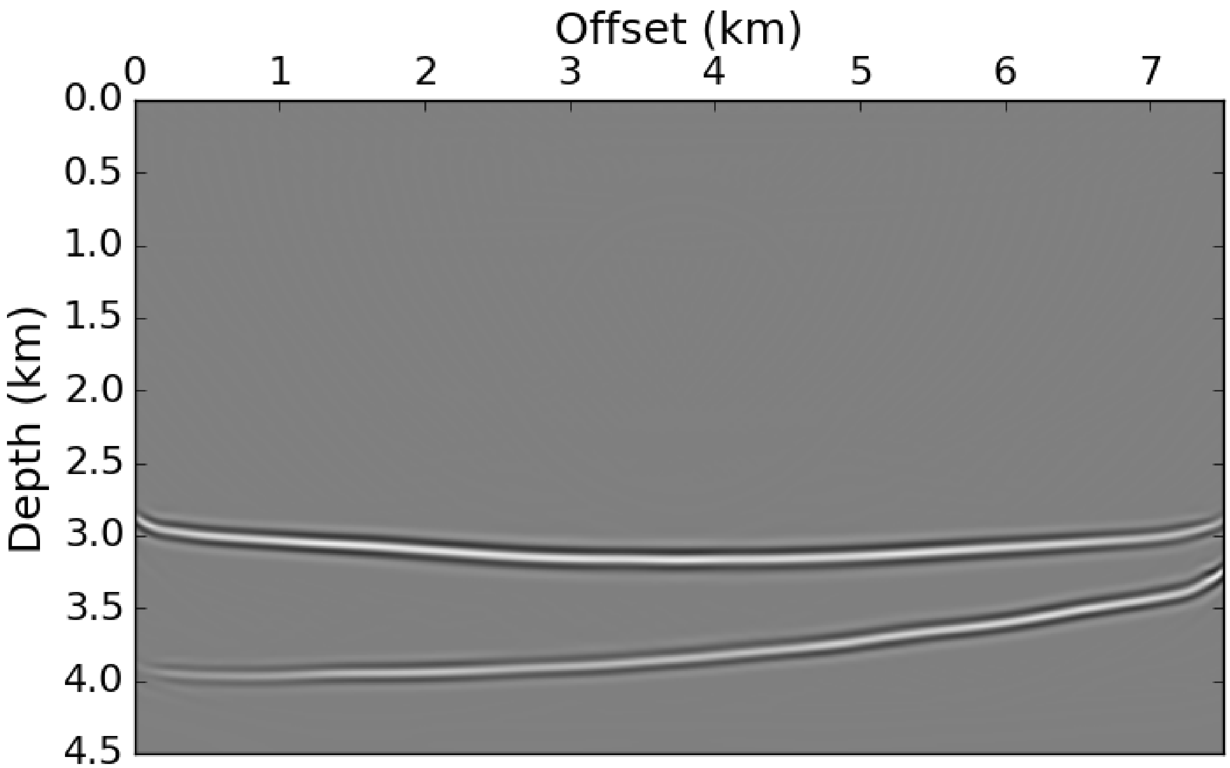

Figure 4.22: RTM image migrated using the inverted velocity - (iteration = 5).

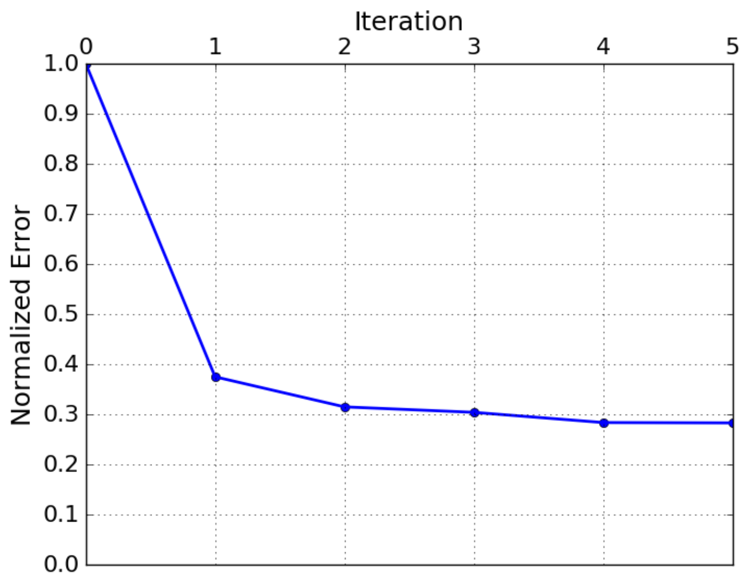

Figure 4.23: Normalized objective function per iteration.

4.3.4 FWI results

To demonstrate the superiority of RWI over FWI, in the particular task of recovering the smoothly-varying component of the background velocity, I examine the FWI results. For meaningful comparisons, I plot the final FWI results (iteration = 5), having also applied source-receiver illumination to the gradient. In Figure (4.24) the gradient for the fifth iteration is plotted. From the gradient, I observe that the reflectivity part of the velocity model is highly resolved, however, the gradient lacks any notable contributions towards updating the background part of the model. As a result, the inverted velocity (Figure 4.25) does not contain any information about the Gaussian anomaly, and false structures are present. The vertical velocity profile (Figure 4.26) indicates that the only difference between the initial and inverted velocity is that the inverted model incorporates high-frequency information.

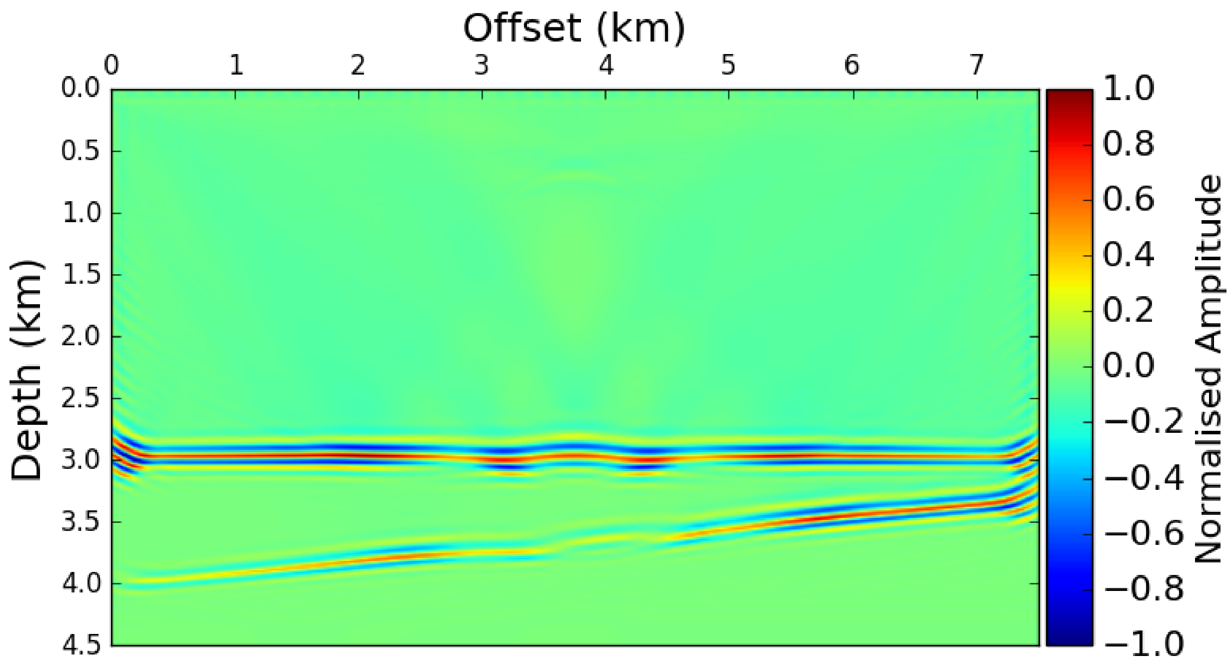

Figure 4.24: FWI gradient with source-receiver illumination - (iteration = 5).

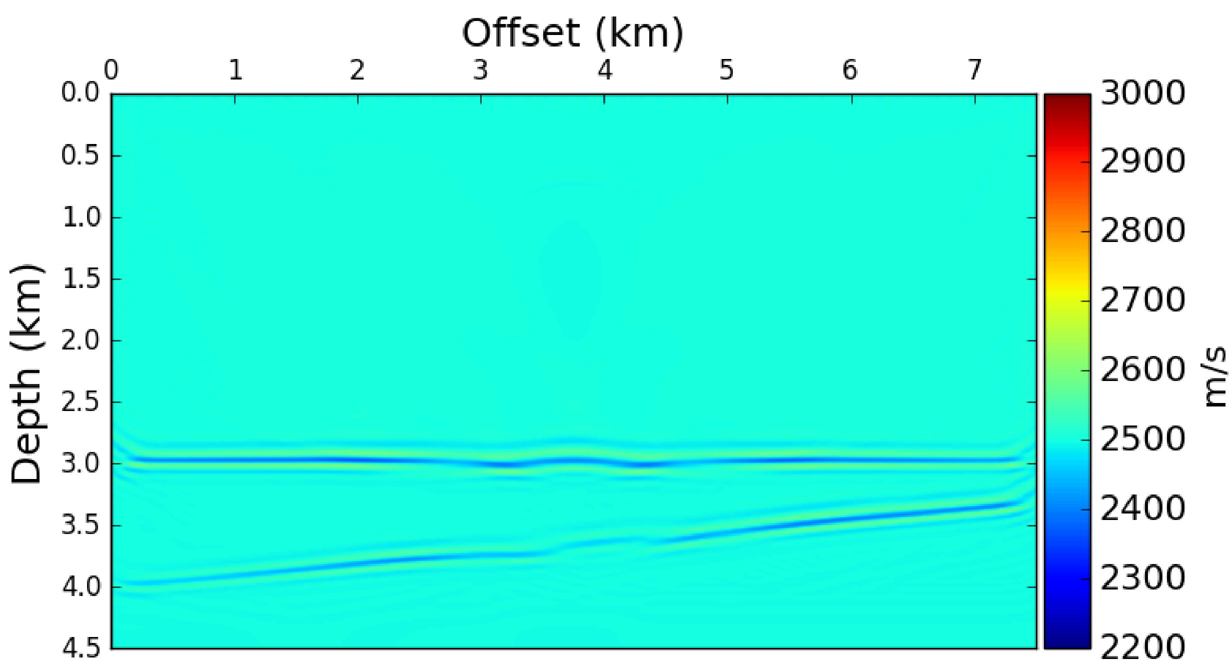

Figure 4.25: Updated velocity model using FWI - (iteration = 5).

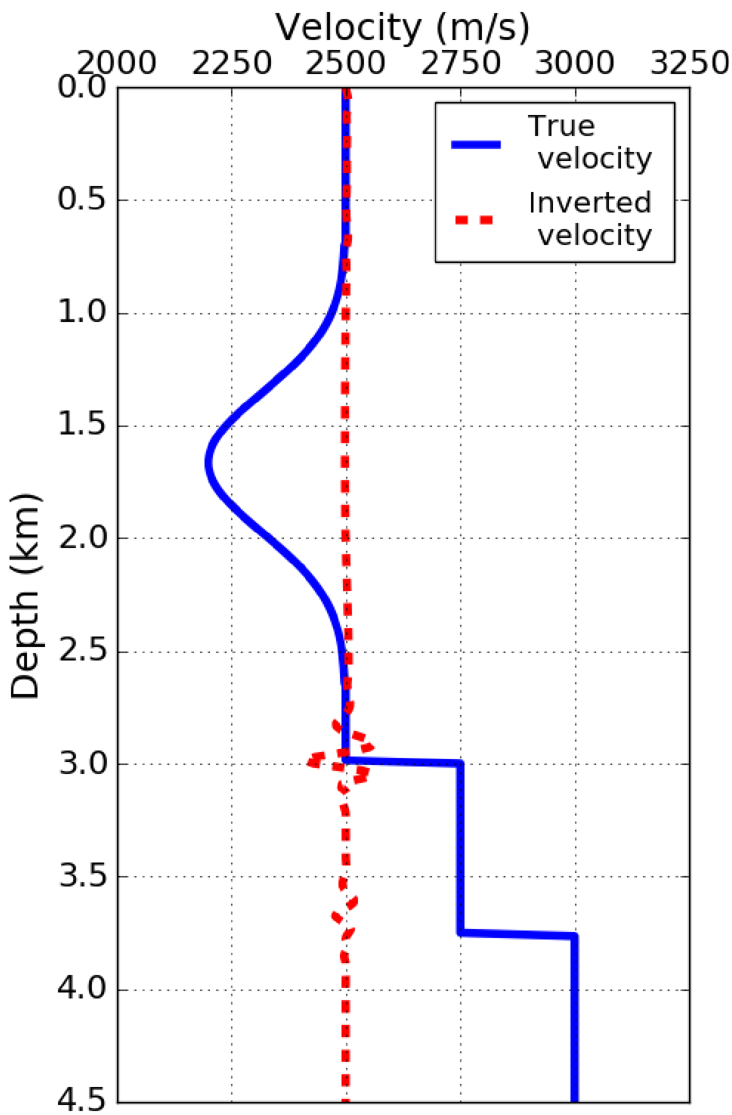

Figure 4.26: Vertical velocity profile at $x = 3750\,m$ for the true and inverted velocity models for FWI - (iteration = 5).

4.3.5 RWI equations analysis

In this section, I present different sets of equations than the one in Section (4.3.1) and the output gradients. Unlike the gradient (Figure 4.15) calculated using the set of equations in Section (4.3.1), the gradients presented in this section updates the Gaussian anomaly incorrectly. Treating the source term in the wave equation as a forcing term or as a boundary value problem (BVP), and using the source in a conventional way or applying an integral to the source function, as proposed by Zhang and Sun (2009), provides different results.

Set of equations A:

The equation used to generate the source wavefield, used in the gradient calculation, is given by

$$\left[\nabla^2 - \mathbf{m}\frac{\partial^2}{\partial t^2}\right] G(\mathbf{r}, t; \mathbf{r}_s) = f(t), \tag{4.7}$$

and the data residuals receiver wavefield, used in the gradient calculation, equation is

$$\begin{cases} \left[\nabla^2 - \mathbf{m}\frac{\partial^2}{\partial t^2}\right] G(\mathbf{r}, t; \mathbf{r}_g) = 0 \\ G(\mathbf{r}_s, t; \mathbf{r}_g) = \delta P(\mathbf{r}_g, t; \mathbf{r}_s). \end{cases} \tag{4.8}$$

The source wavefield equation used to produce the RTM image is

$$\begin{cases} \left[\nabla^2 - \mathbf{m}\frac{\partial^2}{\partial t^2}\right] G(\mathbf{r}, t; \mathbf{r}_s) = 0 \\ G(\mathbf{r}, t; \mathbf{r}_s) = \int_0^t dt' f(t'), \end{cases} \tag{4.9}$$

and the equation used to calculate receiver wavefield needed for the RTM is

$$\begin{cases} \left[\nabla^2 - \mathbf{m}\frac{\partial^2}{\partial t^2}\right] G(\mathbf{r}, t; \mathbf{r}_g) = 0 \\ G(\mathbf{r}_s, t; \mathbf{r}_g) = G(\mathbf{r}_g, t; \mathbf{r}_s). \end{cases} \tag{4.10}$$

In Figure (4.27), the gradient calculated using set of equations A is plotted.

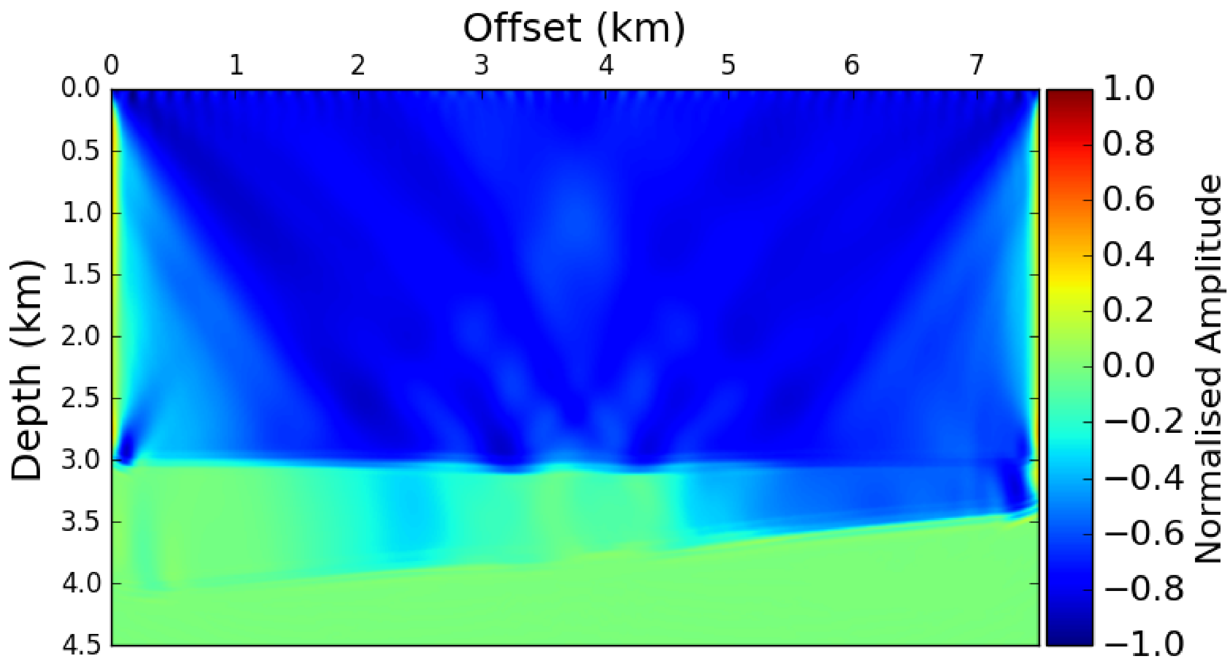

Figure 4.27: Gradient calculated using set of equations A.

Set of equations B:

This set of equations is to be used intuitively, as the receiver wavefield in RTM and the data residuals receiver wavefield are treated as a boundary value problem. The equation used to generate the source wavefield, used in the gradient calculation, is given by

$$\left[\nabla^2 - \mathbf{m}\frac{\partial^2}{\partial t^2}\right] G(\mathbf{r}, t; \mathbf{r}_s) = f(t), \tag{4.11}$$

and the equation to calculate the data residuals receiver wavefield, needed in the gradient calculation, is

$$\begin{cases} \left[\nabla^2 - \mathbf{m}\frac{\partial^2}{\partial t^2}\right] G(\mathbf{r}, t; \mathbf{r}_g) = 0 \\ G(\mathbf{r}_s, t; \mathbf{r}_g) = \delta P(\mathbf{r}_g, t; \mathbf{r}_s). \end{cases} \tag{4.12}$$

The source wavefield equation used to produce the RTM image is

$$\left[\nabla^2 - \mathbf{m}\frac{\partial^2}{\partial t^2}\right] G(\mathbf{r}, t; \mathbf{r}_s) = f(t), \tag{4.13}$$

and the equation used to calculate receiver wavefield needed for the RTM is

$$\begin{cases} \left[\nabla^2 - \mathbf{m}\frac{\partial^2}{\partial t^2}\right] G(\mathbf{r}, t; \mathbf{r}_g) = 0 \\ G(\mathbf{r}_s, t; \mathbf{r}_g) = G(\mathbf{r}_g, t; \mathbf{r}_s). \end{cases} \tag{4.14}$$

In Figure (4.28), the gradient calculated using set of equations B is plotted.

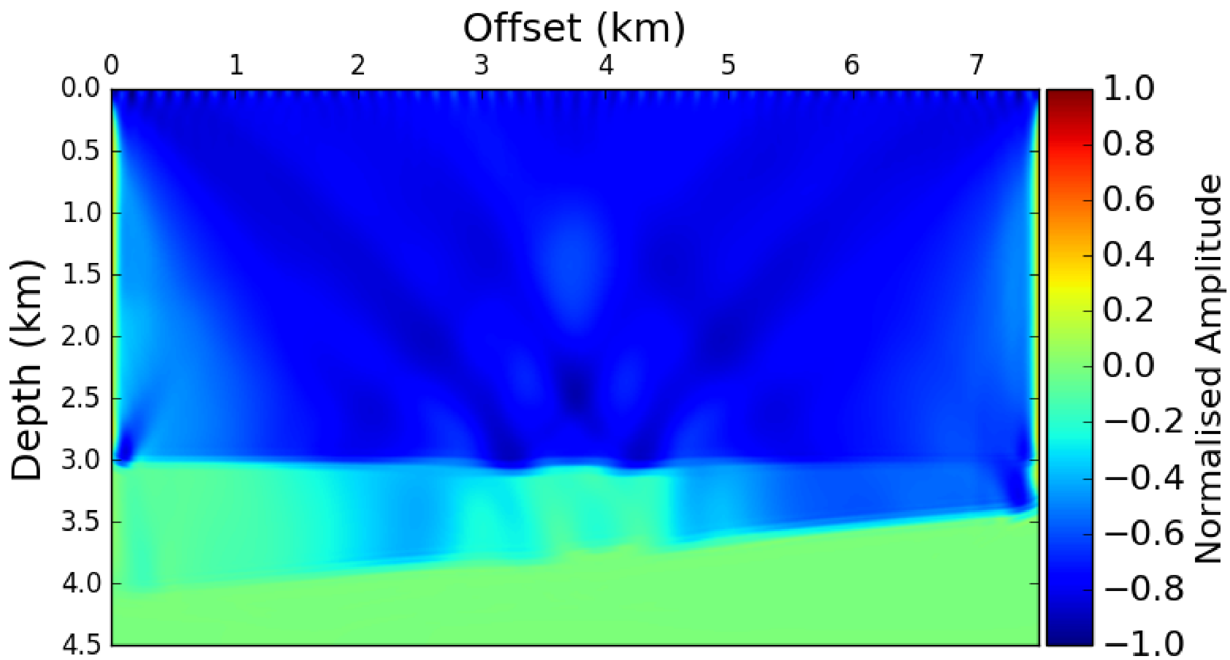

Figure 4.28: Gradient calculated using set of equations B.

Set of equations C:

The equation used to generate the source wavefield, used in the gradient calculation, is given by

$$\left[\nabla^2 - \mathbf{m}\frac{\partial^2}{\partial t^2}\right] G(\mathbf{r}, t; \mathbf{r}_s) = f(t), \tag{4.15}$$

and the data residuals receiver wavefield equation used in the gradient calculation is

$$\left[\nabla^2 - \mathbf{m}\frac{\partial^2}{\partial t^2}\right] G(\mathbf{r}, t; \mathbf{r}_g) = \delta P(\mathbf{r}_g, t; \mathbf{r}_s). \tag{4.16}$$

The source wavefield equation used to produce the RTM image is

$$\left[\nabla^2 - \mathbf{m}\frac{\partial^2}{\partial t^2}\right] G(\mathbf{r}, t; \mathbf{r}_s) = f(t), \tag{4.17}$$

and the equation used to calculate receiver wavefield needed for the RTM is

$$\begin{cases} \left[\triangledown^2 - \mathbf{m}\frac{\partial^2}{\partial t^2}\right] G(\mathbf{r}, t; \mathbf{r}_g) = 0 \\ G(\mathbf{r}_s, t; \mathbf{r}_g) = G(\mathbf{r}_g, t; \mathbf{r}_s). \end{cases} \tag{4.18}$$

In Figure (4.29), the gradient calculated using set of equations C is plotted.

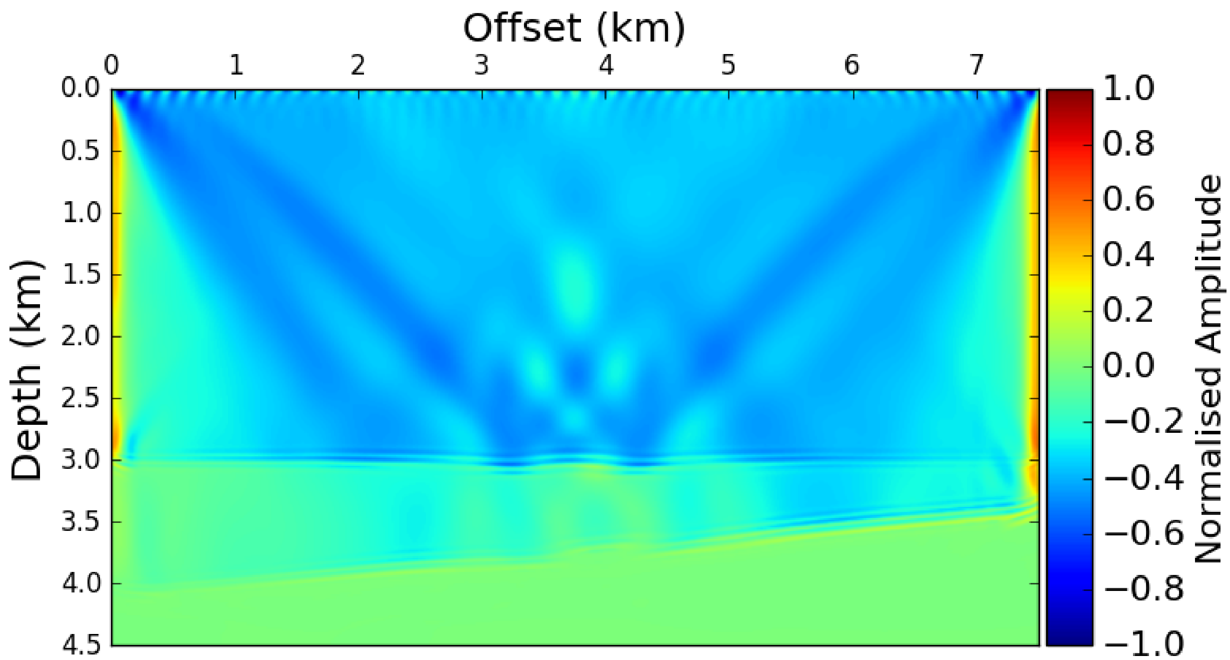

Figure 4.29: Gradient calculated using set of equations C.

Set of equations D:

The equation used to generate the source wavefield used in the gradient calculation is given by

$$\begin{cases} \left[\triangledown^2 - \mathbf{m}\frac{\partial^2}{\partial t^2}\right] G(\mathbf{r}, t; \mathbf{r}_s) = 0 \\ G(\mathbf{r}, t; \mathbf{r}_s) = \int_0^t dt' f(t'), \end{cases} \tag{4.19}$$

and the data residuals receiver wavefield equation used in the gradient calculation is

$$\left[\triangledown^2 - \mathbf{m}\frac{\partial^2}{\partial t^2}\right] G(\mathbf{r}, t; \mathbf{r}_g) = \delta P(\mathbf{r}_g, t; \mathbf{r}_s). \tag{4.20}$$

The source wavefield equation used to produce the RTM image is

$$\begin{cases} \left[\bigtriangledown^2 - \mathbf{m}\frac{\partial^2}{\partial t^2}\right] G(\mathbf{r}, t; \mathbf{r}_s) = 0 \\ G(\mathbf{r}, t; \mathbf{r}_s) = \int_0^t dt' f(t'), \end{cases} \tag{4.21}$$

and the equation used to calculate receiver wavefield needed for the RTM is

$$\begin{cases} \left[\bigtriangledown^2 - \mathbf{m}\frac{\partial^2}{\partial t^2}\right] G(\mathbf{r}, t; \mathbf{r}_g) = 0 \\ G(\mathbf{r}_s, t; \mathbf{r}_g) = G(\mathbf{r}_g, t; \mathbf{r}_s). \end{cases} \tag{4.22}$$

In Figure (4.30), the gradient calculated using set of equations D is plotted.

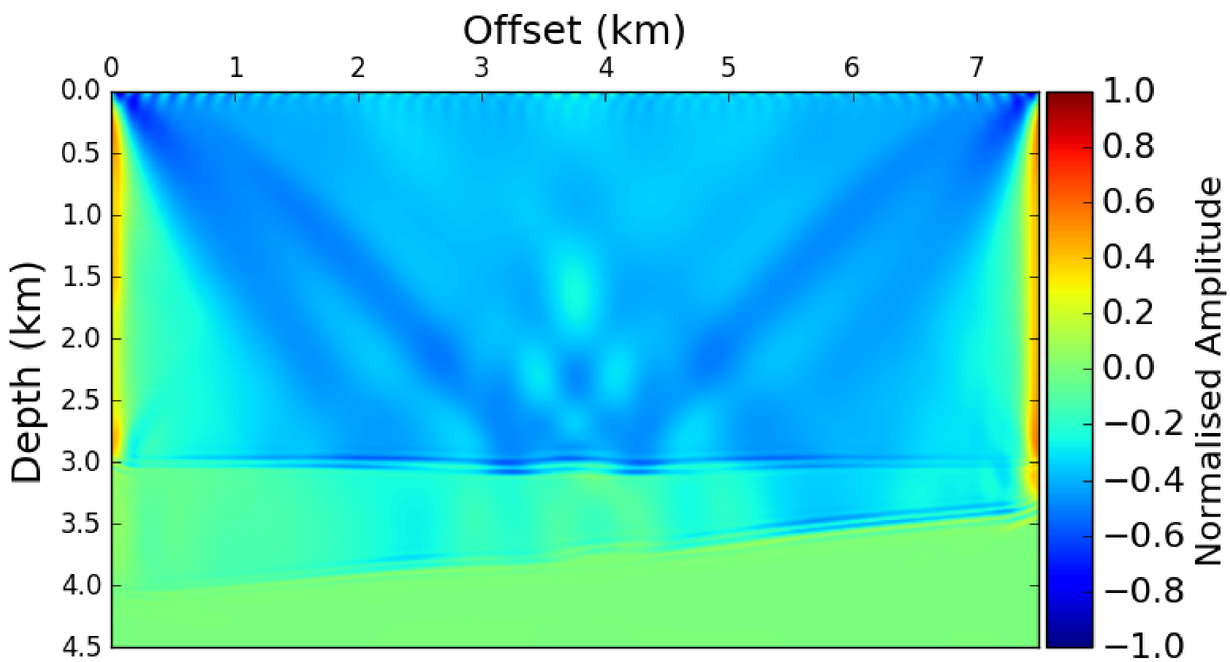

Figure 4.30: Gradient calculated using set of equations D.

4.4 Conclusion

In this chapter, I examined simple RWI results with and without source-receiver illumination applied to the gradient. I observe that applying illumination to the gradient improves the inversion results in the deep section, and it speeds up the convergence rate of the inversion;

however, illumination scales up artifacts as well. I interpret the absence of AVO information in the predicted data as the primary cause, in higher order iterations, of update errors in the velocity. However, a well-focused RTM image is produced in any focused case. In contrast, FWI fails at recovering the background part of the velocity model. I showed that the inversion is highly sensitive to the equations used in the wavefields calculations.

Chapter 5

RWI in complex media

5.1 Introduction

In the previous chapter, I illustrated how RWI has the advantage of recovering the long wavelength components of the velocity model. However, I used a simple model in the examination. In this chapter, I examine the effectiveness of RWI in the case of a complex model. To achieve our goal, I use a part the Marmousi model. The Marmousi model is a complex geological model based on a profile through the North Quenguela Trough in the Cuanza basin in Angola (Versteeg, 1994), that was generated at the Institut Français du Pétrole (IFP).

5.2 Modeling

The complete and partial Marmousi model that I use are plotted in Figures (5.1) and (5.2). The model is $1800\,m \times 800\,m$ in dimension, with many reflectors, faults, and strong velocity variations. The model has a $200\,m$ water layer, with a velocity of $1470\,m/s$. The velocity of the model varies from $1045\,m/s$ to $4401\,m/s$. The initial model I used is a constant-velocity water layer overlaying a linearly increasing velocity from $1045.5\,m/s$ to $3014\,m/s$ (Figure 5.3). In Figure (5.5) a vertical velocity profile across the center of the model, at $x = 900\,m$, is plotted for both the true and the initial velocity models.

For the acquisition, thirty-six shots were used in this experiment, with the first shot at $x = 25\,m$ and the last shot at $x = 1775\,m$, with a shot spacing of $50\,m$. There are 359 receivers with $5\,m$ spacing. The depth of all sources and receivers is $5\,m$. The recording time is $1.5\,s$ with $0.68\,ms$ time interval. The source wavelet is a Ricker wavelet with $20\,Hz$

dominant frequency. Similar to the previous example (Chapter 4), direct arrivals are muted in the observed data. A sample of the observed data at $x = 275\,m$ and $x = 775\,m$ is plotted in Figures (5.4a) and (5.4b). Table (5.1) summarizes the acquisition geometry and the model parameters. In Figure (5.6) the RTM migrated image using the true velocity model is plotted.

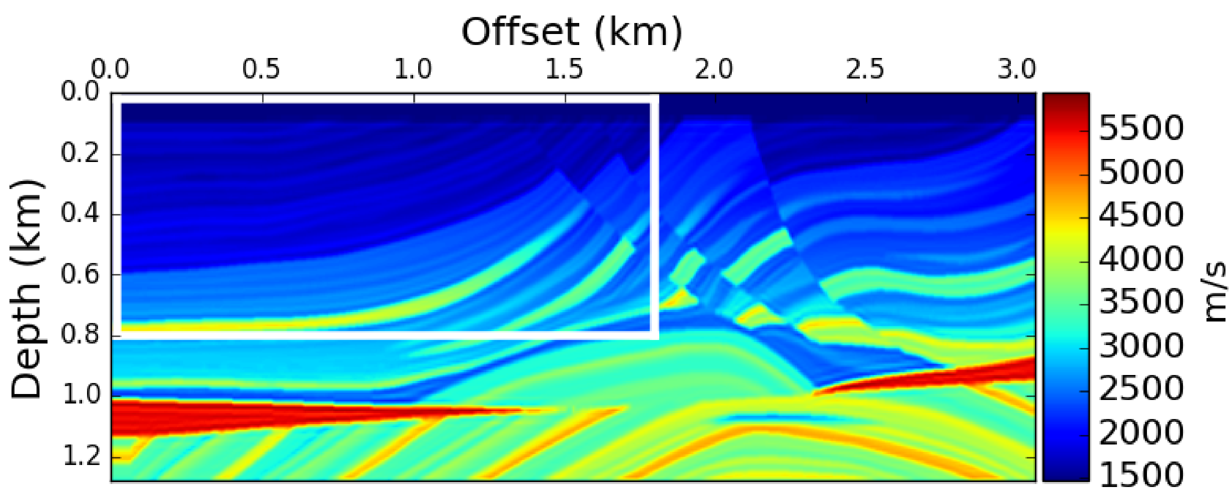

Figure 5.1: Marmousi model (the white box is the testing model).

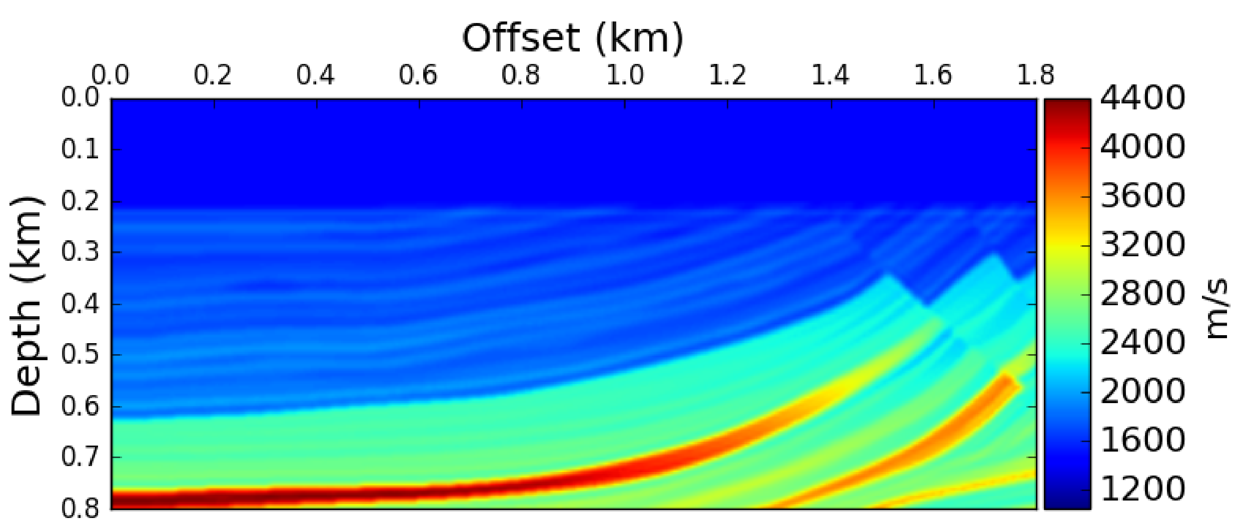

Figure 5.2: True velocity model.

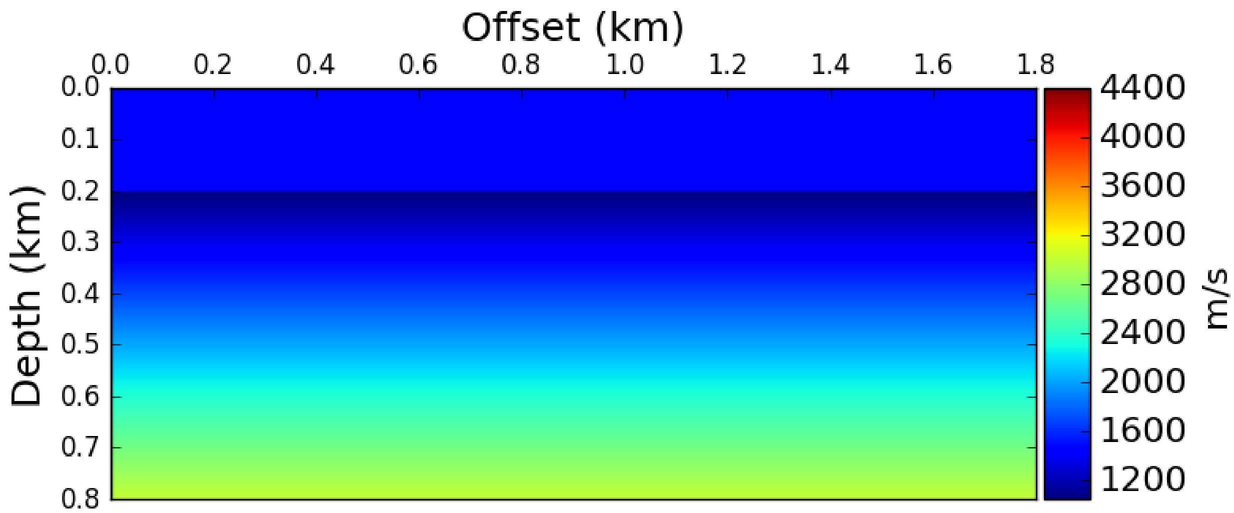

Figure 5.3: Initial velocity model.

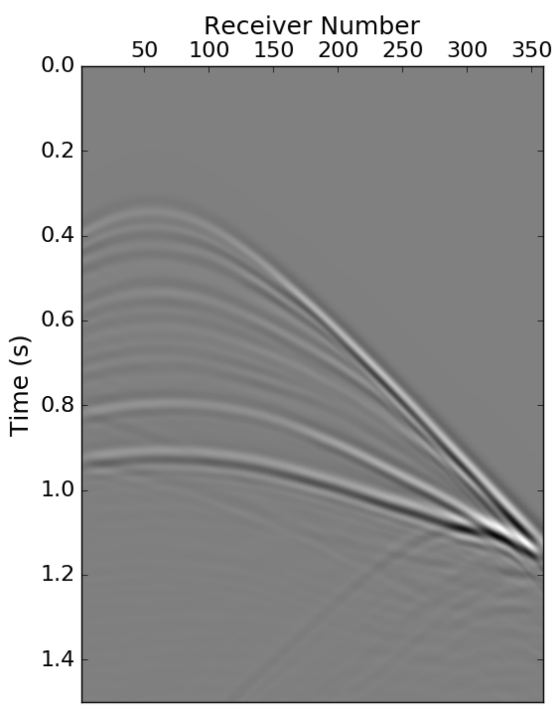

(a)

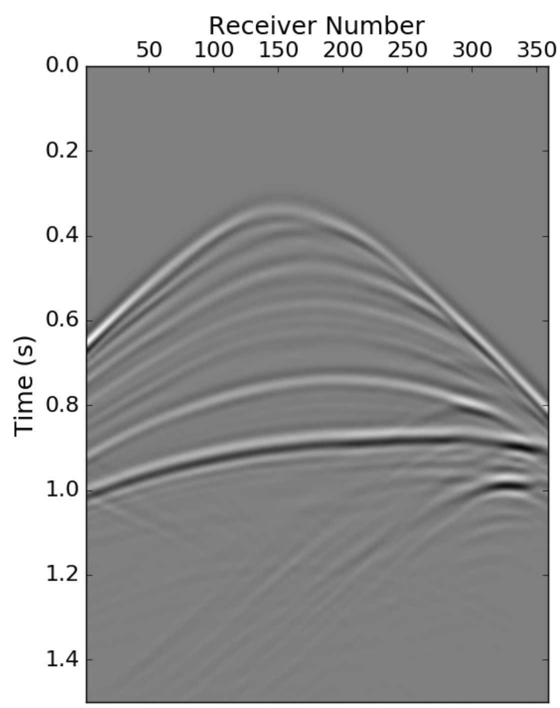

(b)

Figure 5.4: Observed data, without direct arrivals, at (a) $x = 275\,m$ and (b) $x = 775\,m$.

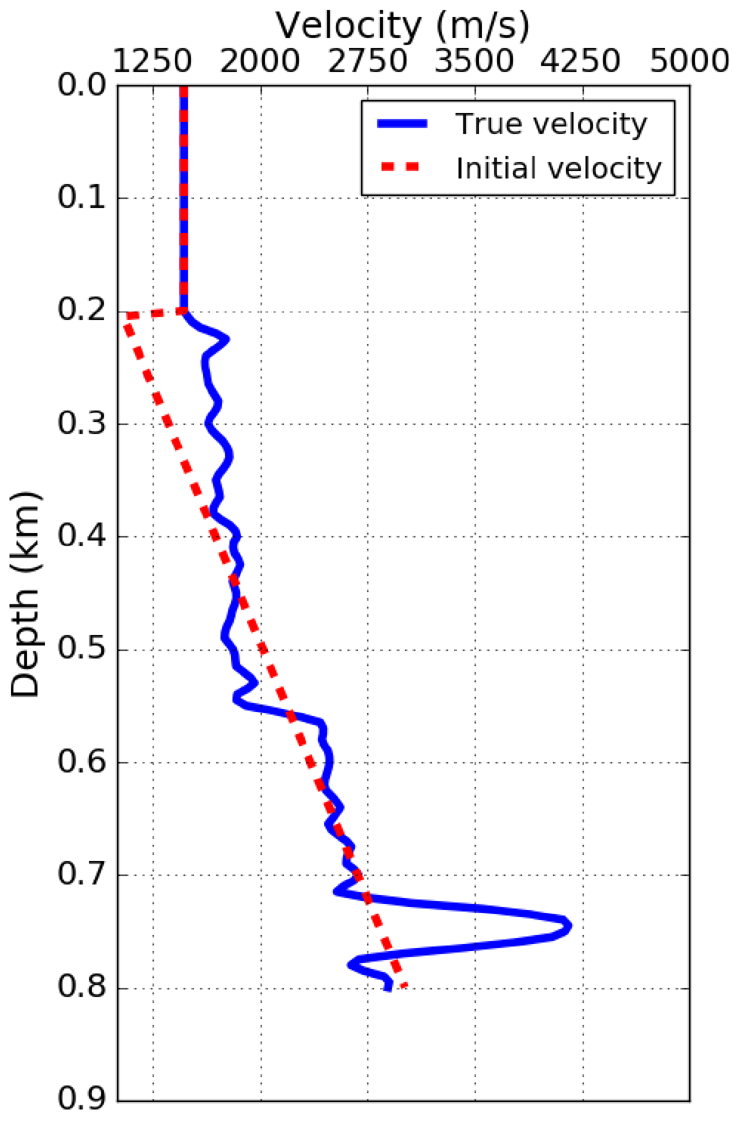

Figure 5.5: Vertical velocity profile at $x = 900\,m$ for the true and initial velocity models.

Acquisition geometry and model parameters			
nx	361	nz	161
dx	5.0 m	dt	0.68 ms
t_{max}	1.5 s	nt	2200
x_{max}	1800 m	z_{max}	800 m
Source x_0	25 m	Source x_{end}	1775 m
Receiver x_0	5 m	Receiver x_{end}	1800 m
Shot spacing	50 m	Receiver spacing	5 m
Number of shots	36	Number of receivers	359
Depth of shots	5 m	Depth of receiver	5 m

Table 5.1: Acquisition geometry and model parameters.

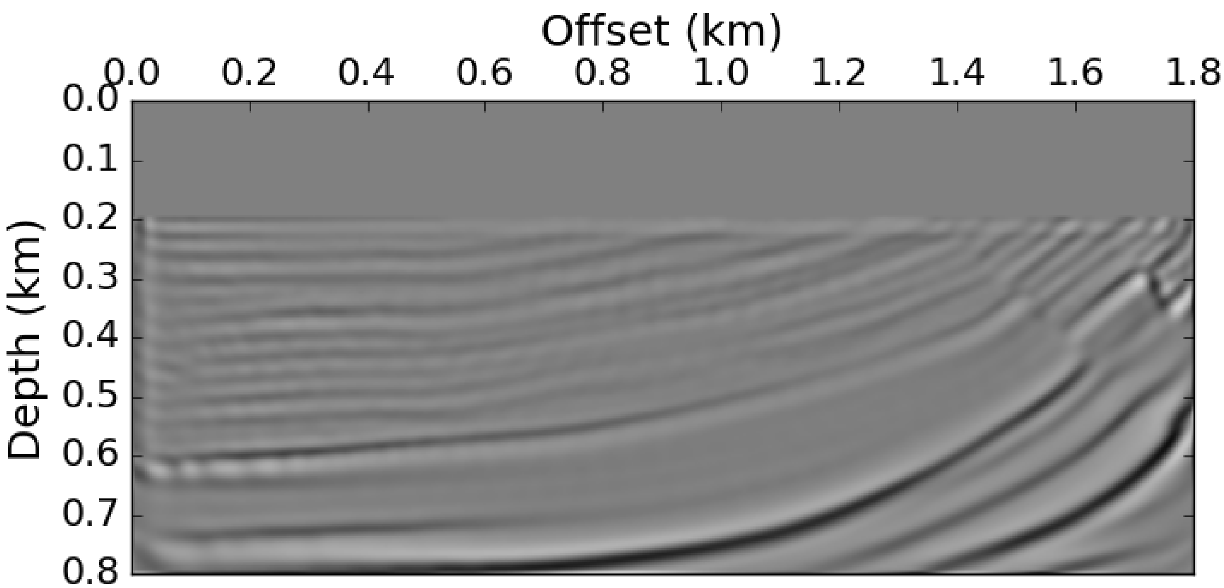

Figure 5.6: RTM image migrated using the true velocity model.

5.3 Inversion

5.3.1 RWI equations

In this section, I present the set of equations used to generate the source wavefield and the data residuals receiver wavefield used in the gradient calculation, equations (3.35) and (3.36), and the source and receiver wavefields needed to migrated the observed data, equation (3.30). The equation used to generate the source wavefield, used in the gradient calculation, is given by

$$\left[\bigtriangledown^2 - \mathbf{m}\frac{\partial^2}{\partial t^2}\right] G(\mathbf{r}, t; \mathbf{r}_s) = f(t), \tag{5.1}$$

and the equation used to compute the data residuals receiver wavefield, used in the gradient calculation, is

$$\begin{cases} \left[\bigtriangledown^2 - \mathbf{m}\frac{\partial^2}{\partial t^2}\right] G(\mathbf{r}, t; \mathbf{r}_g) = 0 \\ G(\mathbf{r}_s, t; \mathbf{r}_g) = \delta P(\mathbf{r}_g, t; \mathbf{r}_s). \end{cases} \tag{5.2}$$

The source wavefield equation used to produce the RTM image is

$$\left[\bigtriangledown^2 - \mathbf{m}\frac{\partial^2}{\partial t^2}\right] G(\mathbf{r}, t; \mathbf{r}_s) = f(t), \tag{5.3}$$

and the equation used to calculate receiver wavefield needed for the RTM is

$$\begin{cases} \left[\bigtriangledown^2 - \mathbf{m}\frac{\partial^2}{\partial t^2}\right] G(\mathbf{r}, t; \mathbf{r}_g) = 0 \\ G(\mathbf{r}_s, t; \mathbf{r}_g) = G(\mathbf{r}_g, t; \mathbf{r}_s). \end{cases} \tag{5.4}$$

The equations used to calculate the demigrated source and demigrated receiver wavefields remain unchanged, equations (3.31) and (3.34).

5.3.2 RWI results

The results presented in this chapter are for gradients with source-receiver illumination compensation being applied. In Figure (5.7) the RTM migrated image using the initial velocity is plotted. The two red curves on the migrated section are the correct positions of two major reflectors in the velocity model. The initial velocity model, in general, has lower velocity than the true velocity model (Figure 5.5). Therefore, reflectors are shifted up. The first and second major reflectors are $65\,m$ and $85\,m$ away from their true positions, respectively. The correlation coefficient between the migrated image using the initial velocity (Figure 5.7) and the migrated image using the true velocity (Figure 5.6) is 0.026. For details about correlation coefficient, the reader is referred to Asuero et al. (2006).

In Figures (5.8) and (5.9) the inverted velocity and the velocity perturbation are plotted. It is difficult to evaluate the accuracy of the inverted model; hence, the velocity perturbation (Figure 5.9) provides a more tangible measure. The inverted velocity captured the general characteristics of the structures of the true model; however, the perturbation is relatively small, and mainly occurring below the water bottom-layer immediately. In Figure (5.10) a vertical velocity profile across the center of the model, at $x = 3750\,m$, is plotted for both the true and the inverted velocity models.

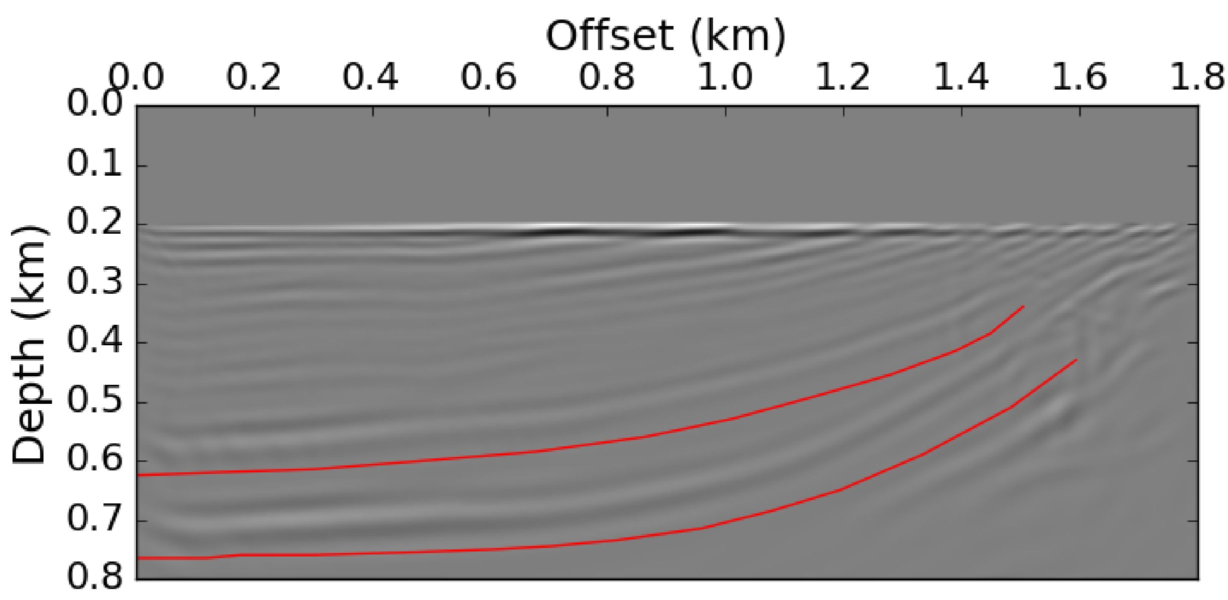

Figure 5.7: RTM image migrated using the initial velocity. The red curves are the correct positions of a two major reflectors in the velocity model.

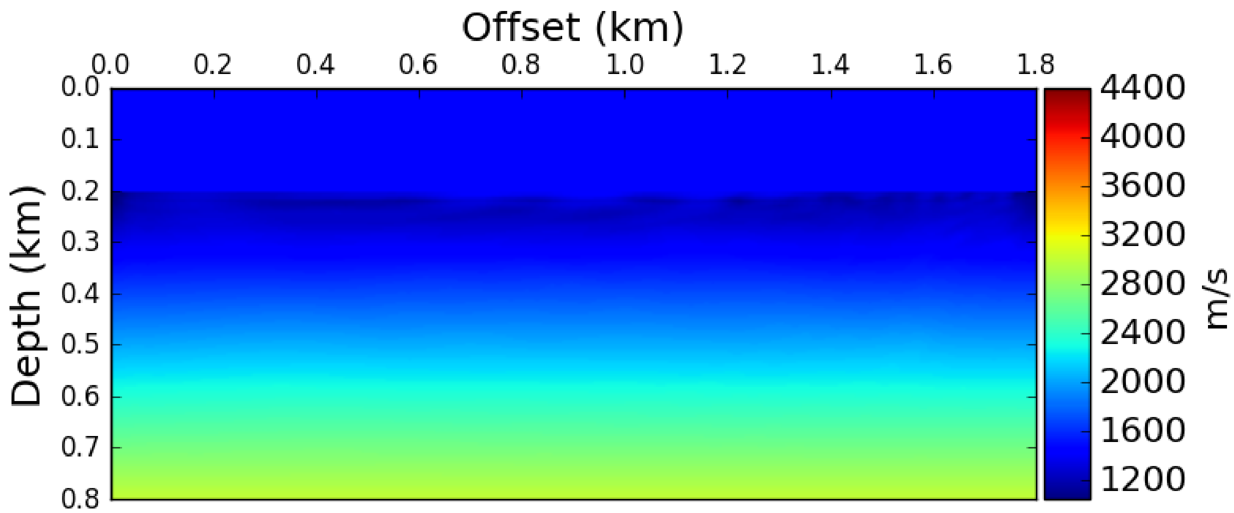

Figure 5.8: Inverted velocity model using RWI.

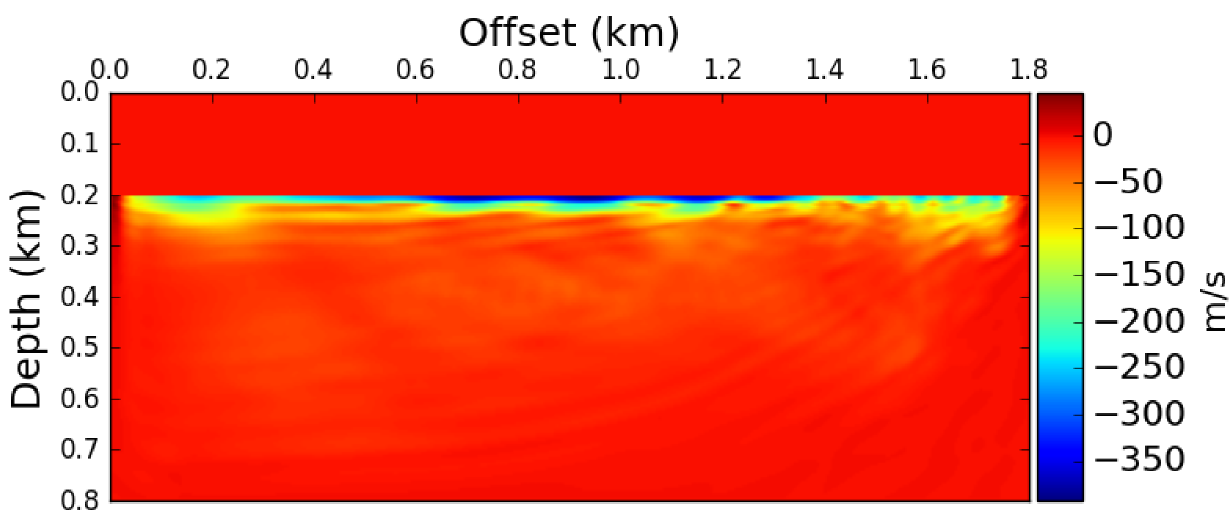

Figure 5.9: Velocity perturbation.

In Figure (5.11) the RTM migrated image generated using the inverted velocity, with the true positions of the two major reflectors marked in red, is plotted. The reflectors are closer to their actual subsurface positions, compared to the RTM image generated using the initial velocity. The first major reflector is $47\,m$ away from its true position and the second

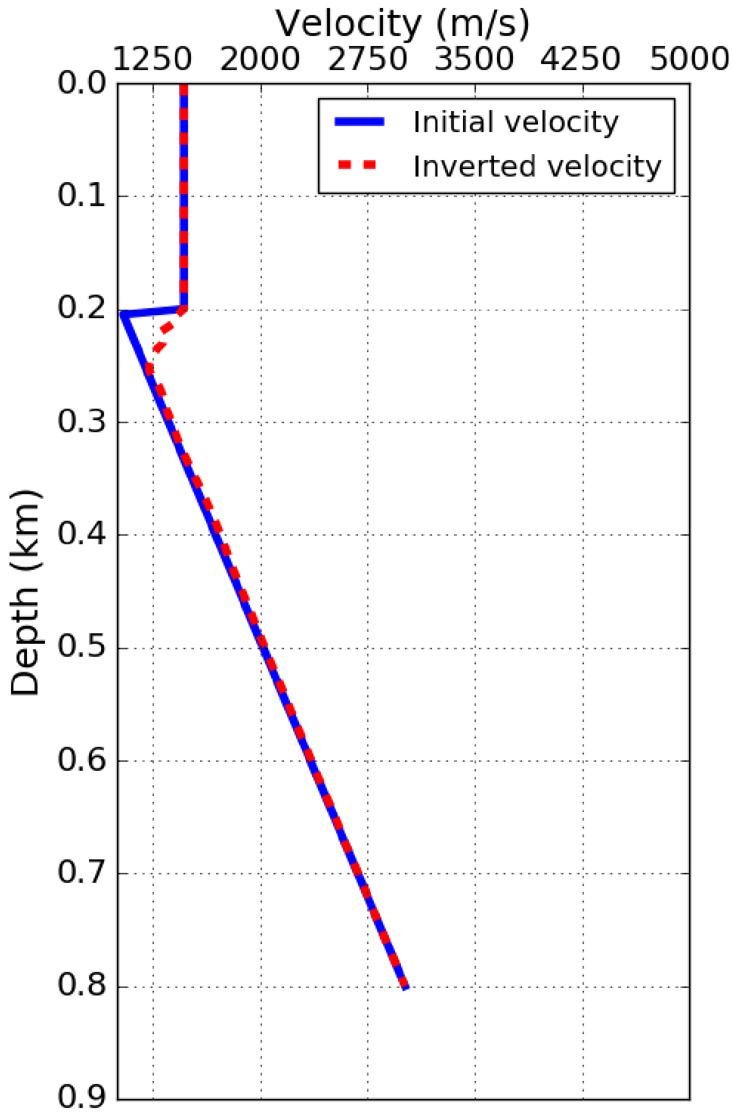

Figure 5.10: Vertical velocity profile at $x = 900\,m$ for the initial and inverted velocity models.

major reflector is $60\,m$ away from its true position. Also, shallow horizons are more coherent and more visible, compared the RTM image migrated using the initial velocity model. The correlation coefficient between the migrated image using the inverted velocity (Figure 5.11) and the migrated image using the true velocity (Figure 5.6) is 0.049. There is an increase in the correlation coefficient between the RTM image produced using the inverted velocity and the RTM image produced using the true velocity, compared to when using the initial velocity to migrate the observed data.

The convergence rate of the inversion process is plotted in Figure (5.12). The red line in the plot is the ratio of the norm of the data residuals squared, when using the true velocity (Figure 5.2) as an initial model, to the norm of the data residuals squared when using our original initial model (Figure 5.3). (The true model is only used to generate predicted data, and not as a starting model for the inversion; hence, the constant error line.) When using the true velocity, the error is not zero, as normally expected in FWI, when using the same model and same operator to generate the observed and predicted data; however, a high error value is obtained. This error is attributed to the fact that predicted data lacks the angle-dependent information present in the observed data. The change from the initial model is relatively small, and this can be observed in the model domain (Figure 5.8); however, there is a significant improvement in the image domain (Figure 5.11).

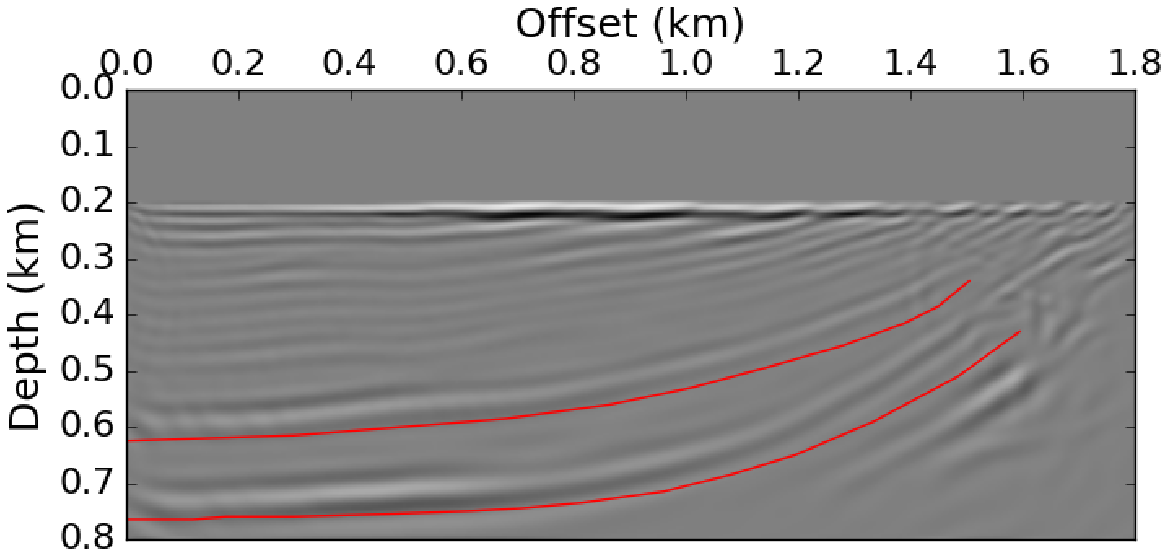

Figure 5.11: RTM image migrated using the inverted velocity. The red curves are the correct positions of a two major reflectors in the velocity model.

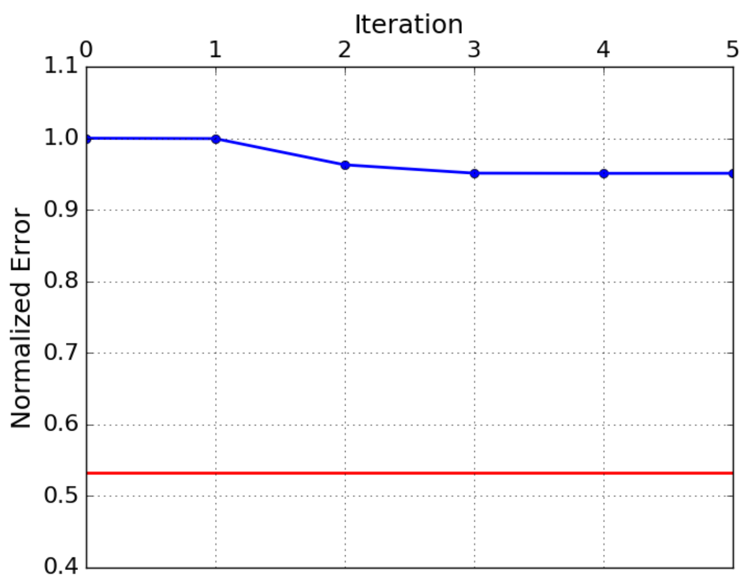

Figure 5.12: Normalized objective function per iteration.

5.3.3 FWI results

In this section, I present the FWI results to benchmark the RWI recovery of the low frequency information from reflection data. In Figure (5.13) the inverted velocity using FWI is plotted. I can see that the inverted velocity is more detailed compared to the results from the RWI. In the RTM migrated image constructed using the FWI inverted velocity, the two major reflectors are closer to their correct position; however, they are less coherent than the results of RWI (Figure 5.11). The average separation between the first major reflector and its true position is $21\,m$ and the average separation between the second major reflector and its true position is $26\,m$. Also, FWI introduces false structures. The correlation coefficient between the migrated image using the FWI inverted velocity (Figure 5.13) and the migrated image using the true velocity (Figure 5.6) is -0.119.

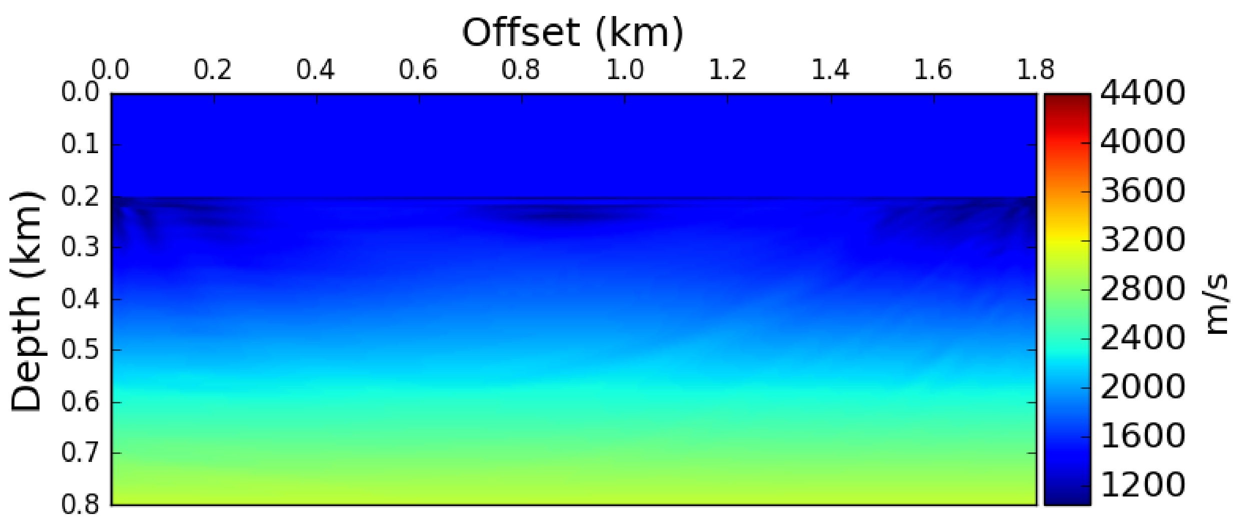

Figure 5.13: Inverted velocity model using FWI.

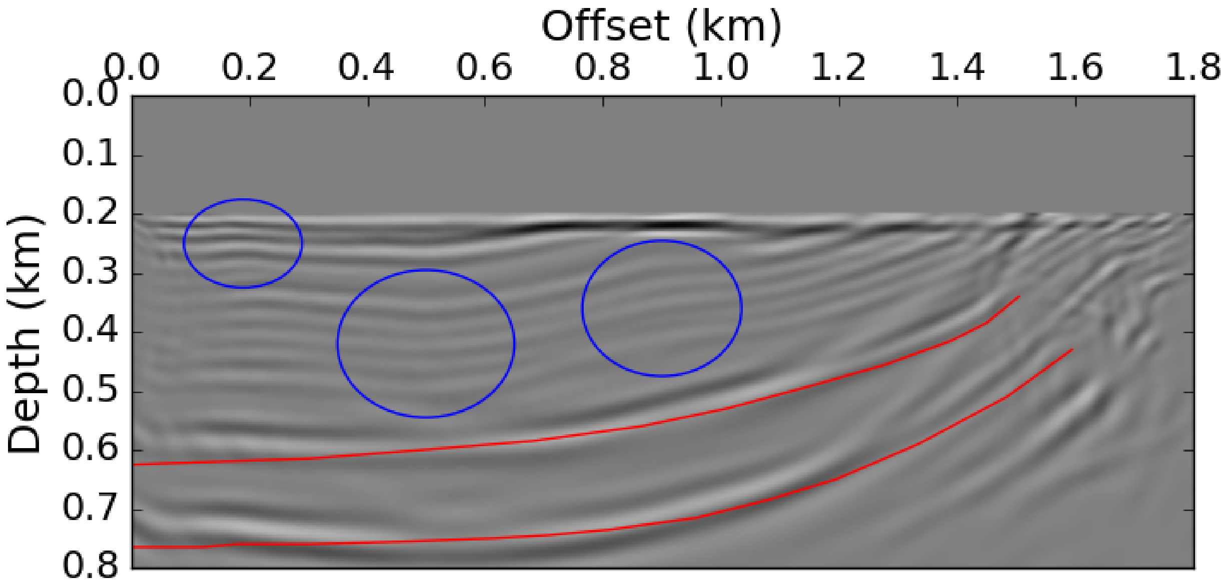

Figure 5.14: RTM image migrated using the FWI inverted velocity. The red curves are the correct positions of a two major reflectors in the velocity model. The blue ellipses are the false structures.

5.4 Conclusion

In this chapter, I applied RWI to a model with complex media. The RWI inverted velocity improves the migration results, compared to that when using the initial velocity, as reflectors are closer to their actual subsurface positions and horizons are well-defined and more coherent. I have shown that FWI gives favorable results, at positioning reflections at their correct position; however, events are blurred and false structures are created. Also, I have shown that when using the true velocity model to generate predicted data, we get a relatively high error value, due to modeling by seismic demigration.

Chapter 6

Practical obstacles to development of RWI

6.1 Introduction

In this chapter, I discuss two major issues associated with RWI. All of the issues presented here arise as a result of the demigration process. In our discussion, I start with the consequences of modeling by seismic demigration on the amplitude versus offset (AVO) information of the predicted data, and its implication on the objective function. Next, I discuss the necessity of using reflection-only observed data.

6.2 Seismic demigration and AVO information

AVO refers to the dependency of seismic amplitude on the source-receiver separation distance; accordingly, it is dependent on the angle of incidence. It is a tool used to analyze subsurface properties such as velocity, density, lithology, and fluid content. AVO information plays a major role in multiparameter waveform inversion, as some physical parameters, such as density and velocity, are indistinguishable at small angles of incidence. Consequently, measurement differences at large angles of incidence are necessary to retrieve these parameters (Innanen, 2015).

In RWI, predicted data is generated through the process of seismic demigration (equation 2.26). Since the demigration process is not an exact inversion method, there is a loss of information when applied, especially AVO information. In Figure (6.1) the AVO signature of observed and predicted data generated using a two layer velocity model, where the velocity of the first layer is $1911\,m/s$ and the velocity of the second layer is $3248.7\,m/s$, is plotted. The amplitudes in the predicted data are almost invariant with offset in comparison with the data generated with complete wave physics included. As a consequence, using a least-squares objective function (equation 3.4) will result in a highly nonlinear problem. Also, when using the true velocity as an initial model, unlike with conventional FWI, the objective function is not zero, as seen in Section (5.3.2).

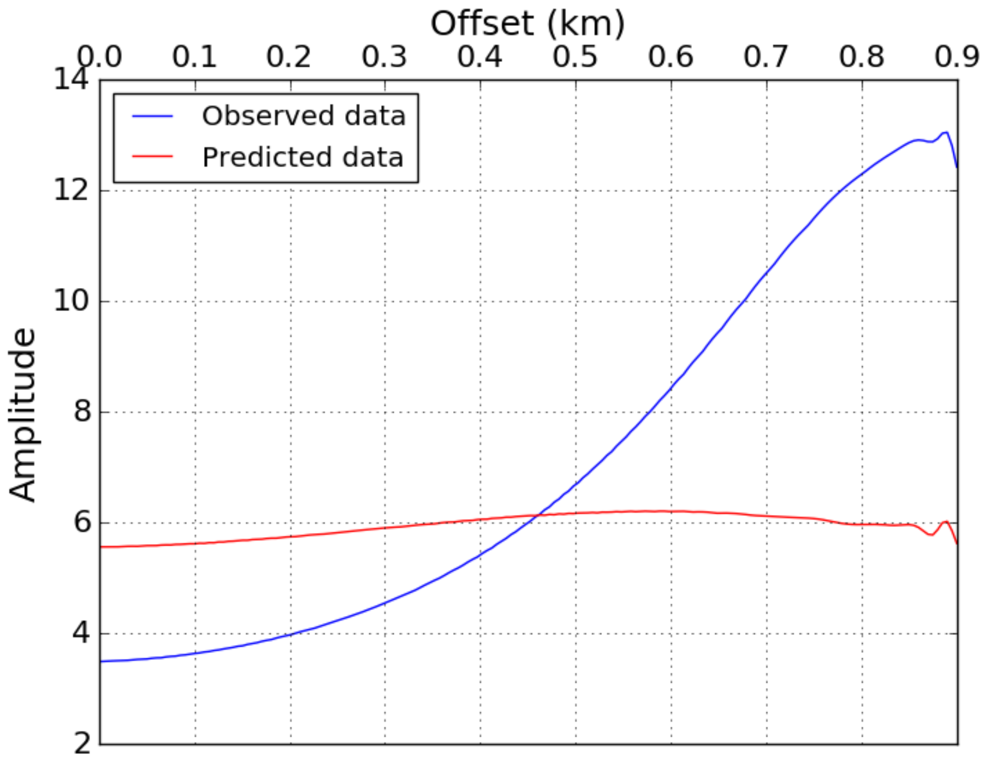

Figure 6.1: AVO of the observed and predicted data.

To overcome this limitation, I employ cross-correlation objective function (equation 6.1) instead of the least-squares function (equation 3.4).

$$E(\mathbf{m}_0) = -\sum_{\mathbf{r}_s,\mathbf{r}_g} \int d\omega\, G(\mathbf{r}_g, \omega; \mathbf{r}_s) G_0^*(\mathbf{r}_g, \omega; \mathbf{r}_s). \tag{6.1}$$

Using a cross-correlation objective function emphasizes the similarities between the observed and predicted data, rather than the differences, and relaxes on the amplitude constraints (Liu et al., 2017); hence, it offers a better alternative to the conventional objective function when AVO information is not available. In Figure (6.1) the inverted velocity using the new objective function is plotted. Comparing this result to the previous one (Figure 4.20), the Gaussian anomaly is more accurately inverted. The significant velocity increase around the lens is less severe in this result. Although the interfaces between the layers are more visible and well-defined, the inverted velocity contains less information about the second layer. In Figure (6.3) the migrated image using the inverted velocity is plotted. The improvements when using the cross-correlation objective function are apparent. In the previous result (Figure 4.22), horizons were well-focused and coherent; however, major false structures were created by the inaccuracy of the inverted velocity. On the other hand, this method offers a better result, where horizons are even more coherent, in particular on the sides of the migrated image, and there are no false structures.

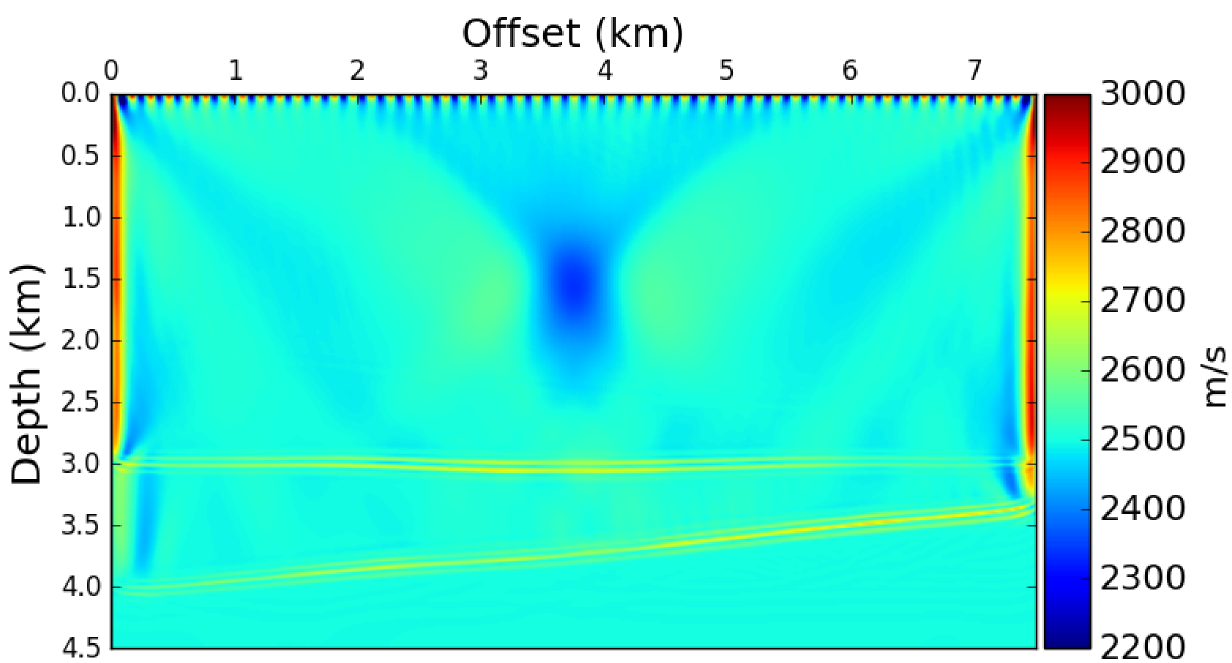

Figure 6.2: Inverted model using cross-correlation objective function [Simple model (Chapter 4)].

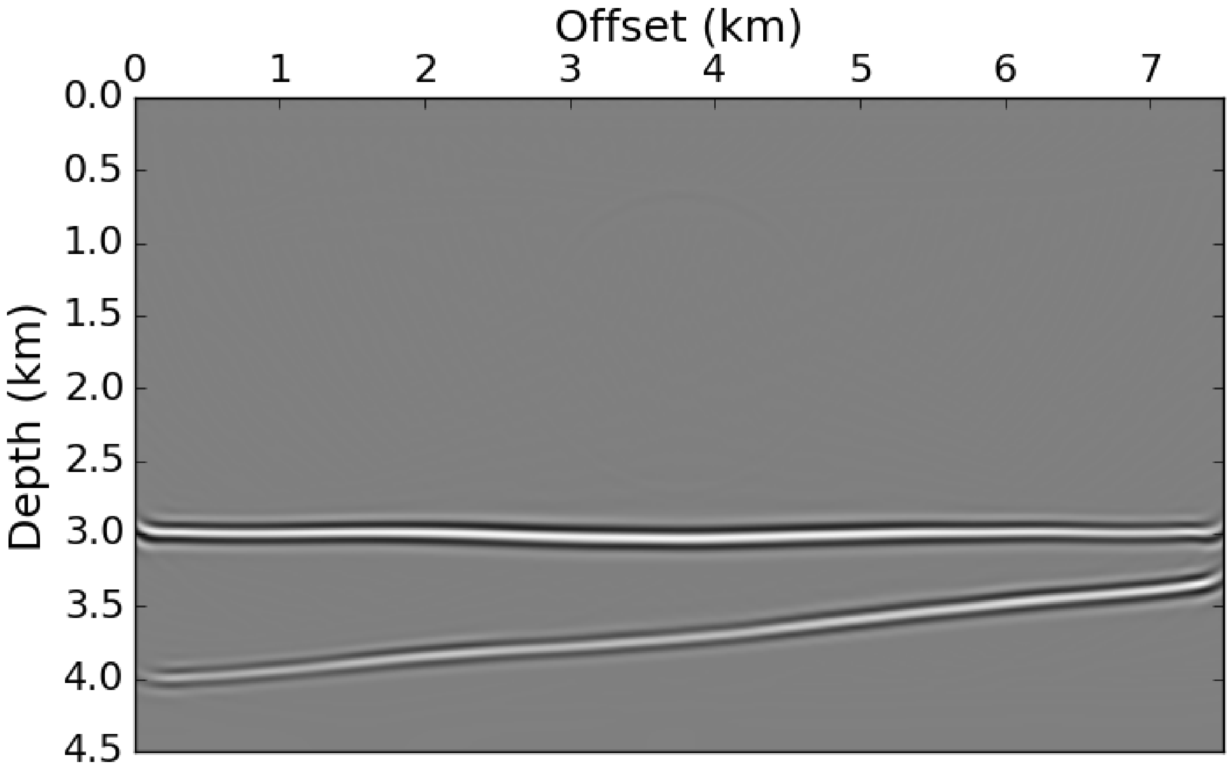

Figure 6.3: RTM migrated image using the cross-correlation objective function inverted velocity [Simple model (Chapter 4)].

6.3 Seismic demigration and reflected waves

In acoustic media, the incident wavefield produces different types of waves (e.g., reflections, refractions, and diving waves) depending on the angle of incidence and the subsurface physical properties. These waves have variable contributions to velocity model building in waveform inversion. For instance, deep reflections contribute towards updating the reflectivity part of the velocity model in FWI, while direct waves contribute towards inverting the long-wavelength part of the velocity model. In RWI, as stated in Chapter (3), reflected waves are utilized to invert for the background part of the velocity model by decomposing the velocity model into a reflectivity part and a background part. This decomposition mandates the use of modeling by seismic demigration to generate predicted data and to compute the gradient for the inversion. The demigration process, as described in Section (2.8), cannot produce any types of waves other than reflections. The reason for this is similar to that for why modeling by seismic demigration does not produce data with AVO information. According to the Zoeppritz equations and Snell's law, the most influential parameter controlling wave propagation behavior in the subsurface is velocity (diving waves are generated as a consequence of a velocity gradient). And the concept of the exploding reflector model, as the name suggests, only produces reflected waves. Therefore, the waves that contribute to the determination of long-wavelength components of the velocity model are neglected in the inversion process. These waves must be filtered from the observed data, and the filtering process is most likely imperfect.

6.4 Conclusion

In this chapter, I presented some of the issues with RWI, caused by the concept of modeling by seismic demigration. I have shown that the conventional objective function is not well suited for inversions with inaccurate amplitudes; further, I demonstrated that a cross-correlation objective function is insensitive to the amplitude variations, due to the lack of AVO information, and is more appropriate for RWI. Also, I have shown that RWI uses reflection-only data, as modeling by seismic demigration only produces reflected waves. This issue constrains us to exclude waves that would contribute in updating the long-wavelength components of the velocity model.

Chapter 7

Conclusions and future work

7.1 Conclusions

Full waveform inversion (FWI) is an emerging seismic imaging and inversion technique. It is being used, not just to provide a high-resolution structural image of the subsurface, but also to provide the subsurface material properties. It suffers from a range of limitations as it is an ill-posed nonlinear problem. To obtain accurate results, initial models in FWI need to predict data within a half-cycle from the observed data. Otherwise, cycle-skipping will occur, and the inversion will converge to local minima. The low-frequency and long-offset data needed to mitigate this issue are frequently unavailable due to seismic acquisition limitations. In RWI cycle-skipping can still occur at far offsets (Chi et al., 2015). In this thesis, I presented and tested a new inversion method based on model decomposition, namely reflection-based waveform inversion (RWI). The objective of this approach is to recover the background part of the velocity model, which is the part of model controlling arrival times of seismic data; hence, providing a better starting model for FWI.

In Chapter 2, I have reviewed the aspects of wave equation modeling, including the absorbing boundary conditions, the finite-difference scheme, and the stability and accuracy of the numerical modeling. Also, I reviewed essential concepts in RWI which are the concept of reverse-time migration, and the concept of modeling by seismic demigration.

In Chapter 3, I presented the theory behind and the formulation of RWI. I explained the motivation behind using RWI over FWI and indicated that a reflection-dominated data have limited ability to recover the background velocity. Also, I have shown the methodology at which RWI construct the gradient and how it is different from FWI gradient.

In Chapter 4, I inverted for a simple model using both FWI and RWI. I have shown that RWI has been able to recover the background velocity from reflection-only data, while FWI failed even while using the full wavefield. Migrating data using RWI inverted velocity provides a preferable image compared to that when using FWI results. I have shown that higher order iterations in RWI tend to produce incorrect results. Also, I examined the consequences of preconditioning the gradient with the source and receiver wavefields, which is equivalent to applying the diagonal of the Hessian (Plessix and Mulder, 2004; Shin et al., 2001), on the inversion results. I demonstrated how applying source-receiver illumination further improve the inversion results, especially in deeper section.

In Chapter 5, I applied RWI to a small section of the Marmousi model, to evaluate the performance of RWI in complex media. I have shown that the RWI inverted velocity improved the migration results, compared to that when using the initial velocity. Also, I have shown that FWI gives comparable results; however, RWI still provided a better image, especially in areas with limited data. I have shown that when using the true velocity model to generate predicted data, modeling by seismic demigration fails at reconstructing the observed data.

In Chapter 6, I discussed some of the practical issues in RWI and its relationship to modeling by seismic demigration. I have shown that, as a consequence of modeling by seismic demigration, predicted data lacks any AVO information, and that this causes incorrect inversion results when using the least-squares objective function. I have demonstrated that a cross-correlation objective function is more suitable for RWI. Also, I have shown that RWI does not utilize all waves that contribute in updating the long-wavelength components of the velocity model.

7.2 Future work

While I demonstrated the potential of RWI method, many opportunities exist to explore its full potential and limits. One can study the applicability of incorporating refractions, direct, or diving waves to improve the inversion results. Also, one can examine the results when using the unstacked migrated shots to perform the demigration and compare to the results when using the stacked image for the demigration. Using the migrated shots, instead of the stacked image, does not require any additional computations. Also, using different migration algorithms is important in understanding the sensitivity of RWI towards the variations in these methods. Moreover, evaluating the performance of an acoustic and and elastic RWI with elastic data is important. Also, a multiparameter RWI attempt could motivate an AVO incorporated demigration process. Additionally, examining different objective functions, and observed and predicted data normalization methods is necessary. Moreover, examining the effect of the initial model on the convergence of RWI is important. Also, understanding the effects of signal-to-noise ratio on the quality of the inversion is necessary. Finally, RWI is a computationally expensive problem and finding different approaches, to decrease the needed number of forward-modeling problems, is vital.

Bibliography

Alford, R., Kelly, K., and Boore, D. M., 1974, Accuracy of finite-difference modeling of the acoustic wave equation: Geophysics, **39**, No. 6, 834–842.

Asuero, A., Sayago, A., and Gonzalez, A., 2006, The correlation coefficient: An overview: Critical reviews in analytical chemistry, **36**, No. 1, 41–59.

Baysal, E., Kosloff, D. D., and Sherwood, J. W., 1983, Reverse time migration: Geophysics, **48**, No. 11, 1514–1524.

Berkhout, A., 1981, Wave field extrapolation techniques in seismic migration, a tutorial: Geophysics, **46**, No. 12, 1638–1656.

Bleistein, N., Cohen, J., and Stockwell, J. W. J., 2001, Mathematics of multidimensional seismic imaging, migration, and inversion: Springer.

Brossier, R., Operto, S., and Virieux, J., 2015, Velocity model building from seismic reflection data by full-waveform inversion: Geophysical Prospecting, **63**, No. 2, 354–367.

Bunks, C., Saleck, F. M., Zaleski, S., and Chavent, G., 1995, Multiscale seismic waveform inversion: Geophysics, **60**, No. 5, 1457–1473.

Chi, B., Dong, L., and Liu, Y., 2015, Correlation-based reflection full-waveform inversion: Geophysics, **80**, No. 4, R189–R202.

Claerbout, J. F., 1970, Coarse grid calculations of waves in inhomogeneous media with application to delineation of complicated seismic structure: Geophysics, **35**, No. 3, 407–418.

Claerbout, J. F., 1971, Toward a unified theory of reflector mapping: Geophysics, **36**, No. 3, 467–481.

Claerbout, J. F., 1985, Imaging the earth's interior: Blackwell scientific publications Oxford.

Clayton, R., and Engquist, B., 1977, Absorbing boundary conditions for acoustic and elastic wave equations: Bulletin of the Seismological Society of America, **67**, No. 6, 1529–1540.

Crase, E., Pica, A., Noble, M., McDonald, J., and Tarantola, A., 1990, Robust elastic nonlinear waveform inversion: Application to real data: Geophysics, **55**, No. 5, 527–538.

Devaney, A. J., 1982, A filtered backpropagation algorithm for diffraction tomography: Ultrasonic imaging, **4**, No. 4, 336–350.

Engquist, B., and Majda, A., 1977, Absorbing boundary conditions for numerical simulation of waves: Proceedings of the National Academy of Sciences, **74**, No. 5, 1765–1766.

Gray, S. H., and May, W. P., 1994, Kirchhoff migration using eikonal equation traveltimes: Geophysics, **59**, No. 5, 810–817.

Guitton, A., Kaelin, B., and Biondi, B., 2006, Least-square attenuation of reverse time migration artifacts, *in* SEG Technical Program Expanded Abstracts 2006.

Hagedoorn, J. G., 1954, A process of seismic reflection interpretation: Geophysical Prospecting, **2**, No. 2, 85–127.

Hemon, C., 1978, Equations d'onde et modeles: Geophysical Prospecting, **26**, No. 4, 790–821.

Innanen, K. A., 2015, Full waveform inversion updating in the presence of high angle/high contrast reflectivity, *in* SEG Technical Program Expanded Abstracts 2015, Society of Exploration Geophysicists.

Jannane, M., Beydoun, W., Crase, E., Cao, D., Koren, Z., Landa, E., Mendes, M., Pica, A., Noble, M., Roeth, G. et al., 1989, Wavelengths of earth structures that can be resolved from seismic reflection data: Geophysics, **54**, No. 7, 906–910.

Lailly, P., 1983, The seismic inverse problem as a sequence of before stack migrations, *in* Conference on Inverse Scattering: Theory and Application, Society of Industrial and Applied Mathematics, 206–220.

Lines, L. R., Slawinski, R., and Bording, R. P., 1999, A recipe for stability of finite-difference wave-equation computations: Geophysics, **64**, No. 3, 967–969.

Liu, Y., Teng, J., Xu, T., Wang, Y., Liu, Q., and Badal, J., 2017, Robust time-domain full waveform inversion with normalized zero-lag cross-correlation objective function: Geophysical Journal International, **209**, No. 1, 106–122.

Marfurt, K. J., 1984, Accuracy of finite-difference and finite-element modeling of the scalar and elastic wave equations: Geophysics, **49**, No. 5, 533–549.

Margrave, G. F., Ferguson, R. J., and Hogan, C. M., 2010, Full waveform inversion with wave equation migration and well control: CREWES Annual Report, **22**, 1–20.

McMechan, G. A., 1983, Migration by extrapolation of time-dependent boundary values: Geophysical Prospecting, **31**, No. 3, 413–420.

Miller, D., Oristaglio, M., and Beylkin, G., 1987, A new slant on seismic imaging: Migration and integral geometry: Geophysics, **52**, No. 7, 943–964.

Mora, P., 1987, Nonlinear two-dimensional elastic inversion of multioffset seismic data: Geophysics, **52**, No. 9, 1211–1228.

Mulder, W., and Plessix, R.-E., 2008, Exploring some issues in acoustic full waveform inversion: Geophysical Prospecting, **56**, No. 6, 827–841.

Operto, S., Gholami, Y., Prieux, V., Ribodetti, A., Brossier, R., Metivier, L., and Virieux, J., 2013, A guided tour of multiparameter full-waveform inversion with multicomponent data: From theory to practice: The Leading Edge, **32**, No. 9, 1040–1054.

Pan, W., and Innanen, K., 2015a, Full-waveform inversion in the frequency-ray parameter domain: CREWES Annual Report, **27**.

Pan, W., and Innanen, K., 2015b, Suppressing cross-talk for elastic fwi with multi-parameter approximate hessian and its parameter-type approximation: CREWES Annual Report, **27**.

Pan, W., Innanen, K. A., Margrave, G. F., Fehler, M. C., Fang, X., and Li, J., 2016, Estimation of elastic constants for hti media using gauss-newton and full-newton multiparameter full-waveform inversion: Geophysics, **81**, No. 5, R275–R291.

Plessix, R.-E., and Mulder, W., 2004, Frequency-domain finite-difference amplitude-preserving migration: Geophysical Journal International, **157**, No. 3, 975–987.

Pratt, R. G., 1999, Seismic waveform inversion in the frequency domain, part 1: Theory and verification in a physical scale model: Geophysics, **64**, No. 3, 888–901.

Pratt, R. G., and Shipp, R. M., 1999, Seismic waveform inversion in the frequency domain, part 2: Fault delineation in sediments using crosshole data: Geophysics, **64**, No. 3, 901–914.

Pratt, R. G., and Worthington, M., 1990, Inverse theory applied to multi-source cross-hole tomography. part 1: Acoustic wave-equation method: Geophysical Prospecting, **38**, No. 3, 287–310.

Prieux, V., Brossier, R., Operto, S., and Virieux, J., 2013, Multiparameter full waveform inversion of multicomponent ocean-bottom-cable data from the valhall field. part 1: Imaging compressional wave speed, density and attenuation: Geophysical Journal International, **194**, No. 3, 1640–1664.

Schneider, W. A., 1978, Integral formulation for migration in two and three dimensions: Geophysics, **43**, No. 1, 49–76.

Shin, C., Jang, S., and Min, D.-J., 2001, Improved amplitude preservation for prestack depth migration by inverse scattering theory: Geophysical Prospecting, **49**, No. 5, 592–606.

Sirgue, L., and Pratt, R. G., 2004, Efficient waveform inversion and imaging: A strategy for selecting temporal frequencies: Geophysics, **69**, No. 1, 231–248.

Snieder, R., 1998, The role of nonlinearity in inverse problems: Inverse Problems, **14**, No. 387-404.

Stolt, R., and Weglein, A., 1985, Migration and inversion of seismic data: Geophysics, **50**, No. 12, 2458–2472.

Tarantola, A., 1984, Inversion of seismic reflection data in the acoustic approximation: Geophysics, **49**, No. 8, 1259–1266.

Versteeg, R., 1994, The marmousi experience: Velocity model determination on a synthetic complex data set: The Leading Edge, **13**, No. 9, 927–936.

Virieux, J., 1986, P-SV wave propagation in heterogeneous media: Velocity-stress finite-difference method: Geophysics, **51**, No. 4, 889–901.

Virieux, J., and Operto, S., 2009, An overview of full-waveform inversion in exploration geophysics: Geophysics, **74**, No. 6, WCC127–WCC152.

Wang, S., Chen, F., Zhang, H., and Shen, Y., 2013, Reflection-based full waveform inversion (rfwi) in the frequency domain, *in* SEG Technical Program Expanded Abstracts 2013.

Wang, Y., 2016, Seismic inversion: theory and applications: John Wiley & Sons.

Whitmore, N. D., 1983, Iterative depth migration by backward time propagation, *in* SEG Technical Program Expanded Abstracts 1983.

Wu, R.-S., and Toksöz, M. N., 1987, Diffraction tomography and multisource holography applied to seismic imaging: Geophysics, **52**, No. 1, 11–25.

Xu, S., Wang, D., Chen, F., Zhang, Y., and Lambare, G., 2012, Full waveform inversion for reflected seismic data, *in* 74th EAGE Conference and Exhibition incorporating EUROPEC 2012.

Yilmaz, Ö., 2001, Seismic data analysis: Processing, inversion, and interpretation of seismic data: Society of Exploration Geophysicists.

Zhang, Y., and Sun, J., 2009, Practical issues of reverse time migration: True amplitude gathers, noise removal and harmonic source encoding: First break, **27**, No. 1, 53–59.

Zhou, H., Amundsen, L., and Zhang, G., 2012, Fundamental issues in full waveform inversion, *in* SEG Technical Program Expanded Abstracts 2012.